Infinite and Finite Blocklength Analysis of RIS assisted Communication with Spectrally Efficient Signaling Techniques

A Thesis Submitted

in Partial Fulfilment of the Requirements

for the Degree of

DOCTOR OF PHILOSOPHY

by

Shiv Kumar

(2019eez0025)



DEPARTMENT OF ELECTRICAL ENGINEERING INDIAN INSTITUTE OF TECHNOLOGY ROPAR

May, 2025

Shiv Kumar: Infinite and Finite Blocklength Analysis of RIS assisted Communication with Spectrally Efficient Signaling Techniques Copyright © 2025, Indian Institute of Technology Ropar

All Rights Reserved

Declaration of Originality

I hereby declare that the work which is being presented in the thesis entitled, "Infinite and Finite Blocklength Analysis of RIS assisted Communication with Spectrally Efficient Signaling Techniques" has been solely authored by me. It presents the result of my own independent investigation/research conducted during the time period from January, 2020 of joining the Ph.D. program to February, 2025 of Ph.D under the supervision of Dr. Brijesh Kumbhani, Assistant Professor in the Department of Electrical Engineering, IIT Ropar. To the best of my knowledge, it is an original work, both in terms of research content and narrative, and has not been submitted or accepted elsewhere, in part or in full, for the award of any degree, diploma, fellowship, associateship, or similar title of any university or institution. Further, due credit has been attributed to the relevant state-of-the-art and collaborations (if any) with appropriate citations and acknowledgments, in line with established ethical norms and practices. I also declare that any idea/data/fact/source stated in my thesis has not been fabricated/ falsified/ misrepresented. All the principles of academic honesty and integrity have been followed. I fully understand that if the thesis is found to be unoriginal, fabricated, or plagiarized, the Institute reserves the right to withdraw the thesis from its archive and revoke the associated Degree conferred. Additionally, the Institute also reserves the right to appraise all concerned sections of society of the matter for their information and necessary action (if any). If accepted, I hereby consent for my thesis to be available online in the Institute's Open Access repository, inter-library loan, and the title & abstract to be made available to outside organizations.

Signature

Name: Shiv Kumar

Entry Number: 2019eez0025

Program: PhD

Department: Electrical Engineering
Indian Institute of Technology Ropar

Rupnagar, Punjab 140001

Date: May, 2025

Acknowledgement

I want to express my sincere gratitude to my supervisor, Dr. Brijesh Kumbhani, for their unwavering support and guidance throughout this research journey. I am truly grateful for his valuable feedback and the patience he has demonstrated throughout the process. Additionally, I would like to acknowledge his assistance in meticulously reviewing and correcting all my manuscripts.

I want to thank my doctoral committee members, Dr. Sam Darshi, Dr. Suman Kumar, and Dr. Shahshi Sekhar Jha, for taking the time to evaluate the progress of my research. Their recommendations have been of great significance. Furthermore, I am grateful to the other faculty members and the head of the department, Dr. C.C. Reddy, for their continuous assistance during my studies. I want to thank all my collaborators, Dr. Rohit Singh, Dr. Satyam Agarwal, and Prof. Georges Kaddoum, for their helpful suggestions and comments on my research. I also acknowledge MHRD, Govt. of India, for financing my research studies at IIT Ropar.

Last but not least, I would like to express my deepest gratitude to my beloved parents, wife, and my little son Vinayak, who always support me at any time. Finally, I would like to thank the almighty for bestowing me this opportunity and showering his blessings on me to come out successful against all odds.

Certificate

This is to certify that the thesis entitled "Infinite and Finite Blocklength Analysis of RIS assisted Communication with Spectrally Efficient Signaling Techniques", submitted by Shiv Kumar (2019eez0025) for the award of the degree of Doctor of Philosophy of Indian Institute of Technology Ropar, is a record of bonafide research work carried out under my guidance and supervision. To the best of my knowledge and belief, the work presented in this thesis is original and has not been submitted, either in part or full, for the award of any other degree, diploma, fellowship, associateship or similar title of any university or institution.

In my opinion, the thesis has reached the standard of fulfilling the requirements of the regulations relating to the Degree.

Signature of the Supervisor

Dr. Brijesh Kumbhani

Department of Electrical Engineering Indian Institute of Technology Ropar

Rupnagar, Punjab 140001

Date: May, 2025

Lay Summary

The work of this thesis is centered around wireless/mobile communications which is currently expanding with exponential rate as most of the people are day to day user of wireless communication in one or the other way. It presents a work on analysis of wireless technologies for enhancement of user experience when connected to network via a phone call, accessing internet or attending a video conference. technology, the operation is affected by one or the other type of imperfection, error, or misbehaved component/device. Wireless/Mobile communication is not an exception to such imperfections and impairments. The analysis in this piece of work considers the effect of some of the imperfections in processing the received signals and while extracting the information from them. This thesis also considers the effect of some of the hardware imperfections on the system performance. The analysis has been performed on the wireless communication technologies that are possibly the part of future generations of the mobile communication, including 5th generation (5G) and beyond. While performing the analysis the focus is on energy efficient techniques and enhance the communication range without demanding huge energy. In addition to the energy efficiency, another expensive resource in wireless communications is the bandwidth. So, we also target the efficient use of bandwidth through simultaneous multiple signal transmission over same frequency channel. Thus, this thesis presents the analysis of amalgamation of energy efficient and bandwidth efficient wireless technology for future generation with practical use cases.

Abstract

Reconfigurable intelligent surfaces (RISs) emerged as a pivotal technology for the upcoming sixth generation (6G) wireless communication because of its characteristics of controlling propagation environment, increasing signal strength and extending coverage with sufficient energy efficiency (EE). On the other hand, to support the massive connectivity of devices with various quality-of-service (QoS) requirements and offer significant spectral efficiency (SE) and EE improvements, non-orthogonal multiple access (NOMA), cognitive radio (CR), and full-duplex (FD) systems have been considered as the potential technologies in the communication systems, such as cellular network, relaying networks, and wireless sensor networks. This thesis focuses on the performance analysis of RIS-assisted communications with spectrally efficient signaling techniques like NOMA, CR, and FD by using infinite blocklength (IBL) and finite blocklength (FBL) codes. Firstly, we design a novel paradigm of RIS-assisted NOMA system by formulating a phase shift matrix that provides coherent phase shift across both users of a NOMA pair. The performance of the considered system is analyzed by deriving the closed-form expression of outage probability (OP) and system throughput.

Furthermore, ultra-reliable and low-latency communication (URLLC) is one of the pillars for 6G networks to satisfy the rigorous conditions of internet of things (IoT) applications (e.g., industrial automation, remote surgery, virtual/augmented reality, tactile internet, and vehicle-to-everything communications) subjecting to extremely high reliability (99.999%) and ultralow latency ($\leq 1 \text{ ms}$). For such conditions, the conventional analysis approaches based on the Shannon capacity with the assumption of IBL wireless transmission are no longer suitable. To this end, a new transmission method, short-packet communication (SPC) with finite FBL codes, has been used to reduce the physical-layer transmission latency for URLLCs. Therefore, secondly, we have considered the IBL and FBL analysis of RIS-assisted CR-NOMA system with energy harvesting mechanism to deploy IoT devices by considering practical constraints of hardware impairments (HIs). For the IBL regime, we derived the analytical expression of OP and system throughput. For the FBL regime, we derived the novel analytical expression of average block error rate (ABLER), goodput, latency and reliability. Thirdly, we have investigated the performance of active RIS (ARIS) with two FD users communicating with each other using FBL codes by considering HIs at the FD transceiver nodes. We derived the analytical and asymptotic expressions of ABLER and ergodic capacity. Additionally system throughput, goodput and latency parameters are also analyzed. Finally, the FBL analysis of simultaneously transmitting and reflecting RIS (STAR-RIS) assisted NOMA system by considering imperfect channel state information (CSI) is analyzed. We derived the novel analytical expressions of ABLER, system throughput, goodput, latency and reliability. All the analytical results presented in this thesis are validated through extensive Monte-Carlo simulations.

Keywords: Cognitive radio; full-duplex; Non-orthogonal multiple access; reconfigurable intelligent surface (RIS); simultaneously transmitting and reflecting-RIS (STAR-RIS).

Contents

D	eclar	ation		iii
\mathbf{A}	cknov	wledge	ment	iv
\mathbf{C}	ertifi	cate		\mathbf{v}
La	ay Su	ımmary	7	vi
\mathbf{A}	bstra	ct		vii
Li	st of	Figure	es	xiii
Li	st of	Tables		$\mathbf{x}\mathbf{v}$
\mathbf{A}	crony	/ms		xvi
1	Introduction			
	1.1	Develo	pment of Wireless Communications	. 1
		1.1.1	Motivation for using Reconfigurable Intelligent Surfaces	. 3
		1.1.2	Motivation for using Simultaneous Transmitting and Reflecting	
			Reconfigurable Intelligent Surfaces	. 5
		1.1.3	Motivation for using Non Orthogonal Multiple Access	6
	1.2	Thesis	Contributions	. 7
	1.3	Thesis	Organization	. 8
2	Bac	kgroun	d and Literature Review	11
	2.1	Smart	Radio Environment	. 11
	2.2	RIS Fu	indamentals	. 11
		2.2.1	Patch-array-based RIS:	. 12
		2.2.2	Metasurface-based RIS:	. 12
		2.2.3	Statistical Channel Modeling of RIS assisted Communication $\ \ldots \ \ldots$. 13
	2.3	Active	RIS	. 14
	2.4	STAR-	RIS	. 15
		2.4.1	Signal Model of STAR-RIS	. 15

 ${f x}$

		2.4.2	Operating Protocols for STAR-RIS	16
			2.4.2.1 Energy splitting (ES):	17
			2.4.2.2 Mode switching (MS):	17
			2.4.2.3 Time switching (TS):	18
	2.5	PD-N	OMA	18
	2.6	Finite	Blocklength Transmission	19
	2.7	Literat	ture Review	20
		2.7.1	Literature on IBL analysis for RIS/STAR-RIS assisted communication	20
		2.7.2	Literature on FBL analysis RIS/STAR-RIS assisted communication	23
3	AN	lovel P	Paradigm for RIS-NOMA Transmission	26
	3.1	Systen	n Model	27
		3.1.1	Design of Phase Shifts for RIS elements	28
		3.1.2	Signal Model	29
	3.2	Statist	cical Distribution of SINR	30
	3.3	Perfor	mance Evaluation	30
		3.3.1	Calculation of OP at U_2	30
		3.3.2	Calculation of OP at U_1	32
		3.3.3	System Throughput	32
	3.4	Simula	ation Results and Discussion	33
	3.5	Summ	ary	36
4	Wir	eless	Powered RIS-assisted Cognitive NOMA Network with	
	Har	\mathbf{dware}	Impairments: IBL and FBL Analysis	37
	4.1	System	a Model	38
		4.1.1	System Description	38
		4.1.2	Channel Model	40
		4.1.3	Energy Harvesting and Information Transmission	40
			4.1.3.1 For Infinite Blocklength	40
			4.1.3.2 For Finite Blocklength	41
		4.1.4	Signal Model	41
	4.2	Chann	nel Statistics	42
	4.3	Infinit	e Blocklength Analysis	43
		4.3.1	Calculation of OP at U_1	44
			Calculation of OP at U_2	44

Contents

		4.3.3	Asymptotic OP analysis	45
			4.3.3.1 Asymptotic OP at $U_1 \ldots \ldots \ldots \ldots$	45
			4.3.3.2 Asymptotic OP at U_2	45
		4.3.4	System throughput	46
	4.4	Finite	blocklength Analysis	46
		4.4.1	Block-Error Rate Preliminaries	46
		4.4.2	Calculation of ABLER at U_1	47
		4.4.3	Calculation of ABLER at U_2	48
		4.4.4	Asymptotic ABLER analysis	48
			4.4.4.1 Asymptotic ABLER for $U_1 \ldots \ldots \ldots \ldots$	48
			4.4.4.2 Asymptotic ABLER for U_2	49
		4.4.5	Goodput Analysis	49
		4.4.6	Latency and Reliability Analysis	49
	4.5	Simula	ation Results and Discussion	50
		4.5.1	Infinite Blocklength Transmission	51
		4.5.2	Finite Blocklength Transmission	54
	4.6	Cumm	nary	60
	4.0	Summ	ici	00
5				
5	Fin	ite Bl	ocklength Analysis of ARIS-FDTW Communication with	
5	Fin	ite Bl	ocklength Analysis of ARIS-FDTW Communication with	1 62
5	Fini Har	ite Bl	ocklength Analysis of ARIS-FDTW Communication with Impairments	62 62
5	Fini Har	ite Bl dware Syster	ocklength Analysis of ARIS-FDTW Communication with Impairments n Model	62 62 63
5	Fini Har	ite Bl rdware Syster 5.1.1 5.1.2	ocklength Analysis of ARIS-FDTW Communication with Impairments n Model	62 62 63 64
5	Find Har 5.1	ite Bl rdware Syster 5.1.1 5.1.2	ocklength Analysis of ARIS-FDTW Communication with Impairments n Model	62 62 63 64 65
5	Find Har 5.1	ite Bl rdware Syster 5.1.1 5.1.2 Perfor	ocklength Analysis of ARIS-FDTW Communication with Impairments n Model	62 62 63 64 65 65
5	Find Har 5.1	ite Blackware System 5.1.1 5.1.2 Perfor 5.2.1	ocklength Analysis of ARIS-FDTW Communication with Impairments Impairments Model	62 62 63 64 65 65
5	Find Har 5.1	ite Bl rdware Syster 5.1.1 5.1.2 Perfor 5.2.1 5.2.2	ocklength Analysis of ARIS-FDTW Communication with Impairments In Model	62 62 63 64 65 65 66
5	Find Har 5.1	Syster 5.1.1 5.1.2 Perfor 5.2.1 5.2.2 5.2.3	ocklength Analysis of ARIS-FDTW Communication with Impairments In Model	62 62 63 64 65 65 66 66
5	Find Har 5.1	System 5.1.1 5.1.2 Perfor 5.2.1 5.2.2 5.2.3 5.2.4 5.2.5	ocklength Analysis of ARIS-FDTW Communication with Impairments In Model	62 62 63 64 65 65 66 66 67
5	Fin: Har 5.1	System 5.1.1 5.1.2 Perfor 5.2.1 5.2.2 5.2.3 5.2.4 5.2.5 Simula	ocklength Analysis of ARIS-FDTW Communication with Impairments In Model	62 62 63 64 65 65 66 67 67
5	Fin: Har 5.1 5.2	ite Blackware System 5.1.1 5.1.2 Perfor 5.2.1 5.2.2 5.2.3 5.2.4 5.2.5 Simulation	ocklength Analysis of ARIS-FDTW Communication with Impairments In Model	62 62 63 64 65 65 66 67 67 68 72
	Fin: Har 5.1 5.2 5.3 5.4 Per	ite Blackware System 5.1.1 5.1.2 Perfor 5.2.1 5.2.2 5.2.3 5.2.4 5.2.5 Simulation Summ	ocklength Analysis of ARIS-FDTW Communication with Impairments In Model	62 62 63 64 65 65 66 67 67 68 72

xii

		6.1.1	Channel	$\operatorname{Model} \ \ldots \ldots \ldots \ldots \ldots \ldots \ldots \ldots \ldots$	75
			6.1.1.1	ES Protocol	75
			6.1.1.2	MS and TS Protocol	77
		6.1.2	STAR-R	IS assisted SP-OMA	77
		6.1.3	Statistica	al Distribution	77
	6.2	Perfor	mance Ev	aluation	78
		6.2.1	ABLER	Preliminaries	78
		6.2.2	Calculati	ion of ABLER at U_1	79
		6.2.3	Calculati	ion of ABLER at U_2	80
		6.2.4	Asympto	otic ABLER Analysis	80
			6.2.4.1	Asymptotic ABLER at U_1	80
			6.2.4.2	Asymptotic ABLER at U_2	81
		6.2.5	System 7	Throughput and Goodput	81
		6.2.6	Latency	and Reliability	81
	6.3	Simula	tion Resu	alts and Discussion	82
	6.4	Summ	ary		90
7	Con	clusio	and Fu	ture Work	91
	7.1	Conclu	ision		91
	7.2	Future	Work .		93
\mathbf{A}	App	oendix			94
	A.1	Deriva	tion of (3	.9) and (3.10)	94
	A.2	Deriva	tion of (3	.11) and (3.12)	94
	A.3	Deriva	tion of (4	19)	95
	A.4	Deriva	tion of (4	20)	95
	A.5	Deriva	tion of (5	.6)	96
Re	efere	nces			97
Li	st of	Public	cations		110

List of Figures

2.1	Notion of smart radio environment	12
2.2	Illustration of Varactor diode type RIS	13
2.3	Illustration of RIS-assisted SISO communication	14
2.4	Concept of STAR-RIS	16
2.5	Different operating protocols of STAR-RIS	17
3.1	RIS aided downlink NOMA network	27
3.2	Outage Probability vs. Transmit SNR for $K=24.$	31
3.3	Comparison of outage probability of scenario-(c) vs. transmit SNR with	
	scenario-(a) and scenario-(b)	34
3.4	Comparison of outage probability of scenario-(c) with different values of K .	34
3.5	Comparison of system throughput for scenario-(c) with scenario-(a) and	
	scenario-(b) vs. transmit SNR	35
4.1	Wireless powered downlink RIS-assisted cognitive NOMA network	39
4.2	Timing diagram for a) IBL transmission, b) FBL transmission	39
4.3	Comparison of OP vs. transmit power	51
4.4	Comparison of OP vs. transmit power for varying K	52
4.5	Comparison of OP vs. transmit power for varying HIs	52
4.6	Comparison of OP vs. transmit power for varying N	53
4.7	Comparison of OP vs. transmit power for varying L	54
4.8	Comparison of OP vs. time splitting factor (α)	55
4.9	Comparison of system throughput vs. transmit power	56
4.10	Comparison of ABLER vs. transmit power	56
4.11	Comparison of ABLER vs. transmit power for varying K	57
4.12	Comparison of ABLER vs. blocklength	58
4.13	Comparison of goodput vs. transmit power	58
4.14	Comparison of latency and reliability vs. transmit power	59
4.15	Comparison of latency and reliability vs. blocklength	59
5.1	ARIS-assisted FDTW network	63

xiv List of Figures

5.2	Comparison of ABLER vs. transmit power with conventional FDTW-AF	
	and FDTW-DF relay systems	69
5.3	Comparison of ABLER vs. transmit power with varying HI parameters	69
5.4	Comparison of EC vs. transmit power with varying HI parameters	70
5.5	Comparison of ABLER and EC vs. LI power	70
5.6	Comparison of system throughput/goodput vs. transmit power	71
5.7	Comparison of latency vs. transmit power	71
6.1	STAR-RIS assisted downlink SP-NOMA system	74
6.2	ABLER vs. transmit SNR	
6.3	Comparison of ABLER vs. transmit SNR for all STAR-RIS protocols	83
6.4	Comparison of ABLER vs. transmit SNR for varying ipCSI factor (ζ)	84
6.5	Comparison of ABLER vs. transmit SNR for varying ip SIC factor $(\psi).$	84
6.6	ABLER vs. blocklength	85
6.7	System throughput vs. transmit SNR	86
6.8	System goodput vs. transmit SNR	87
6.9	Latency vs. transmit SNR	87
6.10	Reliability vs. transmit SNR	88
6.11	Latency and reliability vs. blocklength.	88

List of Tables

3.1	Simulation Parameters for RIS-NOMA	33
4.1	Simulation Parameters for RIS-CR-NOMA	50
5.1	Simulation Parameters for ARIS-FDTW system	68
6.1	Simulation Parameters for STAR-RIS-SP-NOMA	82

Acronyms

1G First Generation **2D** Two Dimensional **2G** Second Generation **3G** Third Generation **3GPP** Third Generation Partnership Project 4G Fourth Generation **5G** Fifth Generation **6G** Sixth Generation **ABLER** Average Block Error Rate **AF** Amplify and Forward AP Access Point **AR** Augmented Reality ARIS Active Reconfigurable Intelligent Surface AWGN Additive White Gaussian Noise **B5G** beyond Fifth Generation **BER** Bit Error Rate **BS** Base Station CD Code Domain **CDF** Cummulative Distribution Function CDMA Code Division Multiple Access

CLT Central Limit Theorem

Acronyms xvii

CR Cognitive Radio

CSI Channel State Information

DF Decode and Forward

DoF Degree of Freedom

EC Ergodic Capacity

EE Energy Efficiency

EGC Equal Gain Combining

EH Energy Harvesting

EM Electromagnetic

eMBB Enhanced Mobile Broadband

ES Energy Splitting

EVM Error Vector Magnitude

 ${f FBL}$ Finite Blocklength

FD Full Duplex

FDMA Frequecy Division Multiple Access

FDTW Full Duplex Two Way

FPGA Field Programmable Gate Array

GCQ Gauss Chebyshev Quadrature

GLQ Gauss Laguerre Quadrature

GPS Global Positioning System

HD Half Duplex

HI Hardware Impairment

 ${f IBL}$ Infinite Blocklength

xviii Acronyms

IoT Internet of Things

ISAC Integerated Sensing and Communication

ISI Inter Symbol Interference

IT Information Transmission

ITU International Telecommunication Union

LI Loop Interference

LOS Line of Sight

LTE Long Term Evolution

MIMO Multiple Input Multiple Output

MISO Multiple Input Single Output

MS Mode Switching

MTC Machine Type Communication

NGMA Next Generation Multiple Access

 ${f NOMA}$ Non-Orthogonal Multiple Access

OFDM Orthogonal Frequency Division Multiple Access

OMA Orthogonal Multiple Access

OP Outage Probability

PA Power Allocation

PD Power Domain

PDF Probability Density Function

PIN Positive Intrinsic Diode

PN Primary Network

PRIS Passive Reconfigurable Intelligent Surface

Acronyms

PU Primary User

QoS Quality of Service

RF Radio frequency

RIS Reconfigurable Intelligent Surface

SE Spectral Efficiency

SIC Successive Interference Cancellation

SIDNR Signal to Interference plus Distortion and Noise

SIMO Single Input Multiple Output

SINR Signal to Interference plus Noise Ratio

SISO Single Input Single Output

 ${f SN}$ Secondary Network

SNR Signal-to-Noise Ratio

SP Short Packet

SPC Short Packet Communication

SRE Smart Radio Environment

STAR Simultaneously Transmitting and Reflecting

SU Secondary User

TDMA Time Division Multiple Access

TS Time Switching

UAV Unmanned Aerial Vehicle

URLLC Ultra Reliable and Low Latency Communication

VLC Visible Light Communication

VR Virtual Reality

Chapter 1

Introduction

1.1 Development of Wireless Communications

The advent of wireless communications is seen as a significant breakthrough in the field of technology, revolutionizing the way individuals communicate with one another across the globe. Wireless communications enable the transmission of data from one point to the other without the necessity of any cables or wires. Guglielmo Marconi's invention of radiotelegraphy in the late 19th century marks the beginning of wireless communications development [1]. A significant milestone was achieved early in the 20th century when Marconi sent a signal across the Atlantic Ocean, illustrating the practicality of wireless signal transmission over vast distances [2]. The initiation of theoretical analysis in wireless communication was characterized by Claude E. Shannon's information theory in 1948. Before Shannon's work, the design and optimization of wireless communication systems were primarily grounded in empirical findings. Shannon recognized the constraints of this type of approach and concentrated on a strictly mathematical basis for comprehending the information conveyed through communication networks [3]. Claude E. Shannon's paper, "A Mathematical Theory of Communication", is now widely acknowledged as the cornerstone of contemporary communication technology research [4].

The beginning of commercial and industrial wireless communication systems is traceable back to the inception of First Generation (1G) wireless communication networks. This technology used analog signals to enable wireless voice communication by employing Frequency Division Multiple Access (FDMA) [5]. To date, the evolution of wireless communication networks has been characterized by five distinct generations, driven by advancements in communication theory and hardware technology. Wireless communication networks were first introduced in the 1980s. The wireless networks moved to the Second Generation (2G) networks in the 1990s due to issues with spectrum efficiency, quality of service, and security in 1G. Digital technology-enabled 2G wireless networks offered improved communication quality and facilitated the provision

of additional data services, including text messages [6]. Early in the 2000s, Third Generation (3G) wireless networks were implemented primarily due to a significant increase in mobile communication devices, marking considerable improvements over their 2G counterparts. 3G networks achieved faster data speeds and offered a wider array of services, such as internet browsing, Global Positioning System (GPS) applications, and mobile apps, using packet switching, Code Division Multiple Access (CDMA), and wideband CDMA (WCDMA) technologies [7]. The introduction of smartphones coincided with a substantial increase in mobile data usage. The adoption of advanced technologies like Orthogonal Frequency Division Multiple Access (OFDM) and Multiple Input Multiple Output (MIMO) systems facilitated Fourth Generation (4G) wireless networks to provide faster data rates and reduced latency, thereby making it possible for high-quality video streaming, online gaming, and live video conferencing to be delivered on mobile devices [8]. Extensive roll-out of Fifth Generation (5G) wireless communication networks has taken place across a large number of countries since 2020. The cutting-edge 5G wireless technology is anticipated to provide improved connectivity, faster data transfer speeds, and less delay than previous iterations. The 5G wireless technology has the capability to support a range of innovative technologies, including the Internet of Things (IoT), autonomous driving, Virtual Reality (VR), and Augmented Reality (AR). Thanks to several pivotal technologies, such as massive MIMO, millimeter-wave communications, network slicing, and so forth [9]. 5G networks offer uninterrupted connectivity, higher data rates, extensive connectivity, and lower latency. New technologies like AR, VR, the tactile internet, holographic teleportation, and self-driving cars necessitate extremely low latency and exceptionally high dependability. Various applications of 5G networks have distinct objectives including focusing on latency, reliability, availability, and bandwidth requirements. The division of works on 5G networks into three primary service categories is contingent on these prerequisites, which include Ultra Reliable and Low Latency Communication (URLLC), massive Machine Type Communication (MTC), and Enhanced Mobile Broadband (eMBB) use cases. The three use cases suggested by the International Telecommunication Union (ITU) are designed to meet demanding performance criteria, including minimal latency and dependability, high data throughput, and massive connectivity.

Wireless communication networks are poised for significant transformation approximately every decade to meet the growing demand for connectivity. Global internet protocol data traffic is projected to increase by an impressive 55% annually, reaching a remarkable

5016 exabytes annually by 2030. Additionally, the number of connected mobile devices is expected to soar to 25.9 billion by 2025, underscoring the necessity for innovative solutions [10]. In response, academia and industry are exploring way towards next-generation, i.e., Sixth Generation (6G) technologies. Recent research has highlighted groundbreaking innovations such as Visible Light Communication (VLC) [11], Integerated Sensing and Communication (ISAC) [12], Reconfigurable Intelligent Surface (RIS) [13], Next Generation Multiple Access (NGMA) [14] and non-terrestrial networks [15], all of which present exciting possibilities for the future of connectivity. In this thesis, our focus is towards RIS-assisted communication systems. Therefore, we will discuss the capabilities of RIS and Non-Orthogonal Multiple Access (NOMA) in this section.

1.1.1 Motivation for using Reconfigurable Intelligent Surfaces

The limitations of existing wireless networks in accommodating the increasing demands for communication services necessitate the development and implementation of innovative wireless communication systems that incorporate advanced technologies. Among the various physical layer technologies being explored for next-generation wireless networks, RIS has emerged as a focal point of research interest, recognized for its potential to revolutionize future wireless communication frameworks [13]. A significant advantage of RIS technology lies in its capacity to enhance spectrum efficiency, a critical component in the realm of wireless communications. The inherently unpredictable and uncontrollable nature of wireless propagation environments poses substantial challenges to achieving reliable and efficient communication [16]. In contrast to traditional approaches like conventional relays, RIS technology presents a viable solution for establishing a controllable wireless propagation environment. An RIS comprises of a planar array of numerous reflecting elements, each of which can be manipulated by an RIS controller to execute real-time, independent phase shifts of incoming signals [17]. By leveraging Channel State Information (CSI), RIS can intelligently reconfigure the wireless propagation landscape by adjusting the phase shifts of its elements, thereby enabling constructive signal combinations directed toward specific angles. This capability not only facilitates spatial signal enhancement but also significantly improves spectrum efficiency, marking a substantial advancement in wireless communication technology [18].

The potential of RIS to proactively alter the wireless communication environment has made them a central topic of research aimed at addressing various issues prevalent in different wireless networks, mainly at the physical layer. By employing a smart controller, such as a Field Programmable Gate Array (FPGA), the phase and amplitude of these reconfigurable elements can be adeptly controlled, thus enabling the reconfiguration of wireless signal propagation and the establishment of a "Smart Radio Environment (SRE)" [19, 20]. Additionally, the absence of Radio frequency (RF) chains in RIS technology renders it a more economical and environmentally friendly option than conventional multi-antenna and relaying technologies. The advantages associated with RISs are outlined as follows:

- Improved signal quality: RISs can enhance the quality of wireless signals by dynamically altering the propagation environment. They can control the phase, amplitude, and polarization of signals, improving signal strength and reducing interference.
- Flexible deployment: RISs are almost passive devices. They are made from Electromagnetic (EM) materials and can be utilized across a wide range of structures. These include building facades, indoor walls, aerial platforms, roadside billboards, highway poles, vehicle windows, and even clothing worn by pedestrians, largely because of their low-cost nature.
- Spectral efficiency enhancement: The capability of RISs to reshape the wireless propagation environment allows for the compensation of power losses experienced over long distances. They achieve this by passively reflecting incoming radio signals and forming virtual Line of Sight (LOS) links between Base Station (BS) and mobile users. The increase in throughput is especially significant when the direct LoS connection is hindered by obstacles like tall buildings. With the thoughtful deployment and design of RISs, a software-defined wireless environment can be established, which enhances the received Signal-to-Noise Ratio (SNR).
- Energy efficiency: Unlike traditional relaying systems such as Amplify and Forward (AF) and Decode and Forward (DF), RISs have the ability to manipulate the incoming signal by adjusting the phase shift of each reflective element, rather than relying on a power amplifier. Consequently, implementing RISs is more energy-efficient and environmentally sustainable than conventional AF and DF systems.
- Scalability and compatibility: RISs are capable of supporting Full Duplex (FD) and full-band transmission, primarily because they reflect EM waves without

alteration. Moreover, wireless networks enhanced by RIS technology are designed to be compatible with the standards and equipment of existing wireless infrastructures.

1.1.2 Motivation for using Simultaneous Transmitting and Reflecting Reconfigurable Intelligent Surfaces

Despite the aforementioned advantages being noteworthy, current research predominantly addresses RISs that solely reflect incident signals. This limitation necessitates that both the signal source and destination reside on the same side of the RIS, specifically within the same half-space of the SRE. Such geographical constraints may not always be feasible in real-world scenarios, thereby significantly curtailing the adaptability and efficacy of RISs, as users are often situated on both sides of the surface. To address this challenge, the innovative concept of Simultaneously Transmitting and Reflecting (STAR) RISs (STAR-RISs) has been introduced [21]. In this framework, a wireless signal that strikes a STAR-RIS element from either side is bifurcated into two components: one that is reflected back into the same space (region) as the incident signal and another that is transmitted into the opposite space. Research indicates that by adjusting both the electric and magnetic currents of a STAR-RIS element, the characteristics of the transmitted and reflected signals can be modified through two generally independent parameters known as the transmission and reflection coefficients. This capability enables the realization of a highly adaptable 360° SRE. Based on the distinctive characteristics outlined above, the implementation of STAR-RISs offers several benefits to wireless communication systems:

- STAR-RISs possess the unique capability to simultaneously transmit and reflect the incoming signals, increasing their coverage to include the entire spatial environment. This characteristic permits a single RIS to cater to both half-spaces, a possibility that conventional reflecting-only RISs cannot achieve.
- STAR-RISs offer improved Degree of Freedom (DoF) for manipulating signal propagation, thereby greatly enhancing the design flexibility necessary to meet rigorous communication requirements.
- The design of STAR-RISs often emphasizes optical transparency, rendering them both visually attractive and compatible with established building designs, including window structures. Thus, STAR-RISs are unlikely to create any adverse aesthetic effects, a consideration that is critical for their practical use.

1.1.3 Motivation for using Non Orthogonal Multiple Access

By the end of 2023, Cisco predicted that mobile users would reach 13.1 billion, and internet-enabled devices would grow from 18.4 billion in 2018 to 29.3 billion in 2023 [22]. This surge in demand is expected to strain the connectivity capabilities of wireless communication networks. With 70% of the global population driving this growth, the trend is likely to persist. To address these challenges, providing massive connectivity has become a key goal for 6G networks. Critical performance targets for 6G include peak data rates of at least one terabit per second, air interface latency of the order of 0.01–0.1 milliseconds, 10 times the connectivity density of 5G, 5–10 times higher Spectral Efficiency (SE), 10–100 times Energy Efficiency (EE), and reliability exceeding 99.99% [23], [24]. Historically, Orthogonal Multiple Access (OMA) techniques like FDMA in 1G, Time Division Multiple Access (TDMA) in 2G, CDMA in 3G, and OFDMA in 4G were widely adopted due to their low complexity and interference avoidance. In particular, OMA pertains to an orthogonal allocation of resources (frequency, time slot, signature code, and other resource block) to distinct users.

The rapid proliferation of IoT, smart devices, heterogeneous services, applications like AR/VR, autonomous vehicles, tele-surgery, tactile internet, and digital twins are accelerating the advancement of 5G networks, necessitating reevaluation of multiple access technologies [25]. NOMA, recently introduced for Third Generation Partnership Project (3GPP) Long Term Evolution (LTE), is anticipated to offer enhanced spectral efficiency [26]. Furthermore, NOMA has been identified as having the potential for integration with existing multiple access frameworks, as it leverages the power domain as an additional dimension. The fundamental principle of NOMA is to facilitate the simultaneous service of multiple users within a single resource block (such as time, frequency, or code) through the implementation of Successive Interference Cancellation (SIC), distinguishing it from traditional OMA technologies like FDMA, TDMA, CDMA, and OFDMA. This approach is motivated by NOMA's ability to utilize spectrum more effectively by taking advantage of varying user channel conditions and its capacity to accommodate multiple users with diverse Quality of Service (QoS) needs within the same resource allocation [27]. The classification of NOMA techniques is fundamentally divided into two categories. The first, termed Power Domain (PD) NOMA (PD-NOMA), pertains to the scenario in which the signals from different users are superimposed and differentiated by specific power allocation coefficients. Conversely, Code Domain (CD) NOMA (CD-NOMA) is utilized when users' signals overlap, yet they are assigned different codes for distinction [28].

1.2 Thesis Contributions

The contributions of this thesis are listed below.

- 1. Performance analysis of a novel phase shift matrix design for RIS-assisted NOMA.
 - (a) We have designed a phase shift matrix of RIS that combines the components from RIS elements with coherent phases across both users.
 - (b) The closed-form expression for the user's Outage Probability (OP) and system throughput are derived.
 - (c) The Monte-Carlo simulations are also presented to verify the closed-form expressions.
- 2. Performance analysis of wireless-powered RIS-assisted cognitive NOMA networks with Hardware Impairments (HIs) using Infinite Blocklength (IBL) and Finite Blocklength (FBL) codes.
 - (a) We analyzed a wireless-powered RIS-assisted downlink NOMA for a cognitive IoT network in which a secondary source harvests energy from a multiantenna power beacon to transmit information to the secondary user in an underlay mode.
 - (b) For the IBL analysis, we derived the novel analytical expressions for OP and system throughput. The asymptotic expression of OP is also derived at higher transmit power.
 - (c) For the FBL analysis, we derived the novel analytical expressions of ABLER, goodput, latency, and reliability. The asymptotic expression of Average Block Error Rate (ABLER) is also derived at higher transmit power.
 - (d) The Monte-Carlo simulations are also presented to verify the analytical results.
- 3. Performance analysis of Active Reconfigurable Intelligent Surface (ARIS)-assisted Full Duplex Two Way (FDTW) communication with HIs using FBL codes.
 - (a) We analyzed the performance of ARIS-FDTW communication in the presence of HIs over cascaded Rician fading channels under the FBL regime.
 - (b) We derived the novel analytical expressions for ABLER, Ergodic Capacity (EC), system throughput, goodput, and latency. The asymptotic expression of ABLER and EC are derived at higher transit power regimes.

- (c) The Monte-Carlo simulations are also presented to verify the analytical expressions.
- 4. Performance analysis of STAR-RIS assisted Short Packet (SP) NOMA system under imperfect SIC (ipSIC) and imperfect CSI (ipCSI).
 - (a) We analyze the downlink STAR-RIS assisted SP-NOMA network under ipSIC and ipCSI conditions over the cascaded Nakagami-*m* fading environment.
 - (b) We derived novel analytical expressions for ABLER, system throughput, goodput, and latency under perfect CSI (pCSI), ipCSI, perfect SIC (pSIC) and ipSIC scenarios. The asymptotic expression of ABLER is also derived at higher transmit power.
 - (c) The Monte-Carlo simulations are also presented to verify the analytical expressions.

1.3 Thesis Organization

This thesis is divided into seven chapters. A brief content of each of the following chapters is summarized below.

Chapter 2: In this chapter, some background information to this thesis is presented. Firstly, the basics of different types of RISs, such as Passive Reconfigurable Intelligent Surface (PRIS), ARIS, and STAR-RIS, and their characteristics are described. Then, the basics of the power domain NOMA and the introduction of FBL analysis are covered. Finally, we present the extensive literature review for the RIS, ARIS, and STAR-RIS-assisted NOMA, Cognitive Radio (CR), and FDTW communication in the IBL and FBL regimes.

Chapter 3: In this chapter, we have analyzed the performance of a new design of the RIS-assisted NOMA system by considering all the elements of RIS to provide coherent phase shifts to both users in a NOMA pair. In addition, we have designed a phase shift matrix of RIS that combines the components from RIS elements with coherent phases across both users. The closed-form expression for the user's OP is derived using the Gauss Chebyshev Quadrature (GCQ) and moment-matching method to assess the system performance. Also, system throughput is evaluated in a delay-limited transmission mode. Numerical results reveal that our proposed system model of RIS-NOMA achieves better OP and higher system throughput than the other existing scenarios of RIS-NOMA

networks. Finally, the Monte-Carlo simulations are also presented to verify the closed-form expressions.

Chapter 4: This chapter investigates the performance of a wireless-powered RIS-assisted CR-NOMA network with HIs. In the secondary network, the secondary source harvests its energy wirelessly from the multiantenna power beacon for its operation. The secondary source operates in underlay mode to communicate with the near user through a direct link, and the far user is served with the help of RIS, under the multiantenna primary user constraint. We have analyzed the performance in the IBL and FBL transmission under the practical constraints of HI and imperfect SIC. We have derived the novel closed-form expression for the OP and system throughput for the IBL transmission. In contrast, for the FBL transmission, we have derived the closed-form expression for the ABLER, goodput, latency, and reliability. The asymptotic analysis for the OP and ABLER is also presented in two different power-setting scenarios: 1) when the transmit power of the power beacon goes to infinity and 2) when the maximum interference constraint of the primary network goes to infinity. Monte Carlo simulations are performed to verify the analytical results. Numerical results indicate the superior performance of the combination of RIS and NOMA in the considered system over RIS-assisted OMA schemes. The impact of other parameters, such as the number of antennas at the power beacon, the number of antennas at the primary user, the number of RIS elements, time-splitting factor, HIs, blocklength, and ipSIC on the system performance, is also examined.

Chapter 5: This chapter investigates the performance of ARIS-FDTW communication in the presence of HIs over cascaded Rician fading channels under the FBL regime. We derived novel analytical expressions for ABLER, EC, system throughput, goodput, and latency. The asymptotic expressions of ABLER and EC are also derived at higher transmit power. Monte Carlo simulations were performed to verify the analytical results. Numerical results revealed the superior performance of the ARIS-FDTW system compared to its passive counterpart and conventional FDTW-AF and FDTW-DF relay systems.

Chapter 6: This chapter analyzes the performance of the downlink STAR-RIS-aided SP-NOMA (STAR-RIS-SP-NOMA) network under the constraint of ipSIC and ipCSI under Nakagami-*m* fading environment. To characterize the system performance,

firstly, we derive the statistical distribution of cascaded Nakagami-m channels using the Laguerre polynomial series approximation. Secondly, the approximate closed-form expression in terms of ABLER, system throughput, goodput, latency, Thirdly, we have compared the ABLER expression for and reliability are derived. all three operating protocols of STAR-RIS. Additionally, we have also compared the performance of STAR-RIS-assisted short packet NOMA with STAR-RIS-assisted SP-OMA (STAR-RIS-SP-OMA) and the conventional cooperative communication scenarios such as DF-relay assisted-Half Duplex (HD)-SP-OMA (DF-HD-SP-OMA) and fixed gain AF-relay assisted-HD-SP-OMA (AF-HD-SP-OMA). The asymptotic analysis is also done at a high SNR regime to gain further insights. Finally, the Monte-Carlo simulation is performed to verify the correctness of the theoretical results. Numerical results validate the superiority of STAR-RIS-SP-NOMA over STAR-RIS-SP-OMA, DF-HD-SP-OMA, and AF-HD-SP-OMA scenarios. Also, the effect of various parameters, such as the ipCSI correlation factor, ipSIC factor, blocklength, and number of STAR-RIS elements on the system performance, is examined.

Chapter 7: This chapter presents the conclusions of the thesis and also provides new insights on future research directions.

Chapter 2

Background and Literature Review

2.1 Smart Radio Environment

The role of RIS is projected to be fundamental in creating an SRE for next-generation wireless communication networks [20]. It encompasses a variety of physical objects that can significantly affect the transmission of EM waves between devices. These waves are often subject to attenuation and multipath propagation. This impairs the communication performance severely at times. Attenuation is primarily due to material absorption and path loss, while multipath propagation results from reflection, diffraction, and refraction, leading to small-scale fading and Inter Symbol Interference (ISI). The wireless environment is shaped by the location, materials, and geometry of physical objects, which cannot be dynamically altered or modeled to adapt to communication services. To counteract the unpredictable nature of the wireless environment, several advanced communication strategies have been employed on the device side, including the use of massive MIMO systems and relays. However, these solutions may introduce challenges related to hardware scalability and mobility. As illustrated in Figure 2.1, the conceptual vision of a SRE encompasses the joint optimization of the transmitter, receiver, and wireless surroundings to enhance communication performance. One innovative method for creating an SRE is the implementation of software-controlled RISs that can interact with various physical objects in the environment, including walls and furniture. This capability allows for the dynamic reconfiguration of the radio environment to satisfy a range of performance demands.

2.2 RIS Fundamentals

A RIS is defined as a Two Dimensional (2D) material configuration that allows for the programming of macroscopic physical attributes. Numerous adjustable surface designs are being considered as potential candidates for realizing RISs. In [20], the authors elucidated a key difference between natural and artificial materials, particularly RISs, indicating that natural materials possess uniform EM properties in their tangential directions,

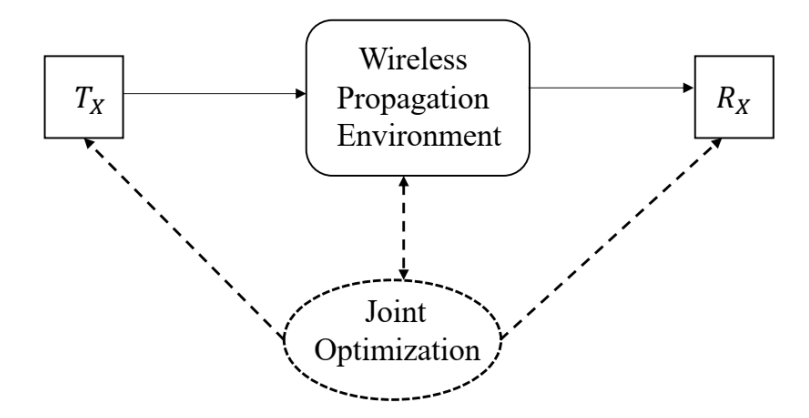


Figure 2.1: Notion of smart radio environment.

while artificial materials tend to exhibit either periodic or quasi-periodic characteristics. RISs can be generally classified into two categories based on their periodic structures: Patch-array-based RIS and metasurface-based RIS. They are briefly discussed as follows:

2.2.1 Patch-array-based RIS:

Patch-array RISs are formed from periodic cells that are several centimeters in size, allowing for tunability by incorporating elements such as Positive Intrinsic Diode (PIN) diodes or delay lines. In patch-array-based RISs, the elements utilize PIN diodes or varactor diodes to establish phase-shift states, as shown in Figure 2.2. The overall power consumption is divided into two components: the static power consumption associated with the control circuit and the dynamic power consumption of each individual element. The power consumption of the control circuit varies with the size of the RIS, ranging from 0.72 watts (W) to 10 W. When employing PIN diodes for phase-shift control, each diode typically consumes 0.33 milliwatts (mW) when in the "ON" state [29]. In [30], the authors detailed a prototype that is based on an implementation utilizing PIN diodes. This approach is recognized as the most common design for both RISs and STAR-RISs, owing to the affordability and voltage-controlled characteristics of PIN diodes. However, a limitation of this approach is that PIN diodes operate in only two states, "ON" and "OFF," which restricts the implementation to a finite set of reflection and transmission coefficients.

2.2.2 Metasurface-based RIS:

Metasurface RISs consist of periodic cells that can be as small as a few millimeters, micrometers, or even at the molecular level, which requires more intricate control over their EM properties, including conductivity and permittivity. A notable example of a

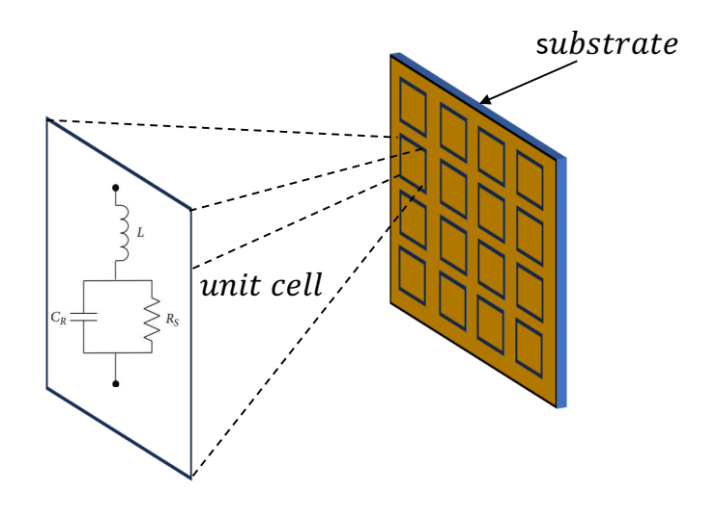


Figure 2.2: Illustration of Varactor diode type RIS.

metasurface-based RIS is the transparent dynamic metasurface developed by researchers at NTT DOCOMO in Japan. As indicated in [31], this metasurface facilitates the manipulation of 28 GHz 5G radio signals, enabling dynamic control over both the reflection and transmission of the signals while preserving the transparency of the window. However, a significant limitation is its lack of dynamic reconfiguration capabilities, which are typically found in implementations utilizing PIN diodes. Additionally, modifications to the distance between substrates can influence the reflection coefficient of the entire surface rather than allowing for the reconfiguration of individual elements.

2.2.3 Statistical Channel Modeling of RIS assisted Communication

Consider a RIS-assisted Single Input Single Output (SISO) system, as shown in Figure 2.3. A BS, S, with a single antenna, communicates with the single antenna destination user (D) through the direct link as well as with the RIS (R). RIS is considered to have N elements. The direct link channel gain between S and D is denoted by h_{SD} , the channel gain vector from S to R_n^{th} RIS element is $\mathbf{h}_{SR} = [h_{SR_1}, h_{SR_2} \cdots h_{SR_N}]^T$, and the channel gain vector from R_n^{th} RIS element to D is denoted as $\mathbf{h}_{RD} = [h_{R_1D}, h_{R_2D} \cdots h_{R_ND}]^T$. The phase shift matrix for the RIS elements can be denoted as $\Theta = diag\{\sqrt{\beta_1}e^{j\theta_1}, \sqrt{\beta_2}e^{j\theta_2} \cdots \sqrt{\beta_N}e^{j\theta_N}\}$, where θ_n is the phase shift of the n^{th} element and β_n is the amplitude of n^{th} RIS element, respectively. In the case of PRIS, it is possible to adjust the phase shift angles; however, the amplitude coefficients remain fixed. Typically, the value of $0 \le \beta_n \le 1$. Therefore, the total channel gain from S to D can be represented as

$$y_D = \sqrt{P_s} (\boldsymbol{h}_{RD}^T \Theta \boldsymbol{h}_{SR} + h_{SD}) x + \eta$$
 (2.1)

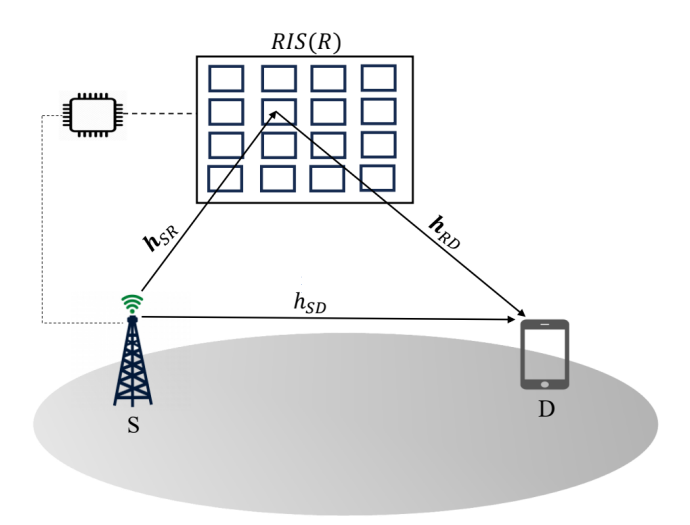


Figure 2.3: Illustration of RIS-assisted SISO communication.

where P_s is the transmit power of S, x is the transmitted symbol from S with $\mathbb{E}\{|x|^2\}=1$ and η is the Additive White Gaussian Noise (AWGN) denoted by $\eta \sim \mathcal{CN}(0, \sigma^2)$. The received SNR at D can be expressed as

$$\gamma_D = \frac{P_s \left| \boldsymbol{h}_{RD}^T \boldsymbol{\Theta} \boldsymbol{h}_{SR} + h_{SD} \right|^2}{\sigma^2}$$

$$= \frac{P_s \left| \sum_{n=1}^N h_{R_n D} \beta_n e^{j\theta_n} h_{SR_n} + h_{SD} \right|^2}{\sigma^2}$$
(2.2)

Here, γ_D can be improved by optimizing θ and the maximization problem can be formulated as

$$\max_{\theta, \beta} \left| \sum_{n=1}^{N} h_{R_n D} \beta_n e^{j\theta_n} h_{SR_n} + h_{SD} \right|^2$$
s.t. $0 \le \theta_n \le 2\pi$, (2.3)
$$0 \le \beta_n \le 1.$$

Therefore, the objective function $\left|\sum_{n=1}^{N}h_{R_{n}D}\beta_{n}e^{j\theta_{n}}h_{SR_{n}} + h_{SD}\right|^{2} = \left|\sum_{n=1}^{N}\beta_{R_{n}D}\beta_{n}e^{j(\theta_{n}+\phi_{SR_{n}}+\phi_{R_{n}D})}\beta_{SR_{n}} + \beta_{SD}e^{j\phi_{SD}}\right|^{2}$ can be maximized if $\theta_{n} = mod(\phi_{SD} - \phi_{SR_{n}} - \phi_{R_{n}D}, 2\pi)$, where mod is the modulus operator. This is called coherent phase shift scheme or coherent addition of signals [17, 19, 32].

2.3 Active RIS

Despite having several advantages of PRIS, conventional PRIS yields only marginal capacity improvements in various scenarios where the direct link is strong. This limitation is attributed to the "multiplicative fading" effect associated with RISs, wherein the

equivalent path loss of the transmitter-RIS-receiver link is calculated as the product of the path losses of the transmitter-RIS and RIS-receiver links. This product is typically several orders of magnitude smaller than the path loss of the direct link. As a result, the "multiplicative fading" effect significantly hinders PRISs from realizing substantial capacity gains in numerous wireless settings. Thus, to promote the feasibility of RISs in future 6G wireless networks, a crucial issue that needs to be addressed is: How can the inherent performance constraints imposed by the "multiplicative fading" effect be mitigated?

In response to this fundamental physical limitation of wireless communication systems, [33], [34] proposes a new architecture of RIS known as ARIS. In contrast to PRISs, which reflect signals without amplification, ARISs are characterized by their capacity to amplify and reflect signals actively. This functionality is made possible by integrating reflection-type amplifiers [35] into the reflective elements of the RIS. While this method does incur additional power consumption, ARISs have the potential to counteract the substantial path loss of reflected links, thereby offering a viable strategy to address the issue of "multiplicative fading." Although ARIS entails a slightly higher expense due to the integration of low-power amplifiers compared to PRIS, it remains more cost-effective than traditional repeaters, such as AF and DF relays [33] A subconnected structure for ARIS was proposed in [36] to allow for independent phase shift regulation of each element. The application of ARIS in wireless communications was explored, revealing that the performance of ARIS-assisted links improves with more active elements.

2.4 STAR-RIS

STAR-RIS is a concept in wireless communication technology to further enhance the conventional RIS capabilities. Unlike conventional RIS, which only reflects signals, STAR-RIS simultaneously enables signal reflection and refraction (transmission). This offers greater flexibility and improved performance in wireless systems [21]. As depicted in Figure 2.4, when a wireless signal is incident on an element of a STAR-RIS from either side of the surface, it is split into two distinct parts [37], the reflected signal and the transmitted signal.

2.4.1 Signal Model of STAR-RIS

In Figure 2.4, it is demonstrated that the wireless signal incident upon a designated element of the STAR-RIS is divided into two distinct signals: one that is transmitted and

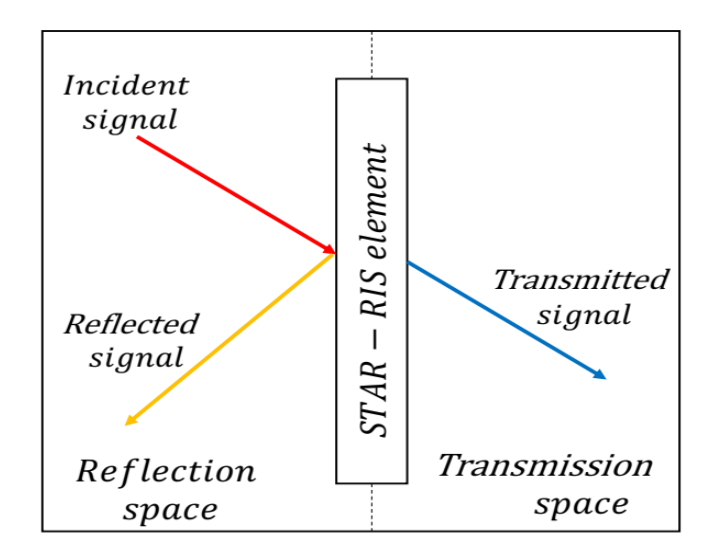


Figure 2.4: Concept of STAR-RIS.

another that is reflected. To characterize this feature of the STAR-RIS, let s_n denote the signal that arrives at the n^{th} element of the STAR-RIS, where n is an element of the set $\mathcal{N}=1,2,\cdots,N,$ with N signifying the total number of elements present. The transmitted and reflected signals associated with the n^{th} element can be modeled as $t_n=\left(\sqrt{\beta_m^t}e^{j\theta_n^t}\right)s_n$ and $r_n=\left(\sqrt{\beta_n^r}e^{j\theta_n^r}\right)s_n$, respectively, where, $\sqrt{\beta_n^t},\sqrt{\beta_n^r}\in[0,1]$ and $\theta_n^t,\theta_n^r\in[0,2\pi)$ denotes the amplitude and phase shift response for transmission and reflection coefficient for the n^{th} element of the STAR-RIS. The amplitude adjustment parameters, i.e., $\sqrt{\beta_n^t}$ and $\sqrt{\beta_n^r}$ are coupled to each other by the law of conservation of energy. According to this law, the total energy of the transmitted and reflected signals for any given element must never be greater than the energy of the incident signal, accordingly $|t_n|^2 + |r_n|^2 = |s_n|^2$, which leads to the condition on the amplitude of transmission and reflection coefficient of each element as $\beta_n^t + \beta_n^r = 1$.

2.4.2 Operating Protocols for STAR-RIS

By properly adjusting the amplitude coefficient for transmission and reflection, a given element of STAR-RIS can be operated in full reflection ($\beta_n^t = 0$, $\beta_n^r = 1$ referred as R mode), full transmission ($\beta_n^t = 1$, $\beta_n^r = 0$, referred as T mode) and the general simultaneous transmission and reflection (β_n^t , $\beta_n^r \in [0,1]$). Inspired by these, authors in [37] proposed three operating protocols for STAR-RIS, namely Energy Splitting (ES), Mode Switching (MS), and Time Switching (TS), as illustrated in Figure 2.5.

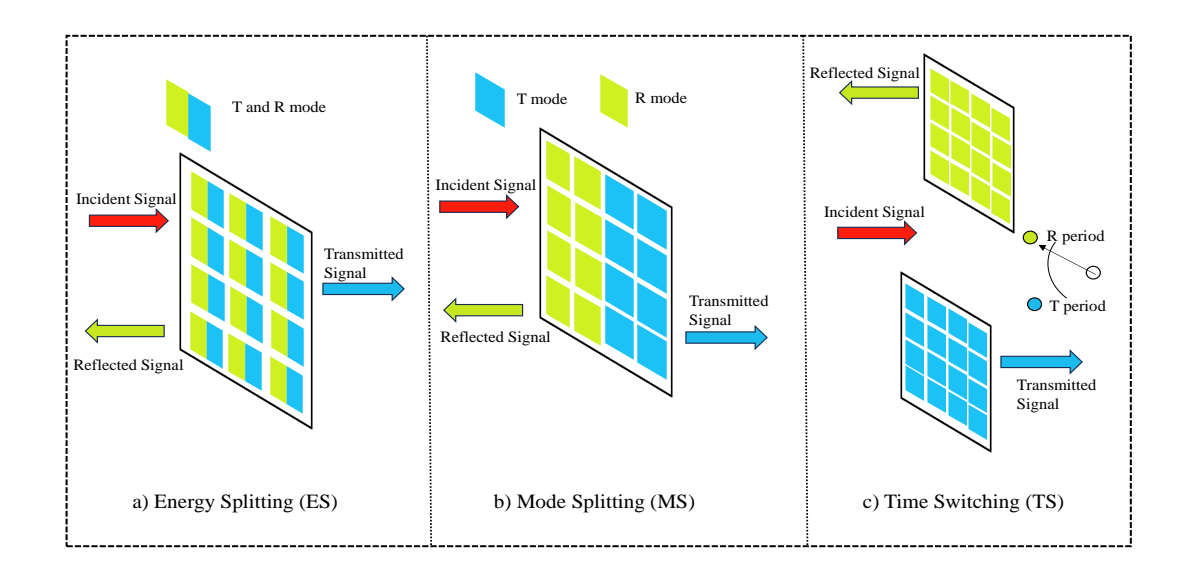


Figure 2.5: Different operating protocols of STAR-RIS.

2.4.2.1 Energy splitting (ES):

In the ES mode, every element of the STAR-RIS system can function in both transmission and reflection modes concurrently. In this operational framework, the energy associated with the incoming signal that interacts with each individual element is typically divided into two distinct forms: the energy that is transmitted and the energy that is reflected. This division of energy is characterized by a specific ratio, denoted as $\beta_n^t:\beta_n^r$, which quantifies the proportion of energy allocated to each of the transmitted and reflected signals. In this framework, the transmission and reflection coefficient matrices are given as $\Theta_t^{ES} = diag\{\sqrt{\beta_1^t}e^{j\theta_1^t},\sqrt{\beta_2^t}e^{j\theta_2^t}\cdots\sqrt{\beta_1^t}e^{j\theta_N^t}\}$ and $\Theta_r^{ES} = diag\{\sqrt{\beta_1^r}e^{j\theta_1^r},\sqrt{\beta_2^r}e^{j\theta_1^r},\sqrt{\beta_2^r}e^{j\theta_2^r}\cdots\sqrt{\beta_1^r}e^{j\theta_N^r}\}$, respectively, where $\beta_n^t,\beta_n^r \in [0,1],\beta_n^t+\beta_n^r=1$ and $\theta_n^t,\theta_n^r \in [0,2\pi) \forall n \in \mathcal{N}$.

2.4.2.2 Mode switching (MS):

In MS mode, elements of the STAR-RIS are categorized into two distinct groups. One group consists of N_t elements that function in full transmission mode, while the other group comprises N_r elements that operate in full reflection mode, where $N_t + N_r = N$. The transmission and reflection coefficient matrices are given as $\Theta_t^{MS} = diag\{\sqrt{\beta_1^t}e^{j\theta_1^t}, \sqrt{\beta_2^t}e^{j\theta_2^t} \cdots \sqrt{\beta_1^t}e^{j\theta_{N_t}^t}\}$ and $\Theta_r^{MS} = diag\{\sqrt{\beta_1^r}e^{j\theta_1^r}, \sqrt{\beta_2^r}e^{j\theta_2^r} \cdots \sqrt{\beta_1^r}e^{j\theta_{N_r}^r}\}$, respectively, where $\beta_n^t, \beta_n^r \in \{0, 1\}$, and $\theta_n^t, \theta_n^r \in [0, 2\pi) \forall n \in \mathcal{N}$. It is important to understand that MS mode in STAR-RISs can be seen as a special case of ES mode in STAR-RISs.

2.4.2.3 Time switching (TS):

The TS mode of STAR-RIS operates differently from ES and MS by utilizing the time domain and periodically switching all its elements between two modes: the transmission mode and the reflection mode. This switching occurs in distinct orthogonal time slots, known as the T and R periods, as illustrated in Figure 2.5. Let $0 < \lambda_t < 1$ and $0 < \lambda_t < 1$, $\lambda_t + \lambda_1 = 1$ be the fractions of time allocated to T and R period respectively. The corresponding transmission and reflection matrices can be represented as $\Theta_t^{TS} = diag\{e^{j\theta_1^t}, e^{j\theta_2^t} \cdots e^{j\theta_N^t}\}$ and $\Theta_r^{TS} = diag\{e^{j\theta_1^r}, e^{j\theta_2^r} \cdots e^{j\theta_N^r}\}$, respectively, where $\theta_n^t, \theta_n^r \in [0, 2\pi) \forall n \in \mathcal{N}$.

2.5 PD-NOMA

PD-NOMA represents a method in wireless communication that enables multiple users to utilize the same time-frequency resources by assigning varying power levels to their respective signals. In a typical downlink scenario, a BS transmits superimposed signals to two users, designated as U_1 (strong user) and U_2 (weak user). The superimposed transmitted signal can be represented as

$$x = \sqrt{\alpha_1} s_1 + \sqrt{\alpha_2} s_2 \tag{2.4}$$

where α_1 and α_2 are the Power Allocation (PA) levels assigned for transmission to U_1 and U_2 respectively. s_1 and s_2 are the symbols transmitted to U_1 and U_2 , respectively. On the receiver's side, the received signals at U_1 and U_2 can be respectively expressed as

$$y_1 = h_1 \sqrt{\alpha_1} s_1 + h_1 \sqrt{\alpha_2} s_2 + \eta_1 \tag{2.5}$$

$$y_2 = h_2 \sqrt{\alpha_1} s_1 + h_2 \sqrt{\alpha_2} s_2 + \eta_2 \tag{2.6}$$

where h_i is the channel coefficient and η_i is the AWGN for $U_i, i \in \{1, 2\}$. Since U_1 has a better channel condition, it first decodes the U_2 signal before decoding its own signal. Therefore Signal to Interference plus Noise Ratio (SINR) for decoding s_2 at U_1

$$SINR_{1\to 2} = \frac{|h_1|^2 \alpha_2}{|h_1|^2 \alpha_1 + \sigma^2} \tag{2.7}$$

If U_1 successfully decodes s_2 , it subtracts s_2 from the received signal (SIC process). The remaining signal at U_1

$$\hat{y}_1 = h_1 \sqrt{\alpha_1} s_1 + \eta_1 \tag{2.8}$$

Therefore, the SNR at U_1 to decode its own signal is

$$SNR_1 = \frac{|h_1|^2 \alpha_1}{\sigma^2} \tag{2.9}$$

Furthermore, U_2 can not perform SIC and treats s_1 as noise while decoding its own signal s_2 . Thus SINR at U_2 is

$$SINR_1 = \frac{|h_2|^2 \alpha_2}{|h_2|^2 \alpha_1 + \sigma^2} \tag{2.10}$$

2.6 Finite Blocklength Transmission

Historically, each successive generation of cellular systems has primarily aimed to achieve significant improvements in data transmission rates compared to its predecessor. However, 5G and beyond Fifth Generation (B5G) represent a shift in this paradigm: their emphasis extends beyond merely enhancing broadband services and increasing data rates. This shift is necessitated by the fact that a substantial proportion of wireless connections in 5G are expected to be initiated by autonomous machines and devices rather than by human-operated mobile terminals. The B5G is expected to cater to the unique requirements of these autonomous entities by introducing two innovative wireless communication modes: URLLC and massive machine-to-machine communications [38], [39]. In recent years, the advancements in B5G and subsequent communication technologies have significantly enhanced network transmission capabilities. This progress has catalyzed the evolution of the IoT era, facilitating pervasive connectivity across various sectors, including intelligent industries, smart transportation, and smart homes [40], thereby enabling the interconnection of all devices [41]. Numerous essential IoT applications demand exceptionally ultra-high reliability (99.99%) and ultra-low latency (<1ms) [42], [43]. However, traditional long packet communication (IBL), which is prevalent, tends to exhibit considerable transmission delays due to the extended time required for coding and decoding processes associated with larger packet sizes. In contrast, Short Packet Communication (SPC) allows for the transmission of information in the range of hundreds of bits, thereby notably decreasing transmission delays [44], [45]. Moreover, in many IoT communication scenarios, the data transmitted typically consists of commands, status updates, or sensor readings, which can be effectively conveyed through short data packets. Consequently, SPC emerges as a defining characteristic of IoT. It is important to note that Shannon's capacity formula becomes inapplicable in the context of SPC, as the law of large numbers does not hold. Thus, it is essential to reassess the achievable data rates in SPC. Therefore, Polyanskiy et al. [46] investigated SPC in the context of AWGN channels from an information-theoretic viewpoint. Their research led to the formulation of an approximation for the maximum achievable rate, represented as a complex function dependent on the SNR, blocklength, and the decoding error probability.

2.7 Literature Review

The performance analysis of RIS/STAR-RIS-assisted communication has been extensively reported in the literature in terms of IBL and FBL regimes over various fading channels. The performance metrics considered are OP, EC, and Bit Error Rate (BER) for IBL transmission and ABLER for FBL transmission. Firstly, we will provide a summary of the literature on the IBL performance of RIS/STAR-RIS-assisted communication, and then we will discuss the literature on the FBL analysis.

2.7.1 Literature on IBL analysis for RIS/STAR-RIS assisted communication

The RIS, alternatively referred to as the Intelligent Reflecting Surface (IRS) or Large Intelligent Surface (LIS), has attracted growing interest from researchers and industry professionals. This surge in attention is due to its potential to alter the propagation environment and improve the quality of signal reception [13, 17, 20, 47]. In [48, 49], the authors demonstrated the enhanced performance of RIS compared to conventional relay-assisted networks regarding hardware expenses and energy consumption. Owing to the mathematical intricacies involved in addressing the cascaded fading channels of the RIS, most of the works have resorted to deriving the outage probability via approximations or inequalities. In [19], [50], the authors utilized the Central Limit Theorem (CLT) to evaluate the OP of the RIS-assisted SISO system with Rayleigh fading. However, with the CLT approach, there is a considerable difference between the analytical and the simulation results when dealing with a few reflecting elements. To address this issue, the authors in [51] analyzed the OP of the RIS-assisted SISO system with the K_G distribution. In [52], the authors used the Rician fading environment to investigate the OP and BER of RIS-assisted Unmanned Aerial Vehicle (UAV) using a mixture Gamma approximation method. Furthermore, to obtain a simpler expression of OP, the authors of [53, 54]

used Gamma approximation to model the cascaded channel of RIS by using the Laguerre series. In [55], the authors analyzed the OP for the RIS-assisted Multiple Input Single Output (MISO) system over Rician fading. In [56], the authors investigated the statistical characterization and performance analysis of multi-RIS-assisted communication under a Nakagami-m fading environment.

The above-mentioned studies [50, 51, 52, 53, 54, 55, 56] assume pCSI is available at the RIS controller, which facilitates the optimal selection of phase shifts to enhance the manipulation of incoming signals. However, the realization of pCSI at the RIS depends on extensive channel estimation, which leads to substantial signaling overhead and increased energy consumption. Additionally, it is crucial to acknowledge that channel estimation errors are largely inevitable. Channel estimation errors result from quantization errors and unpredictable noise disturbances. In [57], the authors investigated the OP performance of RIS-assisted communication by considering the imperfect estimation of the channel from RIS to the user. In [58], the performance of an uplink RIS-assisted Single Input Multiple Output (SIMO) system was investigated under ipCSI. Furthermore, in [59], the authors investigated the OP and EC of an ARIS and PRIS-assisted MISO communication with discrete phase shifts and ipCSI.

CR, FDTW communication, and NOMA are identified as the essential technologies for the next generation of wireless networks to further improve overall SE. The adoption of CR facilitates the sharing of the same spectrum among different network types, thereby optimizing spectrum usage through intelligent sensing and decision-making processes [60]. The systems that allow users to send and receive messages over the same channel simultaneously, known as FDTW communication, may considerably enhance SE and throughput [61]. However, while the FD system increases the overall SE, it also limits the system performance due to imperfect self-interference cancellation. In this context, owing to various analog and digital self-interference cancellation techniques [62], FDTW communication emerges as a promising technique to double SE and reduce latency. At the same time, NOMA permits multiple users to access the same frequency, time, or code resources, which potentially improves SE, fairness, and overall connectivity [27]. Because of the advantages mentioned above, researchers have begun to study the coexistence of RIS with CR [63, 64, 65, 66, 67], RIS with FDTW [53, 68, 69, 70, 71, 72, 73], RIS with NOMA [74, 75, 76, 77, 78, 79, 80, 81, 82] and RIS with CR and NOMA [83, 84, 85, 86, 87] to get benefit from the complementary nature of these technologies. Implementing NOMA enhances the SE, while RISs facilitate the effective and intelligent customization of users'

propagation environment to improve overall communication performance.

Dongfang et al. [63] investigated the resource allocation in RIS-assisted FD-CR systems. In [64], the authors aimed to maximize the weighted sum rate of RIS-assisted MIMO-CR network. In [65], the authors investigated the multiple RIS-assisted downlink MIMO-CR system to maximize the achievable sum rate of the Secondary User (SU). In [66], the weighted sum rate of SUs for the RIS-assisted CR system is maximized by jointly optimizing the transmit precoding matrix at the Secondary Network (SN) base station and the reflection phase shift of the RIS. In [67], the authors maximize the secrecy EE by simultaneously optimizing transmit beamforming at a multi-antenna cognitive base station and passive beamforming at the RIS.

In view of RIS-assisted FDTW communication, the authors in [53] analyzed the performance of RIS-assisted FDTW communication with reciprocal and non-reciprocal channels under Rayleigh fading. Furthermore, in [68, 69], the authors investigated the performance of the RIS-FDTW system under Rayleigh fading. In another pertinent study [70], the authors investigated the performance of RIS-FD communication under the Nakagami-m fading environment by considering a separate RIS to assist both user transmissions. In [71], the authors investigated the performance of the RIS-FDTW system with the practical constraint of external EM interference. In another relevant study [72], the authors analyzed the performance of RIS-FDTW communication under the effect of ipCSI over Rayleigh fading In [73], the authors analyzed the performance of a RIS-FD system where an FD Access Point (AP) simultaneously communicates with the uplink and downlink user with the help of RIS.

Considering RIS-NOMA, the authors in [74] compared RIS-NOMA to NOMA without RIS and OMA with/without RIS, which have discrete unit-modulus reflection constraints on each RIS element. In [75], the performance of RIS-NOMA was characterized by the OP and the EC over Nakagami-m fading channels for uplink and downlink scenarios. Further, the authors of [76] used coherent phase and random phase shifting to study the outage probability of RIS-NOMA networks. In [77], the authors investigated the uplink performance of the RIS-NOMA network under Nakagami-m fading by using the moment matching method. In [78], the authors investigated the OP, and EC of RIS-NOMA networks, using a 1-bit coding scheme of programming metamaterials to consider both ipSIC and pSIC. A similar kind of approach to design of RIS-NOMA that provides an in-depth comprehension of the co-existence of RIS and NOMA was studied in [79]. In [80], the authors proposed a NOMA network which is aided by multiple RISs with discrete phase

shifts where an RIS serves each user to improve the quality of the received signal. In [81], the authors analyzed the error performance for RIS-aided downlink NOMA system for two user and multiuser scenarios with the help of two RISs. In [82], the authors investigated the OP and EC for ARIS-assisted NOMA by considering hardware impairments under Nakagami-m fading environment. In [83], an EE maximization problem is investigated in an underlay RIS-CR-NOMA system. In [84], the authors investigated the performance of the downlink underlay RIS-CR-NOMA network under the Rayleigh fading environment, and a deep learning framework is used to predict the EC. In [85], the authors analyzed the OP for the non-terrestrial RIS-CR-NOMA under the Rician fading environment. In [86], the authors investigated the performance of the ARIS-assisted CR-NOMA network under Nakagami-m fading. In [87], the authors aimed at maximizing the weighted sum rate and EE for the ARIS-assisted CR-NOMA space-air-ground integrated network.

The latest innovation in metasurfaces, STAR-RIS, facilitates signal passage through these substrates through refraction [21],[37]. In contrast to conventional RISs with half-space SREs, STAR-RISs achieve a versatile full-space SRE. This capability allows for separate beamforming of reflection and refraction, greatly enhancing the adaptability of STAR-RIS coverage areas [88]. Hence, integrating STAR-RIS into NOMA systems can achieve full-space coverage without any blind spots, which brings STAR-RIS-aided NOMA a high research value. In [89], the authors investigated the weighted sum rate of STAR-RIS-assisted NOMA. In [90], the authors investigated the OP for all three operating protocols of the STAR-RIS-assisted NOMA network. In [91], the authors investigated the closed-form expression of OP and EC for STAR-RIS-assisted NOMA network with a Rician fading environment. Furthermore, by considering the random location of the users, the authors in [92] investigated the EC of the STAR-RIS-assisted NOMA network with Nakagami-m fading. In [93], the closed-form expression for the coverage probability and EC is investigated for the STAR-RIS-assisted multicell NOMA network by using the stochastic geometry-based location of the devices. In [94], the author investigated the ergodic sum rate for the STAR-RIS assisted uplink NOMA under ipCSI and hardware impairments.

2.7.2 Literature on FBL analysis RIS/STAR-RIS assisted communication

The aforementioned research contributions have laid a solid groundwork for the deployment of RIS-CR [63, 64, 65, 66, 67], RIS-NOMA [74, 75, 76, 77, 78, 80] and

STAR-RIS-NOMA [89, 90, 91, 92, 93, 94] networks, showcasing their benefits extensively in the existing literature. However, most current studies have focused on IBL transmission or long packet transmission. Solely depending on NOMA technology does not adequately meet the URLLC demands of future generations IoT networks. Furthermore, various IoT application scenarios, including smart grids, autonomous driving, e-health, and industrial automation, require only minimal data exchange between nodes. In contrast, employing SPC to transmit only a few hundred bits of data significantly reduces transmission latency. As a result, FBL transmission, or SPC, is increasingly acknowledged as a defining characteristic of IoT communication. In this context, the foundations of Shannon's capacity theory become increasingly inapplicable, and the assurance of reliable transmission at very high SNR is compromised. To fill the theoretical gap present in the FBL system, Polyanskiy et al. [46] established a relationship between achievable rate, decoding error probability, and transmission delay. They proposed the ABLER as a performance indicator to evaluate the effectiveness of the FBL transmission system.

Therefore, exploring the potential of SPC in conjunction with RIS and NOMA is worthwhile. Initially, authors in [95] investigated how phase error and other hardware limitations affected the performance of RIS-aided URLLC systems, while the authors in [96] investigated the performance of RIS-aided URLLC systems and derived the average data rate and average decoding error probability under correlated and uncorrelated Nakagami-m fading channels. In [97], the authors used the Nelder-Mead simplex approach to tackle the challenge of ultra-high reliability in URLLC using a mobile UAV and RIS in an SPC scenario. Furthermore, the authors in [98] explored the potential of RIS-assisted FD communication with non-linear energy harvesting in an industrial automation scenario. In [99], the authors aimed to maximize the EE for the STAR-RIS-assisted MIMO URLLC system. In [100], the authors investigated the joint reliability and beamforming design for the STAR-RIS-assisted multiuser MISO URLLC system. Furthermore, the authors in [101] investigated the sum rate maximization problem for the multi-STAR-RIS assisted FD-URLLC system using meta-learning and deep deterministic policy gradient methodology. In [102], the performance of RIS-assisted SP-NOMA was investigated using optimal and random phase shifts with pSIC and ipSIC under Rayleigh fading. To make further development in this direction, the authors in [103] investigated the performance of RIS-assisted SP-NOMA by using discrete phase shifts and continuous phase shifts under Nakagami-m fading channels. In [104], the authors investigated a downlink RIS-NOMA system with SPC under the effect of hardware impairments at the transceiver nodes. In [105], FBL analysis was reported for ABLER and goodput for the downlink STAR-RIS assisted SP-NOMA system under Nakagami-m fading. Further, the authors in [106] analyzed an MS protocol with partition strategies for the STAR-RIS-assisted SP-NOMA to serve multiple actuators simultaneously for reducing STAR-RIS design cost. In [107], the performance of STAR-RIS-assisted SP-NOMA with discrete phase shifts is analyzed under a statistical CSI scenario. In [108], the authors maximize the SE in STAR-RIS-assisted SP-NOMA with ipCSI. In [109], the authors considered uplink STAR-RIS-NOMA with FBL for IoT networks to maximize the achievable rate in the IoT devices present on the reflection space of STAR-RIS while guaranteeing the reliability for the IoT device present on the transmission space of STAR-RIS.

Chapter 3

A Novel Paradigm for RIS-NOMA Transmission

Existing works on RIS-assisted NOMA networks majorly target the single user in the NOMA pair, i.e., assisted with RIS [80, 76, 77]. The works that target both users in the NOMA pair follow the splitting of the elements of RIS (i.e., half of the elements of RIS are optimized to serve one user, and the remaining elements are optimized to serve the other user). To serve multiple users with a single RIS, an On-Off control scheme (1-bit encoding) was proposed in [78]. Similarly, serving multiple users with multiple RIS in RIS-NOMA networks with coherent phase shifts to each user was investigated in [79, 80]. The combination of element splitting with two RISs to serve multiple users in the RIS-NOMA network was recently done in [81]. However, to the best of the authors' knowledge, none of the existing work has investigated the problem of serving both the users in the NOMA pair with RIS by considering all the elements to provide coherent phase shifts to both users, which is the novel aspect of the proposed approach.

In this chapter, we analyzed the performance of a new design of the RIS-NOMA system by considering all the elements of RIS to provide coherent phase shifts to both users in a NOMA pair. In addition, we have designed a phase shift matrix of RIS that combines the components from RIS elements with coherent phases across both users. The closed-form expression for the user's OP is derived using the GCQ and moment-matching method to assess the system performance. Also, system throughput is evaluated in a delay-limited transmission mode. Numerical results reveal that our proposed system model of RIS-NOMA achieves better OP and higher system throughput than the other existing scenarios of RIS-NOMA networks. Finally, the Monte-Carlo simulations are also presented to verify the closed-form expressions.

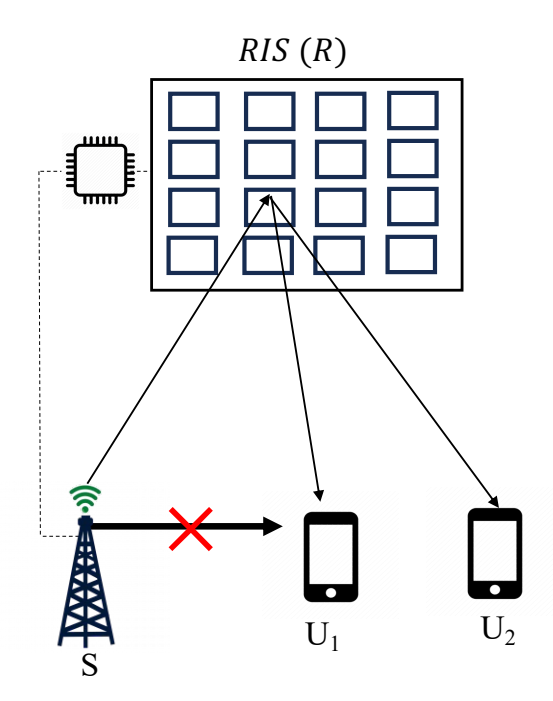


Figure 3.1: RIS aided downlink NOMA network.

3.1 System Model

We consider a RIS-aided downlink NOMA system with a source (S) that provides service to a near user (U_1) and a far user (U_2) with the help of a RIS (R) that is equipped with K number of passive reflecting elements as shown in Figure 3.1. It is also assumed that S, U_1 , and U_2 have a single antenna. We consider the scenario in which S cannot communicate directly with either of the users due to the presence of blockages. However, communication with the users is possible through the RIS. We denote h_{XY} to be the wireless channel link coefficient from transmitter $X \in \{S, R_k\}$ to receiver $Y \in \{R_k, U_1, U_2\}$, where R_k with $k \in \{1, 2, \dots, K\}$ is the k^{th} element of R. The wireless channel links are assumed to be independent but not necessarily identically distributed Rayleigh fading as in [76, 78, 79]. The effective path loss (in dB) is denoted by $A_{dB}(d_{XY}) = 35.1 + 36.7 \log_{10}(d_{XY}) - G_X - G_Y$, where d_{XY} is the distance¹ between transmitter and receiver with $X \in \{S, R\}$ and $Y \in \{R, U_1, U_2\}$, G_X and G_Y represent the antenna gains at the transmitter and receiver, respectively.

According to NOMA principle, S sends a superimposed signal $x = \sum_{i=1}^{2} \sqrt{\alpha_i P_s} x_i$, where x_i is the message intended for U_i , complying with $E\{|x_i|^2\} = 1$. Here, P_s represent the transmitted power of the source and α_i is the PA coefficient for U_i , with $i \in \{1, 2\}$ that

¹We assume RIS to be operated in the far field regime; therefore, $d_{SR} = \{d_{SR_k}\}_{k=1}^K$ and $d_{RU_i} = \{d_{R_kU_i}\}_{k=1}^K$ and inter-elements spacing greater than half wavelength.

satisfies $\alpha_2 > \alpha_1$ and $\alpha_1 + \alpha_2 = 1$. Therefore, the received signal at U_i is represented as

$$y_{U_i} = \frac{1}{\sqrt{A(d_{SR}) A(d_{RU_i})}} \left(\sum_{k=1}^K h_{SR_k} \Phi_k h_{R_k U_i} \right) x + n_{U_i}$$
 (3.1)

where $A(d_{XY})$ is the absolute value corresponding to $A_{dB}(d_{XY})$ and n_{U_i} is the AWGN with zero mean and variance σ_i^2 and Φ_k is the reflection coefficient introduced by the k^{th} element of R.

3.1.1 Design of Phase Shifts for RIS elements

Now, we consider the sum SNR for the NOMA user pair, i.e., the sum of received SNR at U_1 and U_2 , to design the phase shifts for RIS elements such that a coherent combination is received across the users in the NOMA pair. Let's represent the first term of (3.1) alternatively using the product of two vectors as

$$y_{U_i} = \frac{1}{\sqrt{A(d_{SR}) A(d_{RU_i})}} \left(\mathbf{\Phi}^H \mathbf{h_i}\right) x + n_{U_i}$$
(3.2)

where $\mathbf{h_i} = [h_{SR_1}h_{R_1U_i}, h_{SR_2}h_{R_2U_i}, \cdots, h_{SR_K}h_{R_KU_i}]^T$ represents the cascaded channel coefficient of the links from S to U_i through k^{th} element of RIS and $\mathbf{\Phi}^H = [\Phi_1, \Phi_2, \cdots, \Phi_K]$. From (3.2), it can be observed that SNR at user U_i is proportional to $|A_i\mathbf{\Phi}^H\mathbf{h_i}|^2$ with $A_i = \frac{1}{\sqrt{A(d_{SR})A(d_{RU_i})}}$. So, the sum SNR is proportional to $|A_1\mathbf{\Phi}^H\mathbf{h_1}|^2 + |A_2\mathbf{\Phi}^H\mathbf{h_2}|^2$. The sum SNR proportionality can be further represented as

$$|A_1 \mathbf{\Phi}^H \mathbf{h_1}|^2 + |A_2 \mathbf{\Phi}^H \mathbf{h_2}|^2 \le |\mathbf{\Phi}^H (A_1 \mathbf{h_1} + A_2 \mathbf{h_2})|^2$$
 (3.3)

We further consider the maximization of the right-hand side of the above expression. Using Cauchy-Schwarz² inequality, the phase shift vector corresponding to a maximum of $\left|\mathbf{\Phi}^{H}\left(A_{1}\mathbf{h_{1}}+A_{2}\mathbf{h_{2}}\right)\right|^{2}$ can be obtained as

$$\mathbf{\Phi} \propto (A_1 \mathbf{h_1} + A_2 \mathbf{h_2}) \tag{3.4}$$

Now, k^{th} component of Φ is represented as $\Phi_k = \left(c_1 e^{-j\phi_{U_1}^k} + c_2 e^{-j\phi_{U_2}^k}\right)$ with $\phi_{U_1}^k$ being the phase corresponding to k^{th} component of $\mathbf{h_1}$, $\phi_{U_2}^k$ being the phase corresponding to k^{th} component of $\mathbf{h_2}$ and c_1 and c_2 are corresponding magnitudes. This way the proportionality in (3.4) violates when $|A_1\mathbf{h_1}| \neq |A_2\mathbf{h_2}|$. Further, realizing proportionality in (3.4) is not possible for PRIS because the magnitude of the reflection coefficient cannot

²The dot product (or the inner product) of two vectors a and b then: $|a.b| \leq |a|.|b|$.

be > 1. However, the multiple components reaching the receiver from RIS elements combine in coherent phases, equivalent to Equal Gain Combining (EGC) with unity gain for all components. Next, we discuss the SINR formulation and related statistics that are required for OP and throughput analysis of the system.

3.1.2 Signal Model

For the formulation of SINR, we represent the received signal as represented in (3.1) and (3.2) as

$$y_{U_i} = (\Psi_{1,i} + \Psi_{2,i}) x + n_{U_i} \tag{3.5}$$

where, $\Psi_{1,i} = A_i \sum_{k=1}^K \left(h_{SR_k} c_1 e^{-j\phi_{U_1}^k} h_{R_{kU_i}}\right)$ and $\Psi_{2,i} = A_i \sum_{k=1}^K \left(h_{SR_k} c_2 e^{-j\phi_{U_2}^k} h_{R_{kU_i}}\right)$ for $i \in \{1,2\}$. The k^{th} component of the phase shift vector $\mathbf{\Phi}$ i.e., Φ_k is combination of phase information of k^{th} component of $\mathbf{h_1}$ and that of $\mathbf{h_2}$. For U_1 , $\phi_{U_1}^k = -arg\left(h_{SR_k}\right) - arg\left(h_{R_kU_1}\right)$ accounts for coherent phase shifts [76, 77] resulting in maximized SNR at U_1 . Thus, $|\Psi_{1,1}| = A_1 |\sum_{k=1}^K h_{R_kU_1} c_1 e^{j\phi_{U_1}^k} h_{SR_k}| = c_1 A_1 \sum_{k=1}^K |h_{R_kU_1}| |h_{SR_k}|$. Similarly, for U_2 , $\phi_{U_2}^k = -arg\left(h_{SR_k}\right) - arg\left(h_{R_kU_2}\right)$ accounts for coherent phase shifts to maximize the SNR at U_2 . Thus, $|\Psi_{2,2}| = A_2 |\sum_{k=1}^K h_{R_kU_2} c_2 e^{-j\phi_{U_2}^k} h_{SR_k}| = c_2 A_2 \sum_{k=1}^K |h_{R_kU_2}| |h_{SR_k}|$. Furthermore, for U_1 , $\phi_{U_2}^k$ accounts for random phase shift [76, 77] and thus $|\Psi_{2,1}| = A_1 |\sum_{k=1}^K h_{R_kU_1} c_2 e^{-j\phi_{U_2}^k} h_{SR_k}|$. Similarly, for U_2 , $\phi_{U_1}^k$ accounts for random phase shifts and $|\Psi_{1,2}| = A_2 |\sum_{k=1}^K h_{R_kU_2} c_1 e^{-j\phi_{U_1}^k} h_{SR_k}|$. Using the NOMA principle, the far user (U_2) can directly decode its signal by considering the near user (U_1) signal as noise. Accordingly, the SINR at U_2 can be written as

$$\Upsilon_2 = \frac{\alpha_2 \rho \left| \Psi_{2,2} + \Psi_{1,2} \right|^2}{\alpha_1 \rho \left| \Psi_{2,2} + \Psi_{1,2} \right|^2 + 1}$$
(3.6)

where, $\rho = \frac{P_s}{\sigma^2}$ denotes the transmit SNR. Conversely, by using SIC, U_1 decodes its signal, x_1 by first decoding x_2 and treating x_1 as interference. Therefore, the instantaneous SINR of decoding x_2 at U_1 is

$$\Upsilon_{12} = \frac{\alpha_2 \rho |\Psi_{1,1} + \Psi_{2,1}|^2}{\alpha_1 \rho |\Psi_{1,1} + \Psi_{2,1}|^2 + 1}$$
(3.7)

Practically, SIC implementation may lead to decoding errors, also known as ipSIC. But, in our work, we assume pSIC. Therefore, if x_2 is successfully decoded and removed, then the instantaneous SNR for decoding x_1 at U_1 is

$$\Upsilon_1 = \alpha_1 \rho |\Psi_{1,1} + \Psi_{2,1}|^2 \tag{3.8}$$

3.2 Statistical Distribution of SINR

Following the steps as discussed in Appendix A.1, the Cummulative Distribution Function (CDF) and Probability Density Function (PDF) of $|\Psi_{2,2}|^2$ can be written as

$$\mathcal{F}_{|\Psi_{2,2}|^2}(x) = \frac{\gamma\left(\Lambda_{|\Psi_{2,2}|}, \frac{\sqrt{x}}{\lambda_{|\Psi_{2,2}|}}\right)}{\Gamma\left(\Lambda_{|\Psi_{2,2}|}\right)},\tag{3.9}$$

$$f_{|\Psi_{2,2}|^2}(x) = \frac{(\sqrt{x})^{\left(\Lambda_{|\Psi_{2,2}|} - 2\right)} e^{\frac{-\sqrt{x}}{\lambda_{|\Psi_{2,2}|}}}}{2\Gamma\left(\Lambda_{|\Psi_{2,2}|}\right) \lambda_{|\Psi_{2,2}|}^{\Lambda_{|\Psi_{2,2}|}}},$$
(3.10)

where, $\Gamma(\cdot)$ and $\gamma(\cdot, \cdot)$ are the Gamma and lower incomplete gamma functions respectively. Similar to (3.9) and (3.10), the CDF and PDF of $|\Psi_{1,1}|^2 = \left(c_1 A_1 \sum_{k=1}^K |h_{SR_k}| |h_{R_k U_1}|\right)^2$ can be obtained suitably by interchanging the subscripts of $|\Psi_{2,2}|$ to $|\Psi_{1,1}|$ in (3.9) and (3.10) respectively. By using the steps as discussed in Appendix A.2, the CDF and PDF of $|\Psi_{1,2}|^2$ can be written as

$$\mathcal{F}_{|\Psi_{1,2}|^2}(y) = 1 - \exp\left(\frac{-y}{\Omega_{|\Psi_{1,2}|}}\right),$$
 (3.11)

$$f_{|\Psi_{1,2}|^2}(y) = \frac{1}{\Omega_{|\Psi_{1,2}|}} \exp\left(\frac{-y}{\Omega_{|\Psi_{1,2}|}}\right),$$
 (3.12)

where, $\Omega_{|\Psi_{1,2}|} = K(c_1 A_2)^2$. Similar to (3.11) and (3.12), the CDF and PDF of $|\Psi_{2,1}|^2 = \left(A_1 |\sum_{k=1}^K h_{R_k U_1} c_2 e^{-j\phi_{U_2}^k} h_{SR_k}|\right)^2$ can be obtained suitably by interchanging the subscripts of $|\Psi_{1,2}|$ to $|\Psi_{2,1}|$ in (3.11) and (3.12) respectively.

3.3 Performance Evaluation

This section analyzes the performance of systems by computing the OP for U_1 and U_2 and the system throughput.

3.3.1 Calculation of OP at U_2

The OP is defined as the probability of instantaneous SINR falling below a specified threshold SINR. The OP at U_2 is defined as

$$P_{o2} = Pr(\gamma_2 < \gamma_{th_2}),$$

= $Pr(|\Psi_{2,2} + \Psi_{1,2}|^2 < \Xi_2).$ (3.13)

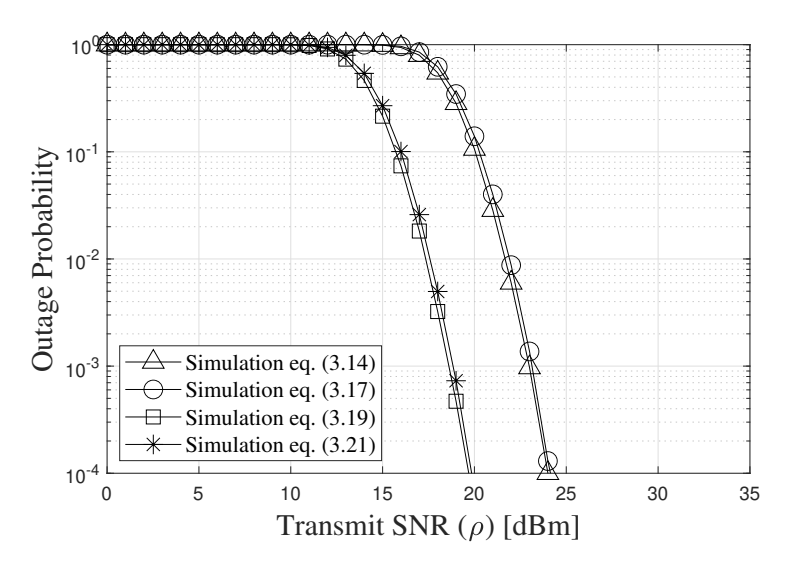


Figure 3.2: Outage Probability vs. Transmit SNR for K=24.

where, $\Xi_2 = \frac{\gamma_{th_2}}{\rho(\alpha_2 - \gamma_{th_2}\alpha_1)}$ and $\gamma_{th_2} = 2^{r_2} - 1$ is the threshold SINR, and r_2 is the target rate of U_2 for detecting the signal x_2 . By using the approximation³ $|Z_1 + Z_2|^2 \approx |Z_1|^2 + |Z_2|^2$, we can write (3.13) as

$$P_{o,2} \approx Pr(|\Psi_{2,2}|^2 + |\Psi_{1,2}|^2 < \Xi_2),$$
 (3.14)

By using (3.9), (3.10), (3.11) and (3.12), we can write (3.14) as

$$P_{o,2} \approx \int_{0}^{\Xi_{2}} \mathcal{F}_{|\Psi_{1,2}|^{2}} (\Xi_{2} - y) f_{|\Psi_{2,2}|^{2}}(y) dy,$$

$$\approx \mathcal{F}_{|\Psi_{2,2}|^{2}} (\Xi_{2}) - \int_{0}^{\Xi_{2}} \exp\left(-\frac{\Xi_{2} - y}{\Omega_{|\Psi_{1,2}|}}\right) f_{|\Psi_{2,2}|^{2}}(y) dy.$$
(3.15)

Since $f_{|\Psi_{2,2}|^2}(y)$ contains the terms \sqrt{y} , therefore it is quite challenging to solve (3.15) directly. So, we use GCQ method to evaluate OP as

$$P_{o,2} \approx \mathcal{F}_{|\Psi_{2,2}|^2}(\Xi_2) - \sum_{l=1}^{L} \frac{\Xi_2 \pi \sqrt{1 - \zeta^2}}{2L} \exp\left(-\frac{\Xi_2 - \mu}{\Omega_{|\Psi_{1,2}|}}\right) f_{|\Psi_{2,2}|^2}(\mu), \tag{3.16}$$

where, $\zeta = \cos\left(\frac{(2l-1)}{2L}\pi\right)$, $\mu = \frac{\Xi_2}{2} (\zeta + 1)$ and L is the complexity accuracy trade-off factor. Note that (3.16) is valid under the condition $\alpha_2 - \gamma_{th_2}\alpha_1 > 0$, otherwise $P_{o,2} = 1$. It is noted that the term $|\Psi_{1,2}|$ negligibly contributes to γ_2 due to the incomplete cancellation of channel phases. Effectively, these terms account for random phase corrections at the RIS. Because of the random phase shifting, the contributions of $|\Psi_{1,2}|$ is less than 10% for

³The approximation is reasonably valid for $Z_1 >> Z_2$ or $Z_2 >> Z_1$. In the proposed system model $\Psi_{2,2} >> \Psi_{1,2}$ as observed from Figure 3.2, because $\Psi_{2,2}$ accounts for the coherent phase shift part at U_2 , and $\Psi_{1,2}$ accounts for random phase shift part at U_2 .

 $K \ge 16$ in the sums $|\Psi_{1,2} + \Psi_{2,2}|$. This contribution reduces to 2.5% for K = 64. Further, the impact of terms $|\Psi_{1,2}|$ for K = 24 on OP performance is found to be negligible, as shown in Figure 3.2. Thus, the expression (3.14) can be approximately written as

$$\tilde{P}_{o,2} \approx Pr\left(|\Psi_{2,2}|^2 < \Xi_2\right) \approx \mathcal{F}_{|\Psi_{2,2}|^2}(\Xi_2)$$
 (3.17)

3.3.2 Calculation of OP at U_1

The OP at U_1 is defined as the event when U_1 is not able to decode x_2 of U_2 and secondly, if U_1 decodes x_2 , while it is unable to decode its own signal x_1 successfully. Mathematically, it is defined as

$$P_{o,1} = Pr(\gamma_{12} < \gamma_{th_2}) + Pr(\gamma_{12} > \gamma_{th_2}, \gamma_1 < \gamma_{th_1}),$$

= $Pr(|\Psi_{1,1} + \Psi_{2,1}|^2 < \Xi_1).$ (3.18)

where, $\Xi_1 = \frac{\gamma_{th_1}}{\rho\alpha_1}$, $\gamma_{th_1} = 2^{r_1} - 1$ is the threshold SNR, and r_1 is the target rate of U_1 for detecting the signal x_1 . By using the approximation $|Z_1 + Z_2|^2 \approx |Z_1|^2 + |Z_2|^2$, we can write (3.18) as

$$P_{o,1} \approx Pr\left(|\Psi_{1,1}|^2 + |\Psi_{2,1}|^2 < \Xi_1\right)$$
 (3.19)

Similarly, by using (3.15) and applying GCQ method, we can write (3.19) as

$$P_{o,1} \approx \mathcal{F}_{|\Psi_{1,1}|^2}(\Xi_1) - \sum_{l=1}^{L} \frac{\Xi_1 \pi \sqrt{1 - \zeta^2}}{2L} \exp\left(-\frac{\Xi_1 - \mu}{\Omega_{|\Psi_{2,1}|}}\right) \times f_{|\Psi_{1,1}|^2}(\mu)$$
(3.20)

where, $\zeta = \cos\left(\frac{(2l-1)}{2L}\pi\right)$, $\mu = \frac{\Xi_1}{2}\left(\zeta + 1\right)$ and L is the complexity accuracy trade-off factor. Here, the impact of $\Psi_{2,1}$ is negligible on U_1 because of random phase shifting as shown in Figure 3.2 and approximated OP can be represented as

$$\tilde{P}_{o,1} \approx P(|\Psi_{1,1}|^2 < \Xi_1) \approx \mathcal{F}_{|\Psi_{1,1}|^2}(\Xi_1)$$
 (3.21)

3.3.3 System Throughput

System throughput is generally defined as the actual amount of data successfully transmitted over a communication link. In our proposed system, we have considered a delay-limited transmission mode that uses OP at a constant transmission rate to evaluate the system throughput [78]. Therefore, mathematically, the system throughput for the

considered RIS-NOMA system is modeled as

$$\mathcal{T} = r_1 (1 - P_{o,1}) + r_2 (1 - P_{o,2}) \tag{3.22}$$

3.4 Simulation Results and Discussion

In this section, we summarize the results of the OP and system throughput of the considered system through Monte Carlo simulations and analytical expressions. The thermal noise power (in dBm) is assumed as $\sigma_i^2 = -174 + 10 \log_{10}(BW) + NF$, where BW is the bandwidth. All other parameter values considered for performing simulations have been specified in Table 3.1.

Table 3.1: Simulation Parameters for RIS-NOMA.

Parameter	Values
Scenario-(a): (1) Distance from $S - R$, d_{SR_1} , (2)	(1) 10 m, (2)
Distance from $R - U_1$, d_{RU_1} and (3) Distance from	14.14 m and (3)
$R-U_2, d_{RU_2}$	22.36 m
Scenario-(b): (1) Distance from $S - R1$, d_{SR1} , (2)	(1) 11.18m, (2)
Distance from $R1 - U_1$, d_{R1U_1} , (3) Distance from	11.18m (3) 14.14
$S-R2$, d_{SR2} (4) Distance from $R2-U_1$, d_{R2U_1} and	m and (4) 14.14 m
Distance from $R1 - U_2$, d_{R1U_2}	
Scenario-(c) (proposed): (1) Distance from $S-R$, d_{SR} ,	(1) 10 m, (2)
(2) Distance from $R-U_1$, d_{RU_1} and (3) Distance from	14.14 m and (3)
$R-U_2, d_{RU_2}$	22.36 m
Operating frequency	3 GHz
Bandwidth (BW)	10 MHz
G_X and G_Y	10 dBi
Noise figure (NF)	10
Number of RIS elements (K)	24
α_1 and α_2	0.3 and 0.7
r_1 and r_2	0.5
Complexity accuracy trade-off factor (L)	50

In Figure 3.3, the effectiveness of the proposed RIS-NOMA network scenario, i.e., scenario-(c) is compared with scenario-(a) [110] and scenario-(b) [81] in terms of OP against the transmit SNR. For scenario-(a): We have considered one RIS sheet with K elements placed at the halfway distance between two users to serve both users. We have taken half of the RIS elements to serve one user dedicatedly and used the remaining half to serve the other. For this, we have considered two-dimensional coordinates to describe each node position: U_1 and U_2 are located at (0,0) and (30,0) respectively, RIS (R) is located at (10,10) and source (S) is located at (10,0) For scenario-(b): We have considered an RIS sheet with K/2 elements to serve each user and place it near the target user, where RIS-1

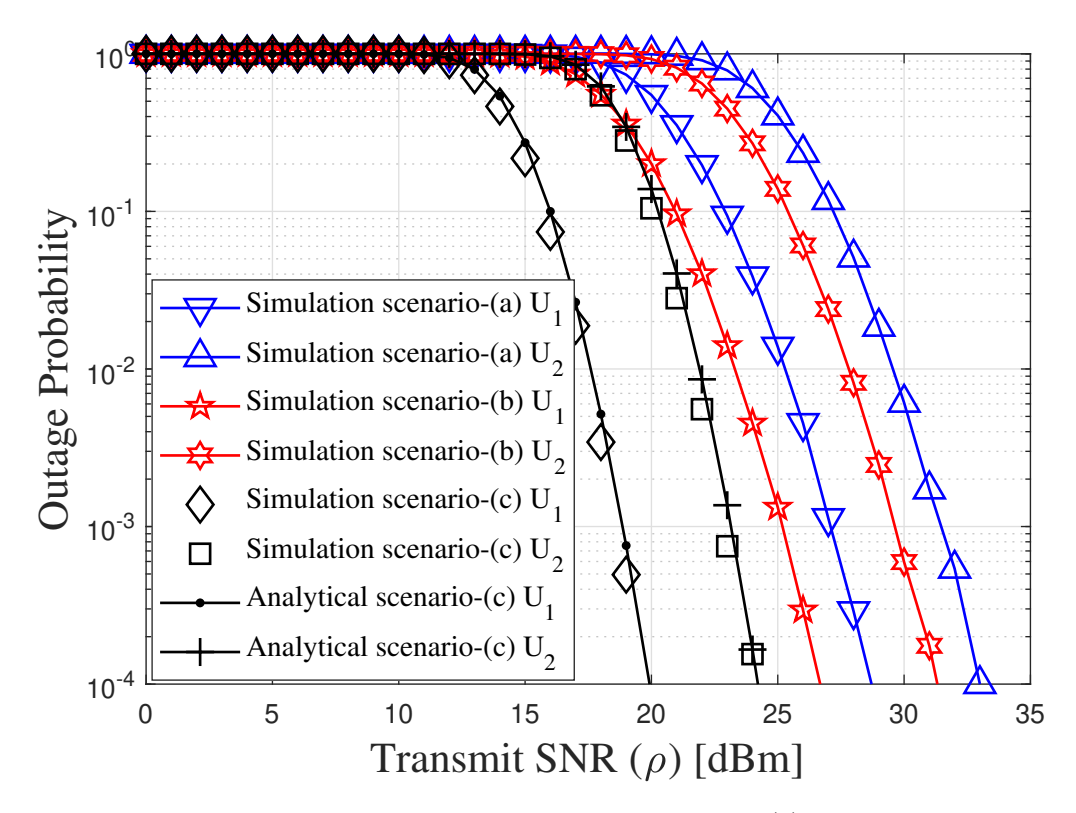


Figure 3.3: Comparison of outage probability of scenario-(c) vs. transmit SNR with scenario-(a) and scenario-(b).

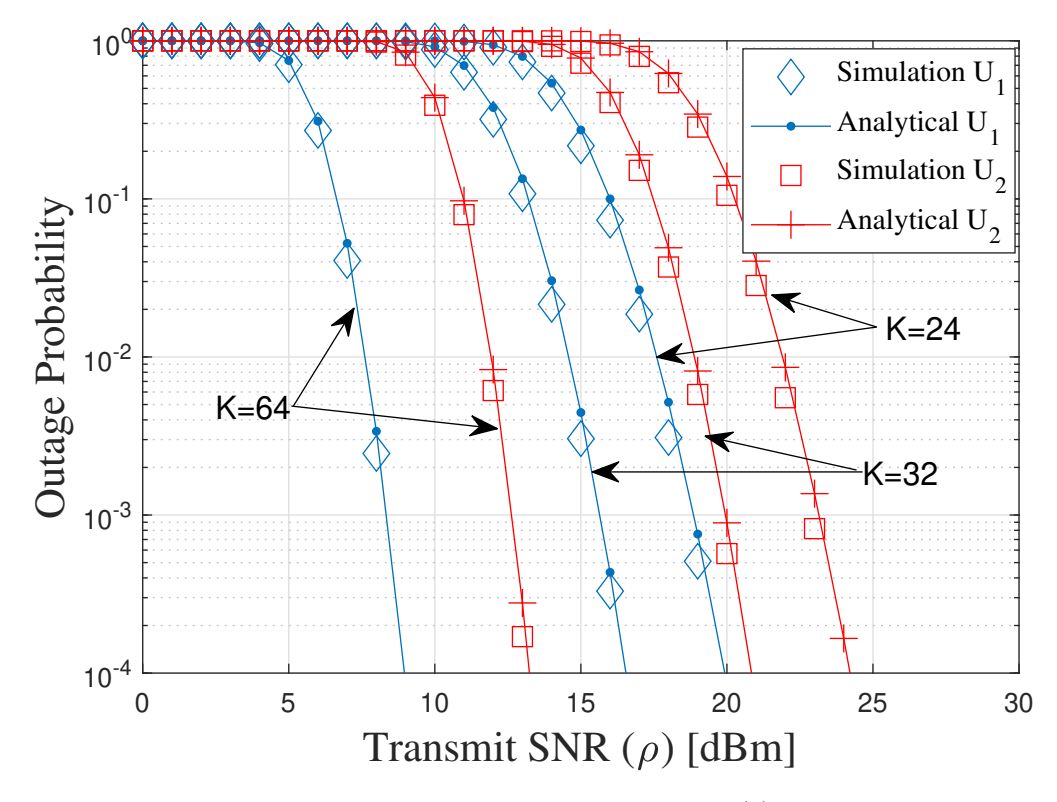


Figure 3.4: Comparison of outage probability of scenario-(c) with different values of K.

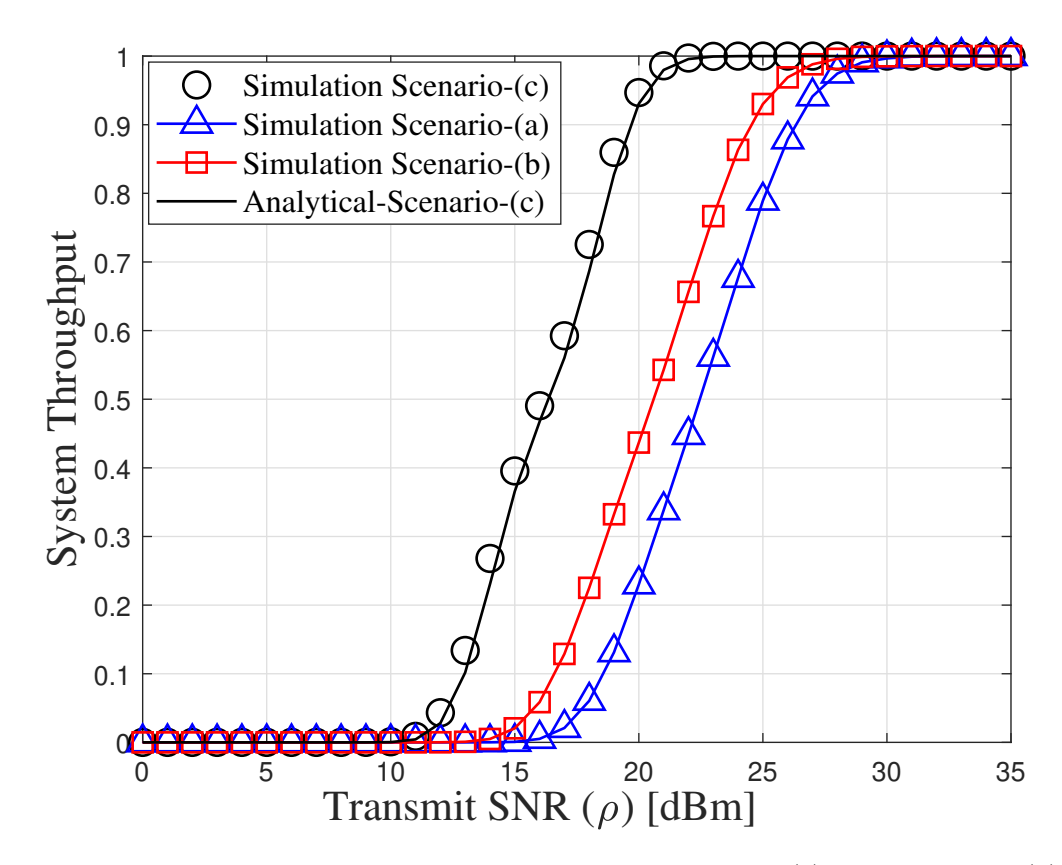


Figure 3.5: Comparison of system throughput for scenario-(c) with scenario-(a) and scenario-(b) vs. transmit SNR.

(R1) is used to serve U_1 and RIS-2 (R2) is used to serve U_2 . Two-dimensional coordinates used for each node position are set as U_1 and U_2 located at (0,0) and (30,0) respectively, R1 and R2 are located at (5,10) and (30,10), whereas the source (S) is located at (15,0). The node positions for scenario-c are the same as that of scenario-a, and the rest of all other parameters for scenarios-(a), (b), and (c) are specified in Table 3.1. It is clear from Figure 3.3 that the proposed scenario-(c) performs better than scenarios-(a) and (b). This is because in scenarios-(a) and (b), the number of reflecting elements to serve U_1 and U_2 reduces to half as compared to the scenario-(c).

Figure 3.4 verifies the Monte-Carlo simulation's correctness and theoretical expression of our proposed scenario in terms of OP for different values of K = 24, 32, and 64. The system performance improves as the number of reflecting elements (K) increases. The results show that the slope of OP versus transmit SNR curves for U_1 and U_2 are the same. Thus, the proposed design can simultaneously serve both the NOMA users, with a single RIS achieving the same diversity order for both users. Further, the OP performance of the user nearer to the RIS is better as we consider that none of the users can receive a direct signal from S, i.e., the base station. Figure 3.5 plots the system throughput versus the

transmit SNR for K = 24. The system throughput curves for the proposed RIS-NOMA network are plotted according to the (3.22). We can observe from the figure that the system throughput for scenario-(c) is superior to scenario-(a) and scenario-(b). This is because, in delay-limited transmission mode, system throughput is affected by the OP.

3.5 Summary

In this chapter, we investigated the performance of a new design of the RIS-NOMA system which provides a coherent phase shift to both users in the NOMA pair by utilizing all the elements of an RIS simultaneously. Firstly, we have designed the phase shifts for RIS elements to simultaneously assist both users in the NOMA pair through coherent phases. Secondly, the closed-form expression in terms of OP is derived by applying the GCQ and moment-matching method. System throughput is also evaluated from the obtained OP in a delay-limited transmission mode. Finally, Monte-Carlo simulations verify the accuracy of the closed-form expressions of OP and system throughput. Numerical results also confirm the superiority of the proposed design of the RIS-NOMA system with other existing scenarios of RIS-NOMA systems.

Chapter 4

Wireless Powered RIS-assisted Cognitive NOMA Network with Hardware Impairments: IBL and FBL Analysis

The literature reported on RIS-NOMA [74, 75, 76, 77, 78, 80], RIS-CR [63, 64, 65, 66, 67] and RIS-CR-NOMA [83, 84, 85, 86, 87] focused mainly on the IBL transmission. In contrast, the FBL transmission aspect of RIS-assisted communication has been studied in [95, 96, 97, 98]. There are four notable limitations identified in the current literature on RIS-CR-NOMA networks for FBL transmission. Firstly, most of the existing works on RIS-CR-NOMA [83, 84, 85, 86, 87] are limited to the performance analysis of IBL transmission. This opens up the opportunity to analyze the FBL transmission for RIS-CR-NOMA networks, which is required for the critical URLLC feature of the 6G use case. Secondly, the promising aspect of deploying an IoT system, i.e., Energy Harvesting (EH), is not yet explored in the RIS-CR-NOMA system. The two RF energy harvesting models, namely wireless power communication network [111, 112] and simultaneously wireless information and power transfer [113, 114, 115], have been less considered for RIS-CR-NOMA networks, despite being studied in CR and NOMA scenarios separately. Thirdly, existing works [83, 84, 85, 86, 87] have considered Primary User (PU) with a single antenna, whereas, in this chapter, we considered multiple antennas at the PU. Fourthly, in practical scenarios, HI is inevitable in IoT hardware due to its low cost, and the literature also lacks an analysis of RIS-CR-NOMA with HI at the transceiver nodes.

In this chapter, we present a downlink wireless-powered RIS-assisted CR-NOMA IoT network in which a secondary source harvests RF energy from a multiantenna power beacon to transmit information to the SUs in an underlay CR mode. While exploring

practical applications, we also assessed the impact of HIs on the transceiver nodes of the users and the secondary source. The performance of the proposed system is analyzed using IBL and FBL analysis. For the IBL analysis, we derived the analytical expressions for the OP and system throughput for the SUs for the pSIC and ipSIC cases. We have used the GCQ and the Gauss Laguerre Quadrature (GLQ) method to evaluate the same. Asymptotic analysis is done at higher transmit power to gain useful insights and is mentioned in **Remark 4.1**. For the FBL analysis, we derived the analytical expression of ABLER and goodput with the help of the GCQ and the GLQ method. We have also deduced the expressions for latency and reliability from the ABLER expressions. Asymptotic analysis of ABLER is also done at a higher transmit power regime, and the insights are mentioned in **Remark 4.2**. Finally, Monte Carlo simulations are done to verify the analytical results. Numerical results verified the enhanced performance of the wireless-powered RIS-assisted CR-NOMA network over OMA in IBL and FBL. Furthermore, the system performance is also analyzed with other parameters such as HIs, ipSIC, number of antennas at PU, number of antennas at power beacon, number of RIS elements, time splitting factor, blocklength, and number of information bits.

4.1 System Model

4.1.1 System Description

We considered a wireless-powered RIS-assisted CR-NOMA system as shown in Figure 4.1. The Primary Network (PN) and SN utilize the same spectrum, and SN operates in underlay mode. The PN consists of a PU (D), with L antennas to receive the signal from its legacy transmitter. The SN consists of a secondary source (S), RIS (R), and two SUs (IoT users), the near user, U_1 , and a far user, U_2 . Here, S communicates with U_1 through a direct link and U_2 with the assistance of RIS¹, R. The RIS, R, consists of K passive elements. It is assumed that S is an energy-limited device that harvests its energy from the RF signal coming from a power beacon (B) with N antenna under CR constraint. We have also assumed: (i) all the nodes of SN, i.e., S, U_1 , and U_2 , are equipped with a single antenna and operate in half duplex mode, (ii) the RIS components do not exhibit joint processing or signal coupling, and the distance separating the elements is more than half a wavelength, (iii) there is no direct link between the primary source and the SUs,

¹It is assumed that R is located far away from B. Therefore, there is a negligible amount of signal coming from B and reflected toward U_2 . Additionally, R is tuned to provide coherent phase shifts, from S to R and from R to U_2 ; thus, the signals coming from B to R undergo random phase shits and can be ignored altogether.

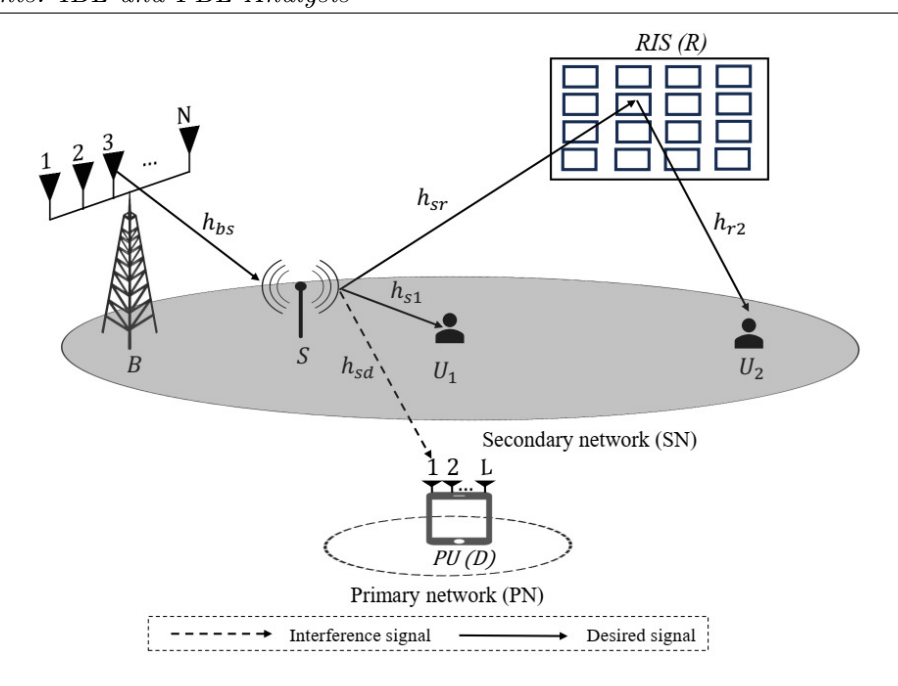


Figure 4.1: Wireless powered downlink RIS-assisted cognitive NOMA network.

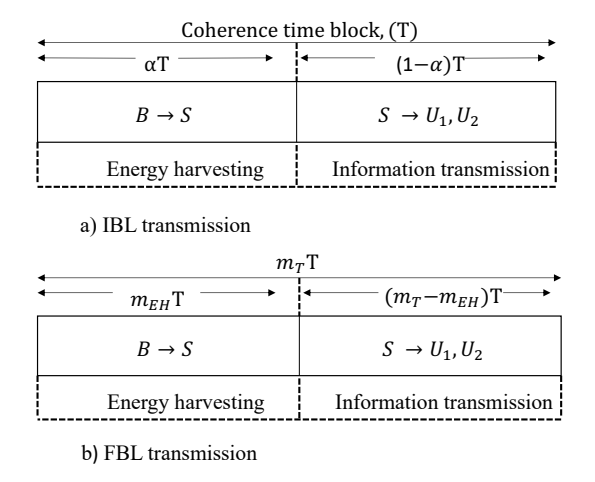


Figure 4.2: Timing diagram for a) IBL transmission, b) FBL transmission.

and (iv) the perfect knowledge of CSI available at each receiver node. The considered system model operates in a TDMA with two consecutive phases encompassing EH and Information Transmission (IT), as shown in Figure 4.2. In the first phase, i.e., EH, S harvests the energy from the RF signal² of B. In the IT phase, S uses its harvested energy to transmit the information signal to U_1 and U_2 through NOMA transmission.

 $^{^{2}}$ We have used the linear EH model for analytical tractability. It is assumed the S has a supercapacitor and the whole harvested energy is greater than the activation threshold and used to employ data transmission [112, 115].

4.1.2 Channel Model

We denote the channel and distance between any two nodes X and Y in the considered system as h_{XY} and d_{XY} , respectively. The reflection matrix of R is defined as $\mathbf{\Theta} = diag(e^{j\theta_1}, e^{j\theta_2}, \dots, e^{j\theta_K}) \in \mathbb{C}^{K \times K}$, where $\theta_k \in [0, 2\pi)$ indicates the k^{th} reflecting element phase shift. We assume the channel vector from B to S, $\mathbf{h}_{bs} = [h_{bs}^1, h_{bs}^2 \cdots h_{bs}^N]$, the channel from S to U_1 , h_{s1} and the channel vector from S to D, $\mathbf{h}_{sd} = [h_{sd}^1, h_{sd}^2 \cdots h_{sd}^L]$, to be Rayleigh distributed, i.e., $h_{XY} \in \mathcal{CN}(0, \Omega_{XY})$, where $X \in \{b, s\}$ and $Y \in \{s, 1, 2, d\}$. $\Omega_{XY} = (\mathcal{A}_o d_{XY}/d_o)^{-\tau}$, d_o , denotes the reference distance, τ is the path loss exponent, and \mathcal{A}_o is the average signal power attenuation at d_o . Additionally, we assume the channel between S to k^{th} element of R, h_{sk} , and the channel between k-th element of R to U_2 , h_{k2} , to be Rician distributed, i.e., $h_{XY} = \sqrt{\Omega_{XY}} \left(\sqrt{\kappa/(\kappa+1)} + \sqrt{1/(\kappa+1)} \tilde{h}_{XY} \right)$, where, $X = \{s, k\}$, $Y = \{k, 2\}$, κ is the Rician factor, $\tilde{h}_{XY} \sim \mathcal{CN}(0, 1)$. In vector form, the channel vectors from S to R and from R to U_2 can be expressed as $\mathbf{h}_{sr} = [h_{s1}, h_{s2}, \dots, h_{sK}] \in \mathbb{C}^{1 \times K}$, $\mathbf{h}_{r2} = [h_{12}, h_{22}, \dots, h_{K2}]^T \in \mathbb{C}^{K \times 1}$.

4.1.3 Energy Harvesting and Information Transmission

4.1.3.1 For Infinite Blocklength

During the EH phase, B transmits energy signals to S through N antennas over αT duration, as shown in Figure 4.2 (a). The cumulative energy harvested at S can be represented as follows

$$E_s^{EH} = \eta \alpha T P_B \sum_{n=1}^{N} \left| h_{bs}^n \right|^2, \tag{4.1}$$

where, $\eta = (0,1)$ is the energy conversion efficiency factor of S, $\alpha = (0,1)$ is the TS factor, T is the coherence time, and P_B is the transmit power of B. Therefore, the transmit power of S used for IT can be expressed as

$$P_s^{EH} = \frac{E_s^{EH}}{(1 - \alpha)T} = \Delta_{si} P_B \sum_{n=1}^{N} |h_{bs}^n|^2, \tag{4.2}$$

where, $\Delta_{si} = \frac{\eta \alpha}{(1-\alpha)}$. To satisfy the QoS of PU, the transmit power of S should be lower than the maximum interference constraint I_{th} [84, 85, 86]. Therefore, the transmit power of S can be expressed as

$$P_s = \min\left(P_s^{EH}, I_{th} / \sum_{l=1}^{L} |h_{sd}^l|^2\right).$$
 (4.3)

4.1.3.2 For Finite Blocklength

We denote m_T , and T as the number of channel uses and the duration (coherence time) of each channel use. Thus, $m_T T$ is the total transmission duration, as shown in Figure 4.2 (b). During the EH phase, B transmits its energy signals to S through N antennas over a duration of $m_{EH} T$. The cumulative energy harvested at S can be represented as follows

$$E_s^{EH} = \eta m_{EH} T P_B \sum_{n=1}^{N} |h_{bs}^n|^2, \tag{4.4}$$

 $m_{EH} = (0, m_T)$ is the number of channel uses for EH phase. Therefore, the transmit power of S used for the IT phase can be expressed as

$$P_s^{EH} = \frac{E_s^{EH}}{(m_T - m_{EH})T} = \Delta_{sf} P_B \sum_{n=1}^{N} |h_{bs}^n|^2, \tag{4.5}$$

where, $\Delta_{sf} = \frac{\eta m_{EH}}{(m_T - m_{EH})}$. By considering the maximum interference power constraint of the CR network, the transmit power of S can be expressed similarly to that in expression (4.3).

4.1.4 Signal Model

According to NOMA, during the IT phase (for IBL and FBL), S transmits the superimposed signal $x = (\sqrt{a_1}x_1 + \sqrt{a_2}x_2)$ to U_1 and U_2 . x_1 and x_2 are respectively the signals intended for U_1 and U_2 such that $\mathbb{E}\{|x_1|^2\} = 1$ and $\mathbb{E}\{|x_2|^2\} = 1$, whereas, a_1, a_2 are the PA factors for x_1 and x_2 , respectively, satisfying $a_2 > a_1$ for user fairness with $a_1 + a_2 = 1$. Therefore, the signal received at U_1 and U_2 can be expressed respectively as

$$y_1 = \sqrt{P_s} h_{s1}(x + \varepsilon_s) + \varepsilon_1 + n_1, \tag{4.6}$$

$$y_2 = \sqrt{P_s} (\mathbf{h}_{sr} \mathbf{\Theta} \mathbf{h}_{r2}) (x + \varepsilon_s) + \varepsilon_2 + n_2, \tag{4.7}$$

where P_s denotes the transmitted power of S, ε_s , ε_1 , and ε_2 indicates the distortion noise due to HIs at S, U_1 and U_2 with $\varepsilon_s \sim \mathcal{CN}(0, k_s^2 P_s)$, $\varepsilon_1 \sim \mathcal{CN}(0, k_1^2 |h_{s1}|^2 P_s)$, and $\varepsilon_2 \sim \mathcal{CN}(0, k_2^2 |\mathbf{h}_{sr} \boldsymbol{\Theta} \mathbf{h}_{r2}|^2 P_s)$ [82]. k_s , k_1 and k_2 indicate the degree of HI. The parameters k_s , k_1 and k_2 are interpreted as the Error Vector Magnitudes (EVMs). EVM is a prevalent quality assessment for RF transceivers, calculated as the ratio of the average distortion magnitude to the average signal magnitude. As EVM reflects the aggregated impact of

various HIs and compensation algorithms, it is possible to measure it directly in practical settings. n_1 and n_2 are the AWGN generated at U_1 and U_2 with $n_1 \sim \mathcal{CN}(0, \sigma_1^2)$ and $n_2 \sim \mathcal{CN}(0, \sigma_2^2)$. According to the NOMA principle, U_1 must decode x_2 first and then subtract it from y_1 before decoding x_1 . Such a decoding process for x_1 is known as SIC. Therefore, the Signal to Interference plus Distortion and Noise (SIDNR) at U_1 for decoding x_2 and x_1 can be respectively written as

$$\Upsilon_{1\to 2} = \frac{P_s a_2 |h_{s1}|^2}{P_s |h_{s1}|^2 \chi_2 + \sigma_1^2},\tag{4.8}$$

and

$$\Upsilon_1 = \frac{P_s a_1 |h_{s1}|^2}{P_s |h_{s1}|^2 \chi_1 + \sigma_1^2},\tag{4.9}$$

where, $\chi = a_1 + k_s^2 + k_1^2$, $\chi_1 = \psi a_2 + k_s^2 + k_1^2$ and ψ is the ipSIC factor, $\psi = 0$ is the case of pSIC and $0 < \psi < 1$ refers to ipSIC. At U_2 , x_2 is decoded directly by considering x_1 as noise. Thus, the received SIDNR for decoding x_2 at U_2 is given as

$$\Upsilon_2 = \frac{P_s a_2 |\mathbf{h}_{sr} \mathbf{\Theta} \mathbf{h}_{r2}|^2}{P_s |\mathbf{h}_{sr} \mathbf{\Theta} \mathbf{h}_{r2}|^2 \chi_2 + \sigma_2^2},\tag{4.10}$$

where, $\chi_2 = a_1 + k_s^2 + k_2^2$.

For comparison with the benchmark scheme, we use TDMA as an OMA scheme, in which the whole IT phase is carried out in two consecutive time slots, and each user is serviced in two consecutive slots. Accordingly, the instantaneous SIDNR for decoding signal x_i at $U_i, i \in \{1, 2\}$ is

$$\Upsilon_i^{OMA} = \frac{P_s^{OMA} |\mathcal{H}_i|^2}{P_s^{OMA} \chi_{oi} + \sigma_i^2},\tag{4.11}$$

where, $\mathcal{H}_{i} = h_{s1}$ for i = 1 and $\mathcal{H}_{i} = \mathbf{h}_{sr}\boldsymbol{\Theta}\mathbf{h}_{r2}$ for i = 2. $\chi_{oi} = k_{s}^{2} + k_{1}^{2}$ for i = 1, $\chi_{oi} = k_{s}^{2} + k_{2}^{2}$ for i = 2 and $P_{s}^{OMA} = min\left(2P_{s}^{EH}, I_{th}/\sum_{l=1}^{L} |h_{sd}^{l}|^{2}\right)$.

4.2 Channel Statistics

Let $|h_{bs}^{\sum}|^2 = \sum_{n=1}^N |h_{bs}^n|^2$ be the the total channel coefficient from B to S. Note that $|h_{bs}^{\sum}|^2$ is the sum of N independent exponential random variables and its distribution is chi-square. Therefore the PDF of $|h_{bs}^{\sum}|^2$ can be expressed as

$$f_{\left|h_{bs}^{\Sigma}\right|^{2}}(x) = \frac{x^{N-1}}{\Omega_{BS}^{N}\Gamma(N)} \exp\left(-\frac{x}{\Omega_{BS}}\right),\tag{4.12}$$

Similar to (4.12), the PDF of $|h_{sd}^{\Sigma}|^2 = \sum_{l=1}^{L} |h_{sd}^{l}|^2$ can be obtained. h_{s1} is Rayleigh distributed, therefore $|h_{s1}|^2$ is exponentially distributed with PDF, $f_{|h_{s1}|^2}(x) = \exp(-x/\Omega_{s1})/\Omega_{s1}$. For notational simplicity, the cascaded Rician channel is represented as $\mathcal{X} = \left|\sum_{k=1}^{K} h_{sk} e^{j\theta_k} h_{k2}\right|^2$. By using coherent phase shift design [17],[76],[19], to facilitate constructive reception at U_2 , the phase shift of the k^{th} element of R is set as $\theta_k = -arg(h_{sk}) - arg(h_{k2})$. Thus, we can write $\mathcal{X} = \left(\sum_{k=1}^{K} |h_{sk}h_{k2}|\right)^2$. Let $X_k = |h_{sk}h_{k2}|$. The PDF of cascaded Rician fading channel X_k can be expressed as [116]

$$f_{X_k}(x) = \frac{1}{\sqrt{\Omega_{sk}\Omega_{k2}}} \sum_{i=0}^{\infty} \sum_{j=0}^{\infty} \frac{4x^{i+j+1}(\kappa+1)^{i+j+2}\kappa^{i+j}}{(i!)^2(j!)^2 e^{2\kappa}} \times (\Omega_{sk}\Omega_{k2})^{-\frac{i+j+1}{2}} K_{i-j} \left[\frac{2x(\kappa+1)}{\sqrt{\Omega_{sk}\Omega_{k2}}} \right],$$
(4.13)

where $K_v(\cdot)$ is the modified Bessel function of the second kind with order v [117, Eq. (8.432)]. The mean and variance of X_k can be written as

$$\mathbb{E}[X_k] = \frac{\pi \sqrt{\Omega_{sk}\Omega_{k2}}}{4(\kappa+1)} \left[L_{\frac{1}{2}}(-\kappa) \right]^2, \tag{4.14}$$

and

$$Var(X_k) = \Omega_{sk}\Omega_{k2} \left[1 - \frac{\pi^2}{16(1+\kappa)^2} \left[L_{\frac{1}{2}}(-\kappa) \right]^4 \right], \tag{4.15}$$

where, $L_{\frac{1}{2}}(\kappa) = e^{\frac{1}{2}}[(1-\kappa)I_0(-\frac{\kappa}{2}) - \kappa I_1(-\frac{\kappa}{2})]$ is the Laguerre polynomial. Here $I_v(\cdot)$ is the modified Bessel function of the first kind with order v. Also, by using the Laguerre series polynomial approximation [118, Eq. (2.76)], which is a moment-matching approach, we can obtain the approximate PDF and CDF of \mathcal{X} as

$$f_{\mathcal{X}}(x) \approx \frac{x^{\varphi_k} e^{-\frac{x}{\phi_k}}}{\phi_k^{\varphi_k+1} \Gamma(\varphi_i+1)}, \quad \mathcal{F}_{\mathcal{X}}(x) \approx \frac{\gamma\left(\varphi_k+1, \frac{\sqrt{x}}{\phi_k}\right)}{\Gamma(\varphi_k+1)}.$$
 (4.16)

where, $\varphi_k = \frac{K\mathbb{E}^2[X_k] - Var(X_k)}{Var(X_k)}$ and $\phi_k = \frac{Var(X_k)}{\mathbb{E}[X_k]}$. $\gamma(\cdot, \cdot)$ and $\Gamma(\cdot)$ represent the lower incomplete Gamma and Gamma function, respectively.

4.3 Infinite Blocklength Analysis

In this section, we derive the analytical and asymptotic expression for the OP and system throughput for the IBL transmission regime. We assume $\sigma_1^2 = \sigma_2^2 = \sigma^2$. An outage event is characterized by a situation in which the SIDNR/SNR at a receiver is less than a predetermined threshold. Let $\gamma_{th_i} = 2^{[r_i/(1-\alpha)]} - 1$ be the given threshold at U_i , $i \in \{1, 2\}$,

where r_i is the target rate for decoding x_i at U_i . Therefore, the OP at U_1 and U_2 can be expressed mathematically as

$$P_1^{out} = \Pr\left(\Upsilon_{1\to 2} > \gamma_{th_2}, \Upsilon_1 < \gamma_{th_1}\right) + \Pr\left(\Upsilon_{1\to 2} < \gamma_{th_2}\right),\tag{4.17}$$

$$P_2^{out} = \Pr\left(\Upsilon_2 < \gamma_{th_2}\right). \tag{4.18}$$

4.3.1 Calculation of OP at U_1

The closed-form analytical expression for the OP of U_1 can be obtained by using the steps mentioned in Appendix A.3 and can be expressed as

$$P_{1}^{out} = \left[1 - \exp\left(-\frac{\rho_{th}}{\rho\Omega_{sd}}\right)\right] \left[\sum_{u=1}^{U} H_{u} \frac{(x_{u})^{N-1}}{\Gamma(N)} \left(1 - \exp\left(-\frac{\delta_{1}}{\Omega_{bs} x_{u} \rho \Delta_{si} \Omega_{s1}}\right)\right)\right] + \left[\sum_{u=1}^{U} H_{u} \frac{(x_{u})^{L-1}}{\Gamma(L)} \exp\left(-\frac{\rho_{th}}{\rho\Omega_{sd}}\right) \left(1 - \exp\left(-\frac{\delta_{1}}{(\Omega_{s1}\rho_{th})} \left(x_{u}\Omega_{sd} + \frac{\rho_{th}}{\rho}\right)\right)\right],$$

$$(4.19)$$

where, $\rho = \frac{P_B}{\sigma^2}$ is the transmit SNR, $\rho_{th} = \frac{I_{th}}{\sigma^2}$ is the interference constraint SNR, $\delta_1 = \max\left(\frac{\gamma_{th_2}}{a_2 - \chi_2 \gamma_{th_2}}, \frac{\gamma_{th_1}}{a_1 - \chi_1 \gamma_{th_1}}\right)$, x_u is the u-th zero point (abscissa) of Laguerre polynomial, $L_U(x) = \frac{e^x}{U!} \frac{d}{dx^P} \left(x^U e^{-x}\right)$, u-th weight can be expressed as $H_u = \frac{\left(P!\right)^2 x_p}{\left[L_{U+1}(x_u)\right]^2}$ and U is the Laguerre tradeoff factor. (4.19) is valid only when $a_2 - \chi_2 \gamma_{th_2} > 0$ or $a_1 - \chi_1 \gamma_{th_1} > 0$, otherwise there exist an upper bound characterized by $P_1^{out} = 1$. The OP of U_1 is a function of parameters like PA factor (a_1) , RIS elements (K), number of antennas at B, (N), the number of antennas at the PU, (L) and the factor χ_1 . Additionally, as the ipSIC factor, (ψ) increases, results in smaller $a_1 - \chi_1 \gamma_{th_1}$, and it will increase the P_1^{out} .

4.3.2 Calculation of OP at U_2

By using the steps mentioned in Appendix A.4, the closed-form analytical expression for the OP of U_2 can be expressed as

$$P_{2}^{out} = \left[1 - \exp\left(-\frac{\rho_{th}}{\rho\Omega_{sd}}\right)\right] \left[\sum_{u=1}^{U} H_{u} \frac{(x_{u})^{N-1}}{\Gamma(N)} \frac{1}{\Gamma(\varphi_{k}+1)} \gamma\left(\varphi_{k}+1, \frac{\sqrt{\delta_{2}/\Delta_{si}\rho x_{u}}}{\phi_{k}}\right)\right] + \left[\sum_{u=1}^{U} H_{u} \frac{(x_{u})^{L-1}}{\Gamma(L)} \exp\left(-\frac{\rho_{th}}{\rho\Omega_{sd}}\right) \frac{1}{\Gamma(\varphi_{k}+1)} \gamma\left(\varphi_{k}+1, \frac{\sqrt{\frac{\delta_{2}}{\rho_{th}}}(x_{u}\Omega_{sd}+\frac{\rho_{th}}{\rho})}{\phi_{k}}\right)\right], \tag{4.20}$$

where, $\delta_2 = \frac{\gamma_{th_2}}{a_2 - \chi_2 \gamma_{th_2}}$. (4.20) holds only for $a_2 - \chi_2 \gamma_{th_2} > 0$, otherwise, $P_2^{out} = 1$.

4.3.3 Asymptotic OP analysis

The asymptotic analysis of OP for U_1 and U_2 can be obtained by setting the transmit power, $P_s \to \infty$. Mathematically, the asymptotic OP can be represented as

$$P_{\infty}^{out}(P_s) = G\left(\frac{1}{P_s}\right)^{Do},\tag{4.21}$$

where G is the coding gain and Do is the diversity order. The diversity order can be described as the rate at which OP decreases as P_s increases. The asymptotic OP for U_1 and U_2 can be obtained for two scenarios; 1) when, $\rho \ge \frac{\rho_{th}}{|h_{sd}^{\Sigma}|^2}$ and 2) $\rho \le \frac{\rho_{th}}{|h_{sd}^{\Sigma}|^2}$.

4.3.3.1 Asymptotic OP at U_1

The asymptotic OP for U_1 can be obtained as

$$P_{1,\infty}^{out} = \begin{cases} \sum_{u=1}^{U} Y \left[1 - \exp\left(-\frac{\delta_1/\Omega_{bs} x_u \rho \Delta_{si}}{\Omega_{s1}}\right) \right], & \rho \le \frac{\rho_{th}}{|h_{sd}^{\Sigma}|^2} \\ \sum_{u=1}^{U} Z \left[1 - \exp\left(-\frac{\delta_1(x_u \Omega_{sd})}{\Omega_{s1} \rho_{th}}\right) \right], & \rho \ge \frac{\rho_{th}}{|h_{sd}^{\Sigma}|^2} \end{cases}$$
(4.22)

where, $Y = H_u \frac{(x_u)^{N-1}}{\Gamma(N)}, Z = H_u \frac{(x_u)^{L-1}}{\Gamma(L)}.$

4.3.3.2 Asymptotic OP at U_2

The asymptotic OP for U_2 can obtained as

$$P_{2,\infty}^{out} = \begin{cases} \sum_{u=1}^{U} Y \left[\frac{\left(\frac{\delta_2/\Delta_{si}\rho x_u}{\phi_k^2}\right)^{\frac{\varphi_k+1}{2}}}{(\varphi_k+1)\Gamma(\varphi_k+1)} \right], & \rho \leq \frac{\rho_{th}}{|h_{sd}^{\Sigma}|^2} \\ \sum_{u=1}^{U} Z \left[\frac{\left(\frac{\delta_2}{\rho_{th}} \left(x_u \Omega_{sd}\right)}{\phi_k^2}\right)^{\frac{\varphi_k+1}{2}}}{(\varphi_k+1)\Gamma(\varphi_k+1)} \right], & \rho \geq \frac{\rho_{th}}{|h_{sd}^{\Sigma}|^2} \end{cases}$$

$$(4.23)$$

Remark 4.1 It can be observed from (4.22) and (4.23) that for $\rho \leq \frac{\rho_{th}}{|h_{sd}^{\Sigma}|^2}$, the asymptotic OP for U_1 and U_2 does not depend on the parameter of interference channels, such as Ω_{sd} , L and ρ_{th} . This is because the transmit SNR (ρ) limits the interference constraint SNR (ρ_{th}). Conversely, when $\rho > \frac{\rho_{th}}{|h_{sd}^{\Sigma}|^2}$, the asymptotic OP for U_1 and U_2 does not depend upon the parameter ρ and N. This is because the interference constraint SNR (ρ_{th}) limits the transmit SNR (ρ). Additionally, the diversity order for U_1 for $\rho \leq \frac{\rho_{th}}{|h_{sd}^{\Sigma}|^2}$ is 1 and for $\rho > \frac{\rho_{th}}{|h_{sd}^{\Sigma}|^2}$, the diversity reaches an outage floor with diversity order zero. Similarly for

 U_2 , in the case of $\rho \leq \frac{\rho_{th}}{|h_{sd}^{\Sigma}|^2}$ the diversity order is $\frac{\varphi_k+1}{2}$, while for the case of $\rho > \frac{\rho_{th}}{|h_{sd}^{\Sigma}|^2}$ the diversity order is zero.

4.3.4 System throughput

System throughput is generally defined as the actual amount of data successfully transmitted over a communication link. In our proposed system, we have considered a delay-limited transmission mode that uses OP at a constant transmission rate to evaluate the system throughput. Thus, the system throughput can be obtained as

$$\mathcal{T} = r_1(1 - P_1^{out}) + r_2(1 - P_2^{out}), \tag{4.24}$$

Since OP is bounded by the outage floor when $\rho \geq \frac{\rho_{th}}{|h_{sd}^{\sum}|^2}$, therefore the upper bound of the system throughput can be obtained as

$$\mathcal{T}_{\infty} \le r_1 (1 - P_{1,\infty}^{out}) + r_2 (1 - P_{2,\infty}^{out}).$$
 (4.25)

4.4 Finite blocklength Analysis

4.4.1 Block-Error Rate Preliminaries

Shannon's theorem, built on the assumption of IBL, is no longer valid in FBL analysis [46]. In FBL transmission, ABLER is computed to analyze the system performance [102, 103, 73]. Let $\mathbb{L} = \ell_d + \ell_t$, where $\mathbb{L} = (m_T - m_{EH})$ is the number of channel uses (for IT phase), and ℓ_d , ℓ_t are the blocklengths for data and training, respectively. Therefore for a given blocklength ℓ_d , the BLER, Ξ and SINR, Υ , the maximum achievable rate, R is given by [46]

$$R(\ell_d, \Upsilon, \Xi) = C(\Upsilon) - \sqrt{\frac{V(\Upsilon)}{\ell_d}} Q^{-1}(\Xi) + \mathcal{O}\left(\frac{\log_2 \ell_d}{\ell_d}\right), \tag{4.26}$$

where, $C(\Upsilon) = \log_2(1 + \Upsilon)$ is the Shanon capacity, $V(\Upsilon) = (1 - (1 + \Upsilon)^{-2}) (\log_2 e)^2$ denotes the channel dispersion, $Q^{-1}(.)$ denotes the inverse of Gaussian Q-function and $\mathcal{O}\left(\frac{\log_2 \ell_d}{\ell_d}\right)$ are the remaining terms which can be neglected when $\ell_d \geq 100$ [119]. In FBL transmission, BLER is computed to analyze the system performance. Let Ξ_i be the BLER, \mathbb{N}_i be the number of information bits, and ℓ_d be the block length for $U_i, i \in \{1, 2\}$. Thus, the maximum achievable rate at U_i is expressed as $R_i = \frac{\mathbb{N}_i}{\ell_d}$. Therefore, the ABLER can

be obtained by averaging Ξ_i over instantaneous SINR, Υ_i , as

$$\overline{\Xi}_i = \int_0^\infty Q\left(\frac{C(\Upsilon_i - R_i)}{\sqrt{V(\Upsilon_i)/\ell_d}}\right) f_{\Upsilon_i}(x) dx, \tag{4.27}$$

The inclusion of the Q-function makes the evaluation of BLER quite complex. Therefore, we use the linear approximation method [119] as $\epsilon(\Upsilon_i) \approx Q\left(\frac{C(\Upsilon_i - R_i)}{\sqrt{V(\Upsilon_i)/\ell_d}}\right)$, where, $\epsilon(\Upsilon_i)$ is given by

$$\epsilon(\Upsilon_i) = \begin{cases}
1, & \Upsilon_i \le \nu_i \\
0.5 - \vartheta_i(\Upsilon_i - o_i), & \nu_i \le \Upsilon_i \le \mu_i \\
0, & \Upsilon_i \ge \mu_i,
\end{cases}$$
(4.28)

where, $\vartheta_i = [2\pi(2^{2R_i} - 1)/\ell_d]^{-1/2}$, $o_i = 2^{R_i} - 1$, $\nu_i = o_i - 1/(2\vartheta_i)$ and $\mu_i = o_i + 1/(2\vartheta_i)$. Accordingly (4.28) can be written as

$$\overline{\Xi}_i \approx \int_0^\infty \epsilon(\Upsilon_i) f_{\Upsilon_i}(x) dx \stackrel{(a)}{\approx} \vartheta_i \int_{\nu_i}^{\mu_i} \mathcal{F}_{\Upsilon_i}(x) dx, \tag{4.29}$$

where $\mathcal{F}_{\Upsilon_i}(x)$ is the CDF of Υ_i and step (a) is obtained by evaluation of integral using partial integration method.

4.4.2 Calculation of ABLER at U_1

With the help of the results obtained in Appendix A.3 and using the GCQ method [120], the ABLER at U_1 for wireless-powered RIS-assisted-CR-NOMA system with pSIC and ipSIC can be obtained as

$$\Xi_{1} = \vartheta_{1} \left(\frac{\mu_{1} - \nu_{1}}{2} \right) \sum_{m=1}^{M} \frac{\pi}{M} \sqrt{1 - x_{m}^{2}} \left[\left(1 - \exp\left(-\frac{\rho_{th}}{\rho \Omega_{sd}} \right) \right) \sum_{u=1}^{U} H_{u} \frac{(x_{u})^{N-1}}{\Gamma(N)} \left\{ 1 - \exp\left(-\frac{\Lambda_{1}}{\Omega_{bs} x_{u} \rho \Delta_{sf} \Omega_{s1}} \right) \right\} + \sum_{u=1}^{U} H_{u} \frac{(x_{u})^{L-1}}{\Gamma(L)} \times \exp\left(-\frac{\rho_{th}}{\rho \Omega_{sd}} \right) \left\{ 1 - \exp\left(-\frac{\Lambda_{1}}{(\Omega_{s1} \rho_{th})} \left(x_{u} \Omega_{sd} + \frac{\rho_{th}}{\rho} \right) \right) \right\} \right].$$

$$(4.30)$$

where, $\Lambda_1 = max\left(\frac{z_1}{a_2 - \chi_2 z_1}, \frac{z_1}{a_1 - \psi \chi_1 z_1}\right)$, $x_m = cos\left(\frac{2m-1}{2M}\pi\right)$, $z_1 = \left(\frac{\mu_1 - \nu_1}{2}\right)x_m + \left(\frac{\mu_1 + \nu_1}{2}\right)$, M is the complexity trade-off factor. The ABLER, $\overline{\Xi}_1$, for pSIC, can be obtained by putting $\psi = 0$ in (4.30), whereas the ABLER for the case of ipSIC can be obtained by varying $0 < \psi < 1$. It should be noted that (4.30) is valid for $a_2 - \chi_2 z_1 > 0$ and $a_1 - \psi \chi_1 z_1 > 0$, otherwise $\overline{\Xi}_1 = 1$.

4.4.3 Calculation of ABLER at U_2

With the help of the results obtained in Appendix A.4 and using the GCQ method [120], the ABLER at U_2 for wireless-powered RIS-assisted-CR-NOMA system can be obtained as

$$\overline{\Xi}_{2} = \vartheta_{2} \left(\frac{\mu_{2} - \nu_{2}}{2} \right) \sum_{m=1}^{M} \frac{\pi}{M} \sqrt{1 - x_{m}^{2}} \left[1 - \exp\left(-\frac{\rho_{th}}{\rho \Omega_{sd}} \right) \sum_{u=1}^{U} H_{u} \frac{(x_{u})^{N-1}}{\Gamma(N)} \frac{1}{\Gamma(\varphi_{k} + 1)} \right]$$

$$\gamma \left(\varphi_{k} + 1, \frac{\sqrt{\Lambda_{2}/\Delta_{sf}\rho x_{u}}}{\phi_{k}} \right) + \sum_{u=1}^{U} H_{u} \frac{(x_{u})^{L-1}}{\Gamma(L)} \exp\left(-\frac{\rho_{th}}{\rho \Omega_{sd}} \right) \frac{1}{\Gamma(\varphi_{k} + 1)}$$

$$\gamma \left(\varphi_{k} + 1, \frac{\sqrt{\frac{\Lambda_{2}}{\rho_{th}} \left(x_{u}\Omega_{sd} + \frac{\rho_{th}}{\rho} \right)}}{\phi_{k}} \right) \right].$$

$$\psi_{here}, \Lambda_{2} = \frac{z_{2}}{a_{2} - \chi_{2} z_{2}}, x_{m} = \cos\left(\frac{2m-1}{2M} \pi \right) \text{ and } z_{2} = \left(\frac{\mu_{2} - \nu_{2}}{2} \right) x_{m} + \left(\frac{\mu_{2} + \nu_{2}}{2} \right).$$

$$(4.31)$$

4.4.4 Asymptotic ABLER analysis

The asymptotic ABLER for U_1 and U_2 can be obtained for two scenarios; 1) when the transmit power of the B tends to infinity, i.e., $\rho \geq \frac{\rho_{th}}{|h_{sd}^{\sum}|^2}$ and 2) when the interference constraint goes to infinity, i.e., $\rho \leq \frac{\rho_{th}}{|h_{sd}^{\sum}|^2}$.

4.4.4.1 Asymptotic ABLER for U_1

The asymptotic ABLER for U_1 can be obtained as

$$\overline{\Xi}_{1,\infty}^{Out} = \begin{cases}
\sum_{u=1}^{U} \sum_{m=1}^{M} \vartheta_{1} \left(\frac{\mu_{1} - \nu_{1}}{2}\right) WY \times \\
\left[1 - \exp\left(-\frac{\Lambda_{1}/\Omega_{bs}x_{u}\rho\Delta_{sf}}{\Omega_{s1}}\right)\right], & \rho \leq \frac{\rho_{th}}{|h_{sd}^{\Sigma}|^{2}} \\
\sum_{u=1}^{U} \sum_{m=1}^{M} \vartheta_{1} \left(\frac{\mu_{1} - \nu_{1}}{2}\right) WZ \times \\
\left[1 - \exp\left(-\frac{\delta_{1}(x_{u}\Omega_{sd})}{\Omega_{s1}\rho_{th}}\right)\right], & \rho \geq \frac{\rho_{th}}{|h_{sd}^{\Sigma}|^{2}}
\end{cases} \tag{4.32}$$

4.4.4.2 Asymptotic ABLER for U_2

The asymptotic ABLER for U_2 can be obtained as

$$\overline{\Xi}_{2,\infty}^{out} = \begin{cases}
\sum_{u=1}^{U} \sum_{m=1}^{M} \vartheta_{2} \left(\frac{\mu_{2} - \nu_{2}}{2}\right) WY \times \\
\left[\frac{\left(\frac{\Lambda_{2}/\Delta_{sf}\rho x_{u}}{\varphi_{k}^{2}}\right)^{\frac{\varphi_{k}+1}{2}}}{(\varphi_{k}+1)\Gamma(\varphi_{k}+1)}\right], & \rho \leq \frac{\rho_{th}}{|h_{sd}^{\Sigma}|^{2}} \\
\sum_{u=1}^{U} \sum_{m=1}^{M} \vartheta_{2} \left(\frac{\mu_{2} - \nu_{2}}{2}\right) WZ \times \\
\left[\frac{\left(\frac{\Lambda_{2}}{\rho_{th}} \left(x_{u}\Omega_{sd}\right)}{\varphi_{k}^{2}}\right)^{\frac{\varphi_{k}+1}{2}}}{(\varphi_{k}+1)\Gamma(\varphi_{k}+1)}\right], & \rho \geq \frac{\rho_{th}}{|h_{sd}^{\Sigma}|^{2}}
\end{cases}$$
(4.33)

where,
$$W = \frac{\pi}{M} \sqrt{1 - x_m^2}$$
, $Y = H_u \frac{(x_u)^{N-1}}{\Gamma(N)}$, and $Z = H_u \frac{(x_u)^{L-1}}{\Gamma(L)}$.

Remark 4.2: From (4.32) and (4.33), it can be observed that for $\rho \to \infty$, the asymptotic ABLER for U_1 and U_2 does not depend upon the parameter of interference channels, such as Ω_{sd} , L and ρ_{th} . This is because the transmit SNR (ρ) of S is adjusted equally to ρ_{th} . Thus, the diversity order is equivalent to zero. Conversely, when $\rho_{th} \to \infty$, the asymptotic ABLER for U_1 and U_2 does not depend upon the parameter ρ and N.

4.4.5 Goodput Analysis

The effective goodput is a significant indicator for quantifying the actual useful data transferred through networks per unit of time. This metric also considers the total channel usage (i.e., training and data). For this reason, it is necessary to ascertain the number of channel uses allocated to data, ℓ_d , and training, ℓ_t , to estimate the goodput precisely. Mathematically, the system goodput (denoted by $\mathcal{G}_i, i \in \{1, 2\}$) can be evaluated from [121], and expressed as

$$\mathcal{G}_i = \left(1 - \frac{\ell_t}{\mathbb{L}}\right) (1 - \overline{\Xi}_i) \left(\frac{\mathbb{N}_i}{\ell_d}\right). \tag{4.34}$$

4.4.6 Latency and Reliability Analysis

Latency in the physical layer is measured as the typical time for a packet to be sent and decoded by the radio interface. Meanwhile, reliability is the likelihood of successfully transmitting N_i bits of information across a certain channel quality in the allotted time on the user plane. Relying on the above definition, we assume the fixed, coherent time

Table 4.1: Simulation Parameters for RIS-CR-NOMA.

Parameter	Values
Distance between B and S , (d_{bs})	30m
Distance between S and PU, (d_{sd})	30m
Distance between S and U_1 , (d_{s1})	20m
Distance between S and R , (d_{sr})	50m
Distance between R and U_2 , (d_{r2})	50m
Number of antennas at B, (N)	7
Number of antennas at PU, (L)	4
Number of RIS elements, (K)	15
Interference power constraint (I_{th})	20 dB
PA factor, (a_1) and (a_2)	0.7 and 0.3
Time splitting coefficient, (α)	0.5
Target rate for U_1 , (r_1)	1 Bits/s/Hz
Target rate for U_2 , (r_2)	$0.5 \; \mathrm{Bits/s/Hz}$
Energy conversion efficiency factor, (η)	0.7
Bandwidth (BW)	10 MHz
Noise power (σ^2)	-100dBm
Number of information bits at U_1 (\mathbb{N}_1)	200
Number of information bits at U_2 (\mathbb{N}_2)	150
Number of channel uses (total blocklength), (m_T)	600
Blocklength for data (ℓ_d) and training (ℓ_t)	400 and 100
Number of channel uses for EH, (m_{EH})	100
Coherence time (T)	$0.003~\mathrm{ms}$
Complexity accuracy trade-off factor (M) and (U)	50 and 300
Pathloss at reference distance d_o , (\mathcal{A}_o)	30dB
Pathloss exponent (α)	3
Rician factor (κ)	-5 dB
Frequency-dependent coefficient (ϱ)	1

block for each channel use is T (in ms). Therefore, mathematically latency, \mathcal{L} (in ms) and reliability, \mathcal{R} (in%) for user $U_i, i \in \{1,2\}$ can be evaluated from [121], respectively as

$$\mathcal{L}_{i} = \frac{\ell_{d}}{\left(1 - \overline{\Xi}_{i}\right)} \times T, \quad \mathcal{R}_{i} = \left(1 - \overline{\Xi}_{i}\right) \times 100. \tag{4.35}$$

4.5 Simulation Results and Discussion

This section presents the Monte-Carlo simulation (Sim.) results to validate the analytical results. All the simulation parameters are set according to [84, 85, 86, 122, 73]. Unless otherwise stated, all the parameter values are taken as mentioned in Table. 4.1.

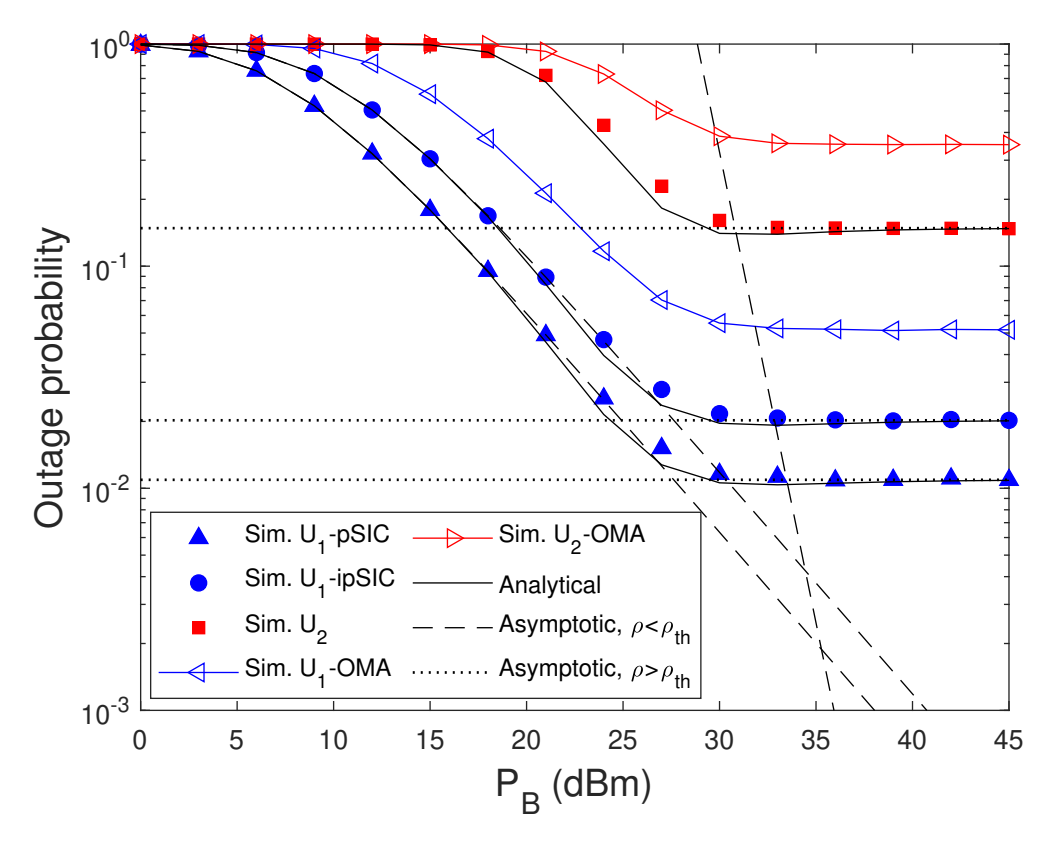


Figure 4.3: Comparison of OP vs. transmit power.

4.5.1 Infinite Blocklength Transmission

In Figure 4.3, the OP of U_1 and U_2 is plotted versus P_B for N=7, L=4, and $\psi=$ 0.25. It can be observed that the OP of the wireless-powered RIS-assisted CR-NOMA system outperforms the wireless-powered RIS-assisted CR-OMA. This is because NOMA enhances user fairness. The analytical results of OP for U_1 (with pSIC and ipSIC) and U_2 match well with the simulations. It can also be observed that the performance of OP for wireless-powered RIS-assisted CR-NOMA of U_1 with pSIC performs better than the ipSIC case. Additionally, the OP of U_1 and U_2 matches with the asymptotic OP at $\rho < \rho_{th}$, but when ρ is far greater than ρ_{th} , the OP tends to approach at a constant value and converges to asymptotic OP at $\rho > \rho_{th}$. This is because for $\rho < \rho_{th}$, the transmit SNR limits the interference constraint, and for $\rho > \rho_{th}$, the interference constraint limits the transmit SNR, which is consistent with **Remark 4.1**. In Figure 4.4, the impact of the number of RIS elements, K = 5, 10, 15, 20, is observed on the OP of the system. As can be observed from Figure 4.4, as K increases, the OP decreases for U_2 , while the performance of U_1 In Figure 4.5, the OP for U_1 with pSIC and U_2 is plotted against remains unaltered. P_B for varying HIs. As the degree of HIs varies from, $k_s = k_1 = k_2 = 0.05, 0.2, 0.3$, the

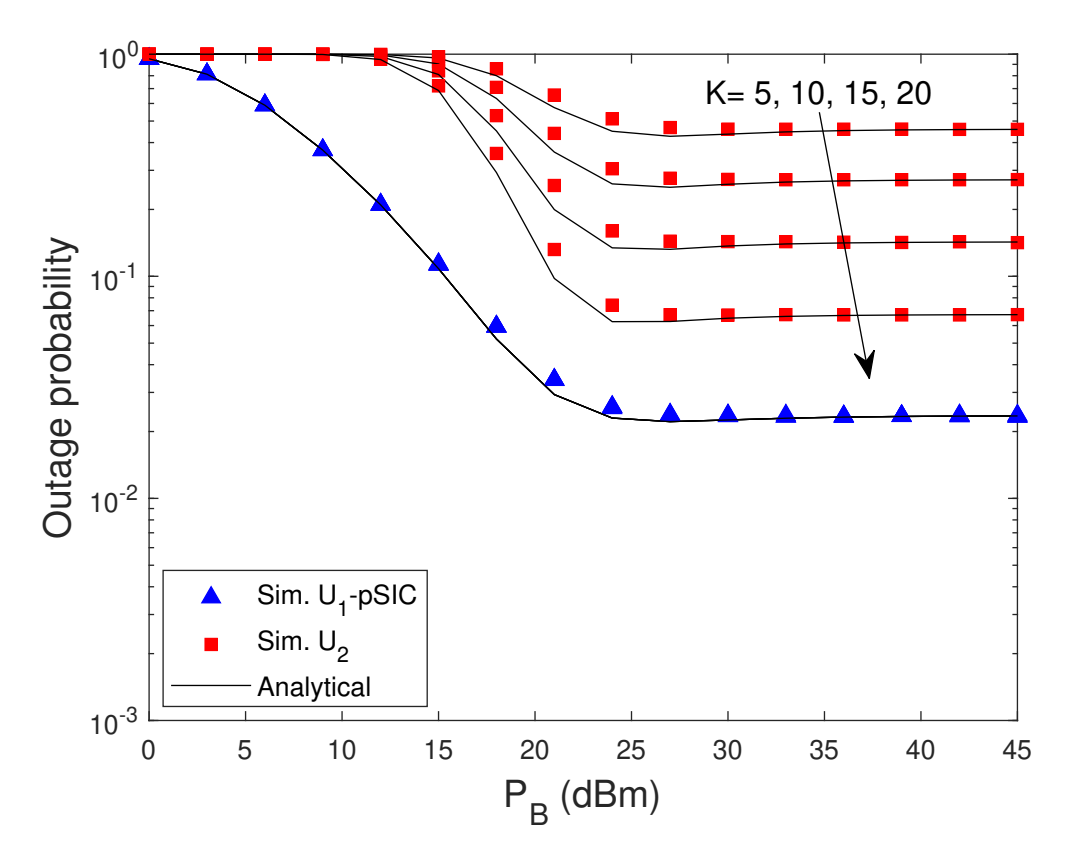


Figure 4.4: Comparison of OP vs. transmit power for varying K.

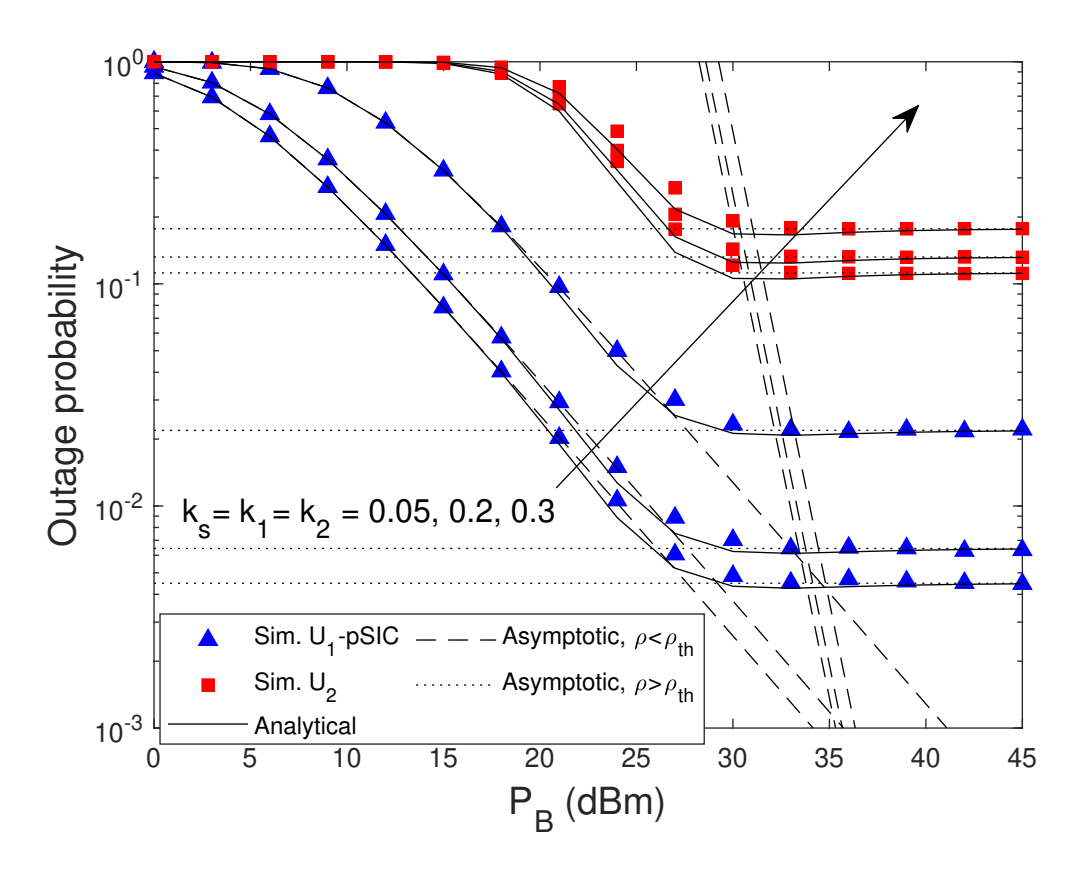


Figure 4.5: Comparison of OP vs. transmit power for varying HIs.

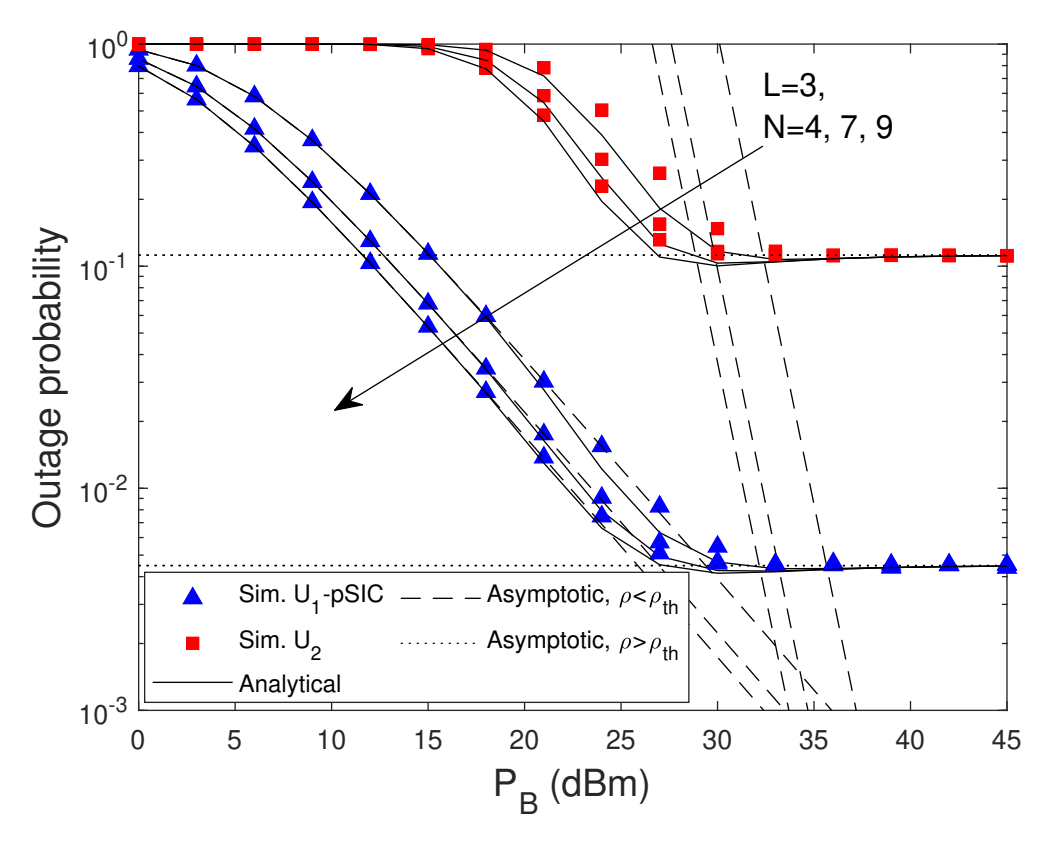


Figure 4.6: Comparison of OP vs. transmit power for varying N.

gap between OP curves for U_1 and U_2 increases and OP degrades. The analytical results corroborate with the simulation. It should be noted that the slope of the curves remains unaffected by the increase in the degree of HIs. Figure 4.6 illustrates the impact of varying number of antennas at B, i.e., N = 4,7,9 and L = 3 versus P_B . As can be observed from the figure, as the number of antennas increases at B, the OP for U_1 and U_2 gradually decrease up to $P_B = 30$ dBm and $P_B = 35$ dBm, respectively. After that, the OP for U_1 and U_2 increases with higher P_B and is saturated to the error floor with the asymptotic value of OP, for $\rho > \rho_{th}$. This is because as N increases, S has more opportunity to harvest a sufficient amount of energy for the data transmission to U_1 and U_2 . Figure 4.7 illustrates the impact of increasing the number of antennas, L, at the PU. It can be observed from the figure that as the L increases, the OP gradually decreases for all values of L for U_1 and U_2 until $P_B = 22$ dBm and $P_B = 27$ dBm, respectively. Furthermore, with higher values of P_B , the OP for U_1 and U_2 is drastically increased with an increase in the value of L and then saturates to the error floor. This is because more antennas at the PU lead to stricter interference constraints. Figure 4.8 illustrates the effect of the TS factor (α) on the OP of the system. As can be observed from the Figure 4.8, for $\alpha > 0.7$, the outage event start to occur at U_1 and U_2 regardless of the value of P_B . This is because S does not have enough

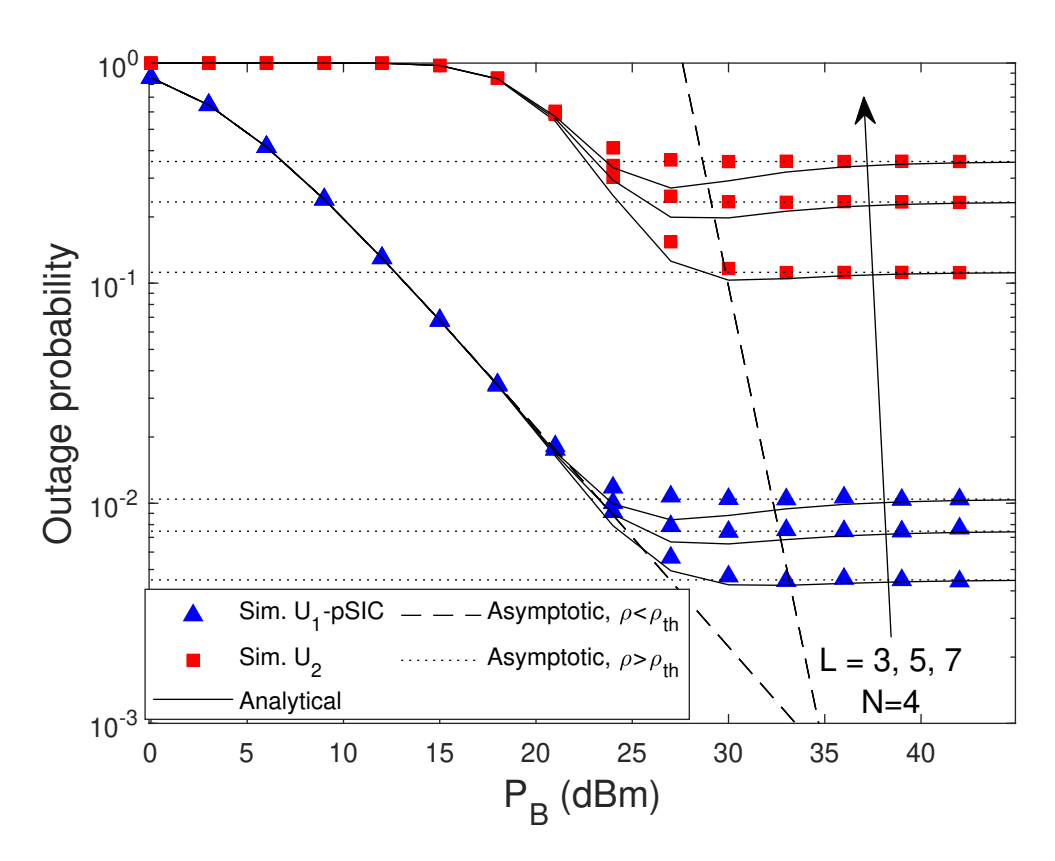


Figure 4.7: Comparison of OP vs. transmit power for varying L.

time for data transmission. Thus, the impact of α is more important than the effect of increasing transmit power for higher values of α . In Figure 4.9, the system throughput is plotted against P_B for both pSIC and ipSIC cases. It can be observed from the figure that the system throughput of our proposed wireless-powered RIS-assisted CR-NOMA system outperforms its OMA counterpart. The explanation for this situation lies in the fact that the power allocated for the transmission of user information in OMA is lower than that in NOMA, and a significantly longer time is required for slot transmission, which in turn leads to a reduction in both the decoding probability for users and the overall throughput of the system. The system throughput of the proposed system with pSIC performs better than the ipSIC case. The system throughput with ipSIC is plotted for $\psi = 0.2$, and it can be observed that the system throughput of our proposed system with ipSIC is still guaranteed to obtain higher throughput than that of OMA.

4.5.2 Finite Blocklength Transmission

In Figure 4.10, the ABLER of U_1 and U_2 is plotted against P_B for N=7, L=4, $\mathbb{N}_1=200$, $\mathbb{N}_2=150$ and $\psi=0.25$. It can be observed that the ABLER of the wireless-powered RIS-assisted CR-NOMA system outperforms the wireless-powered RIS-assisted CR-OMA.

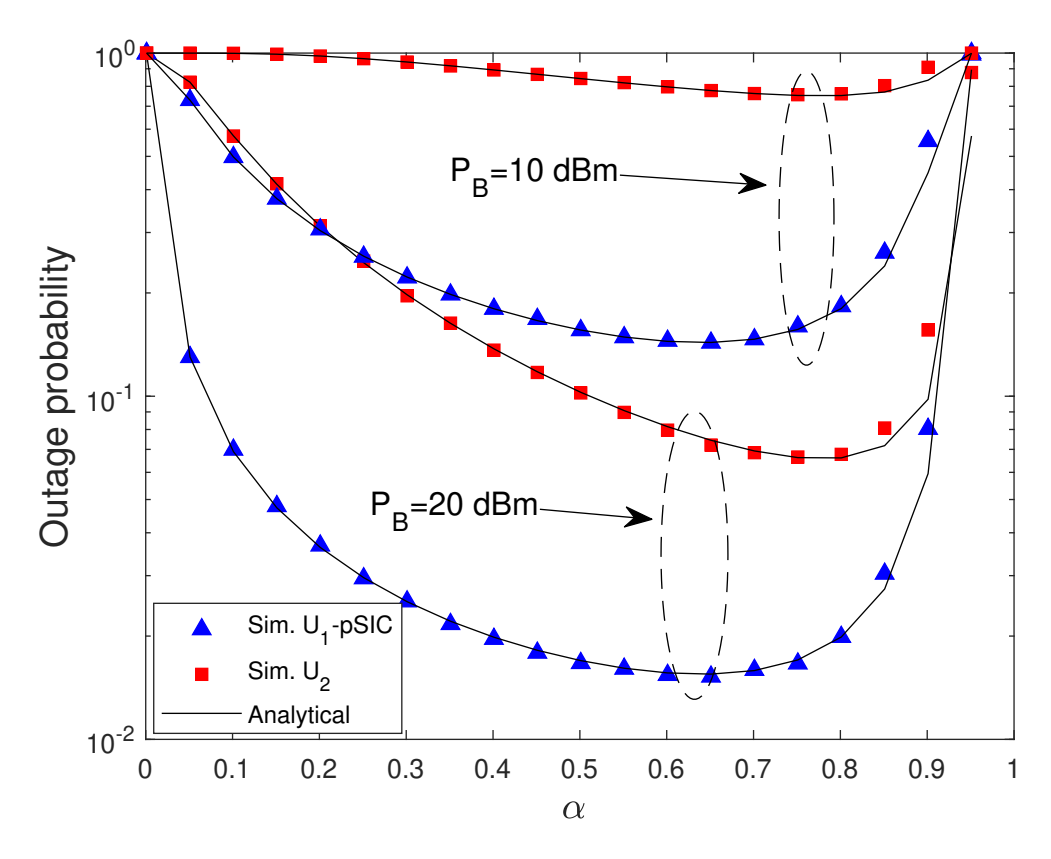


Figure 4.8: Comparison of OP vs. time splitting factor (α) .

The analytical results of ABLER for U_1 (with pSIC and ipSIC) and U_2 are plotted in reference to (4.30) and (4.31) and match well with the simulations. It can also be observed that the performance of ABLER for wireless-powered RIS-assisted CR-NOMA of U_1 with pSIC performs better than the ipSIC case with $\psi = 0.25$. Additionally, the ABLER of U_1 and U_2 matches with the asymptotic ABLER at $\rho < \rho_{th}$, but when ρ is far greater than ρ_{th} , the ABLER tends to approach at a constant value and converges to asymptotic ABLER at $\rho > \rho_{th}$. This is because for $\rho < \rho_{th}$, the transmit SNR limits the interference constraint, and for $\rho > \rho_{th}$, the interference constraint limits the transmit SNR, which is consistent with **Remark 2**. Figure 4.11 shows the impact of the number of RIS elements, K = 5, 10, 15, 20, on the ABLER of the system. As can be observed from Figure 4.11, as K increases, the ABLER decreases for U_2 , while the performance of U_1 remains unaltered. In Figure 4.12, we show the effect of varying blocklength $\mathbb{L} = (m_T - m_{EH})$ for $m_{EH} = 100$, $\ell_t=100,~\mathbb{N}_1=200,~\mathbb{N}_2=150,~\psi=0.25$ and $P_B=20$ dBm. As can be observed from the figure, if the block length of the data in the IT phase is increased, the ABLER decreases, and the system becomes more reliable because the packets are decoded with low decoding errors. Conversely, when the amount of information bits are fixed, the transmission rate will decrease due to an increase in block length. Again, the analytical and simulation

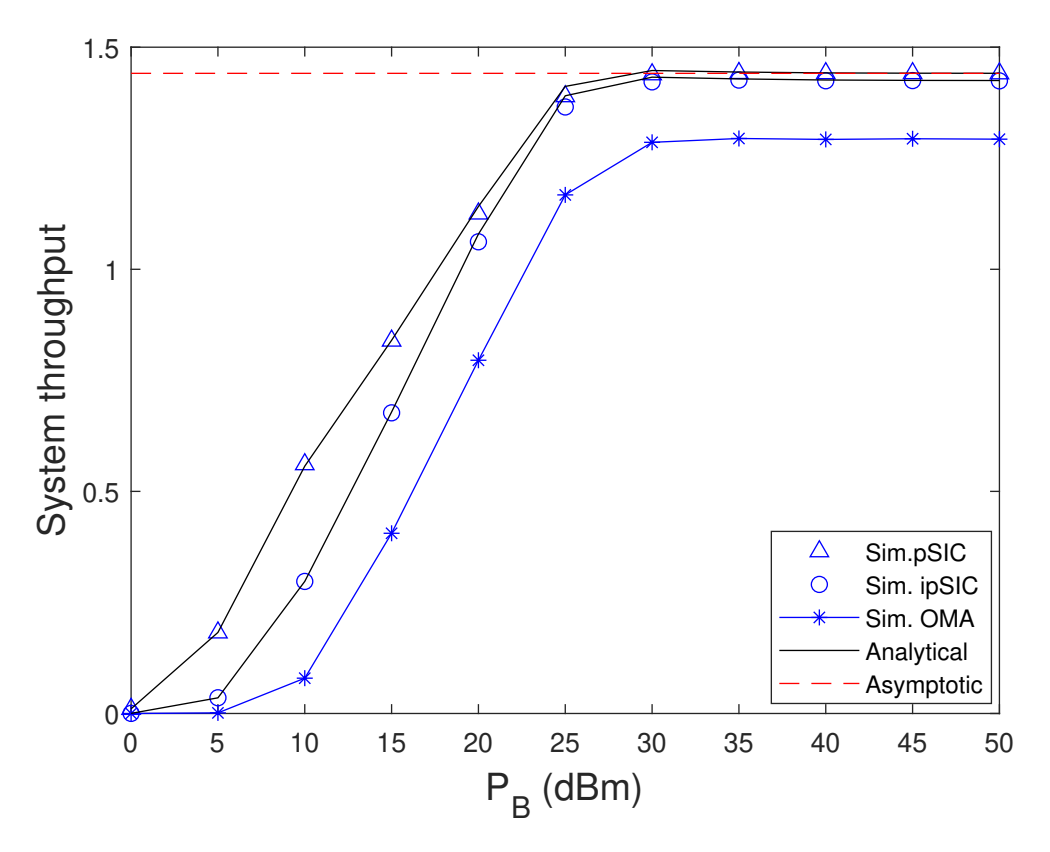


Figure 4.9: Comparison of system throughput vs. transmit power.

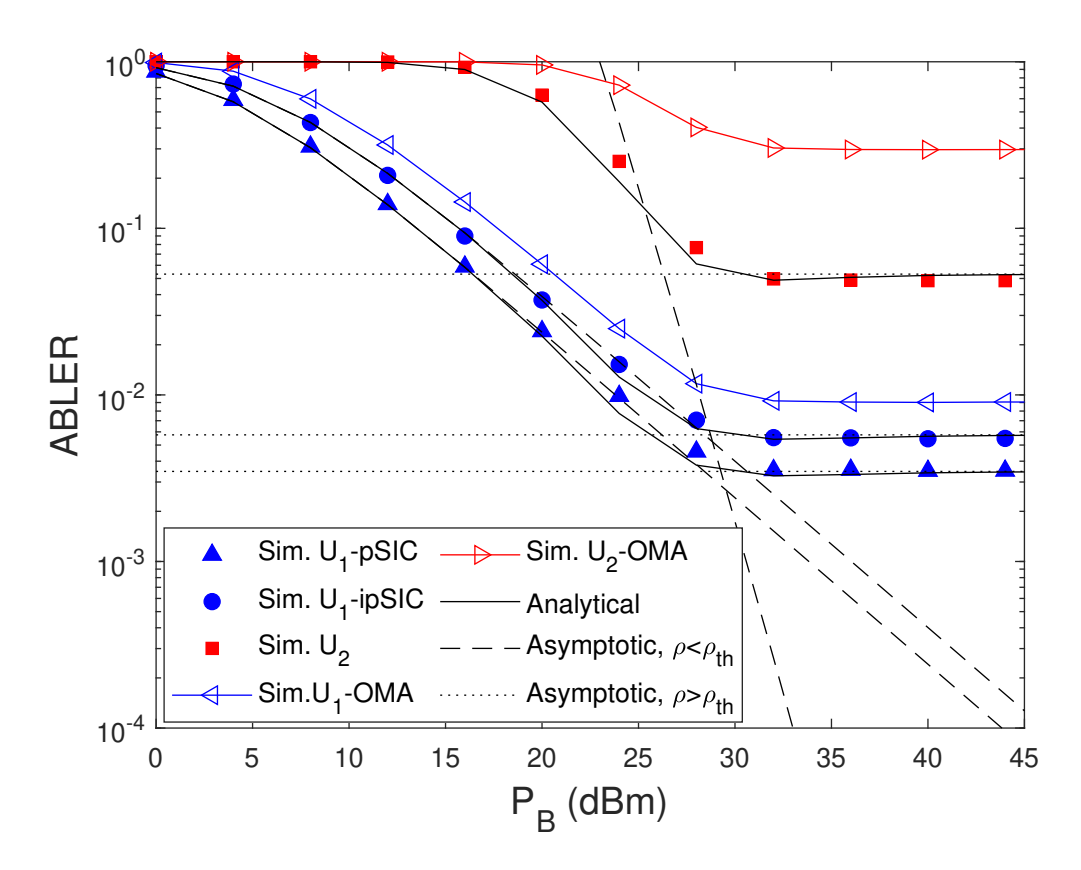


Figure 4.10: Comparison of ABLER vs. transmit power.

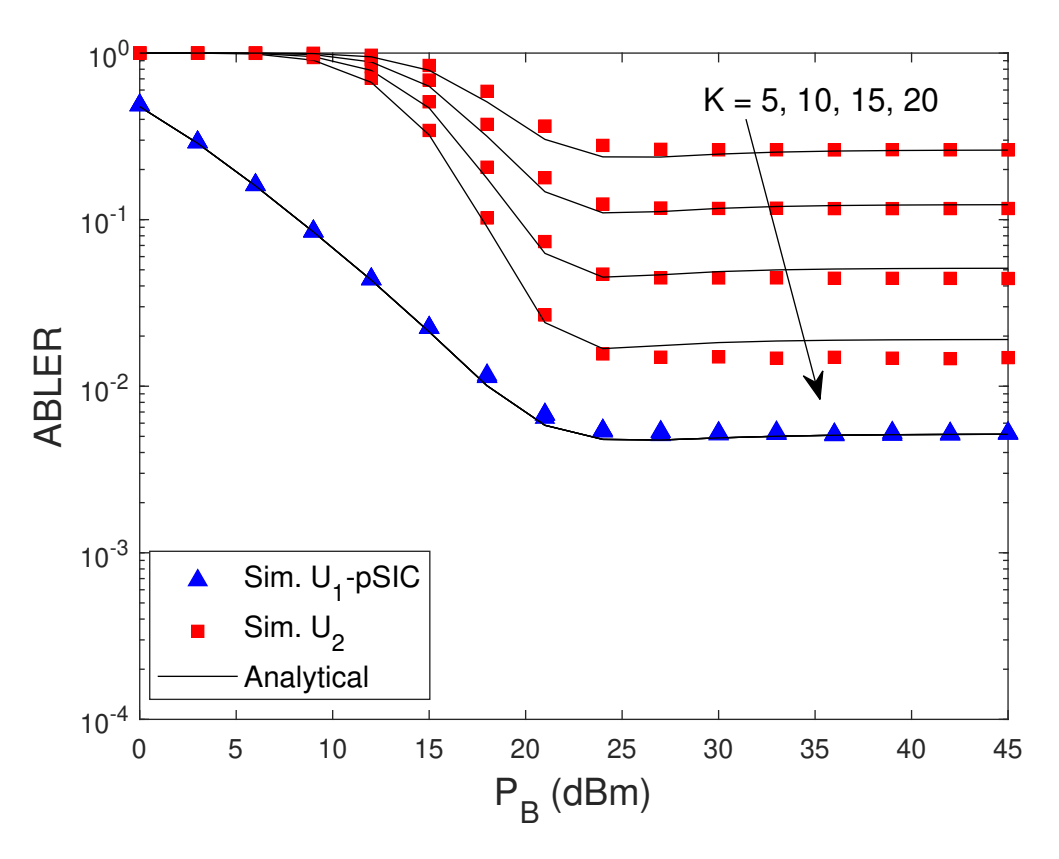


Figure 4.11: Comparison of ABLER vs. transmit power for varying K.

results are in agreement, and our theoretical analysis is validated. Figure 4.13 presents the variation of goodput as a function of P_B for the proposed system in the NOMA/OMA case. As can be observed from the figure, NOMA schemes outperform OMA for U_1 and U_2 . This is because the number of channel realizations to serve each user in the case of NOMA is twice that of OMA. As can be observed, as P_B increases, the goodput increases and converges at the floor. We have also shown the impact of varying number of antennas at B, i.e., N=4, 7, 9 with a fixed L=4. As can be observed from the figure, the goodput of the users increases as N increases because S has more opportunities for harvesting a sufficient amount of energy for packet transmission.

In Figure 4.14, the latency and reliability of U_1 and U_2 for the proposed system are plotted with P_B for N=7, L=4 and $\psi=0.1$ in the NOMA and OMA scenarios. As can be observed, the users U_1 and U_2 in the NOMA case outperform OMA in the latency and reliability analysis. It can be observed from the figure that latency curves decrease significantly from $P_B=0$ dBm to $P_B=20$ dBm. As P_B increases, the latency reaches saturation. This is because an increase in P_B leads to reduced ABLER. Conversely, reliability also increases significantly for a variation of P_B from $P_B=0$ dBm to $P_B=20$ dBm before reaching saturation. The proposed system performance of latency and

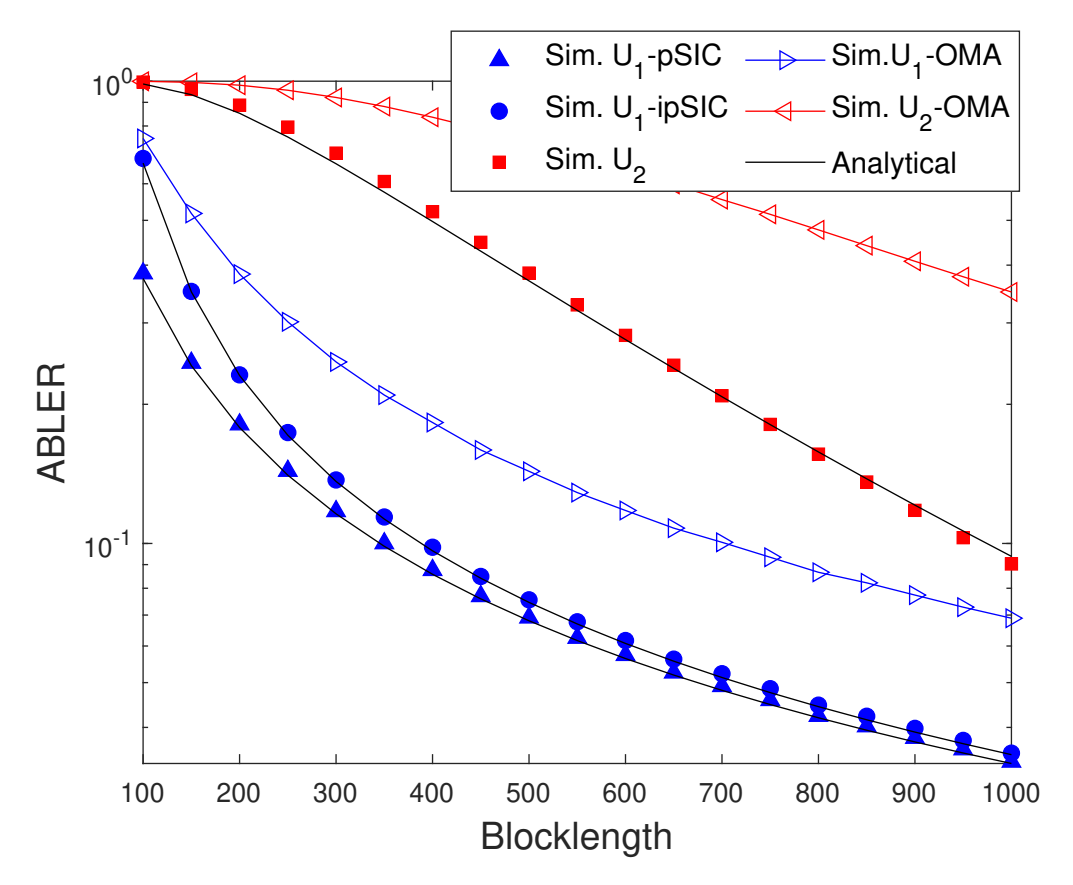


Figure 4.12: Comparison of ABLER vs. blocklength.

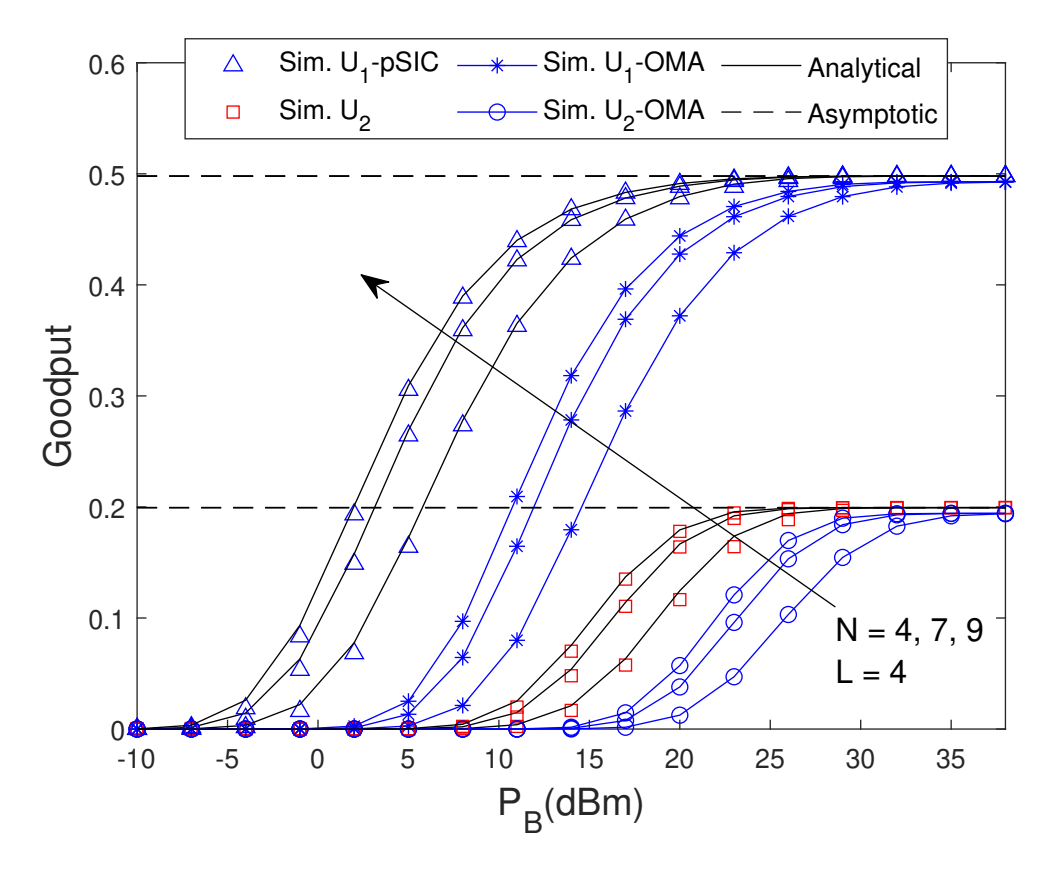


Figure 4.13: Comparison of goodput vs. transmit power.

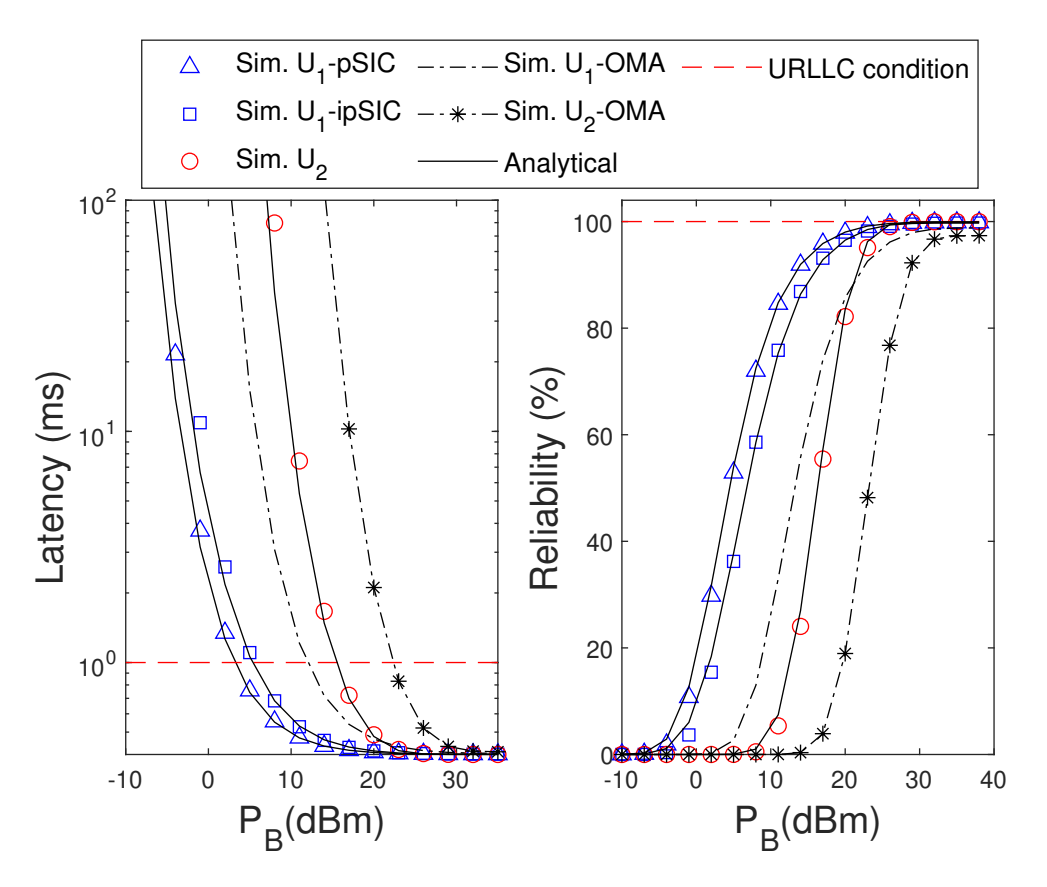


Figure 4.14: Comparison of latency and reliability vs. transmit power.

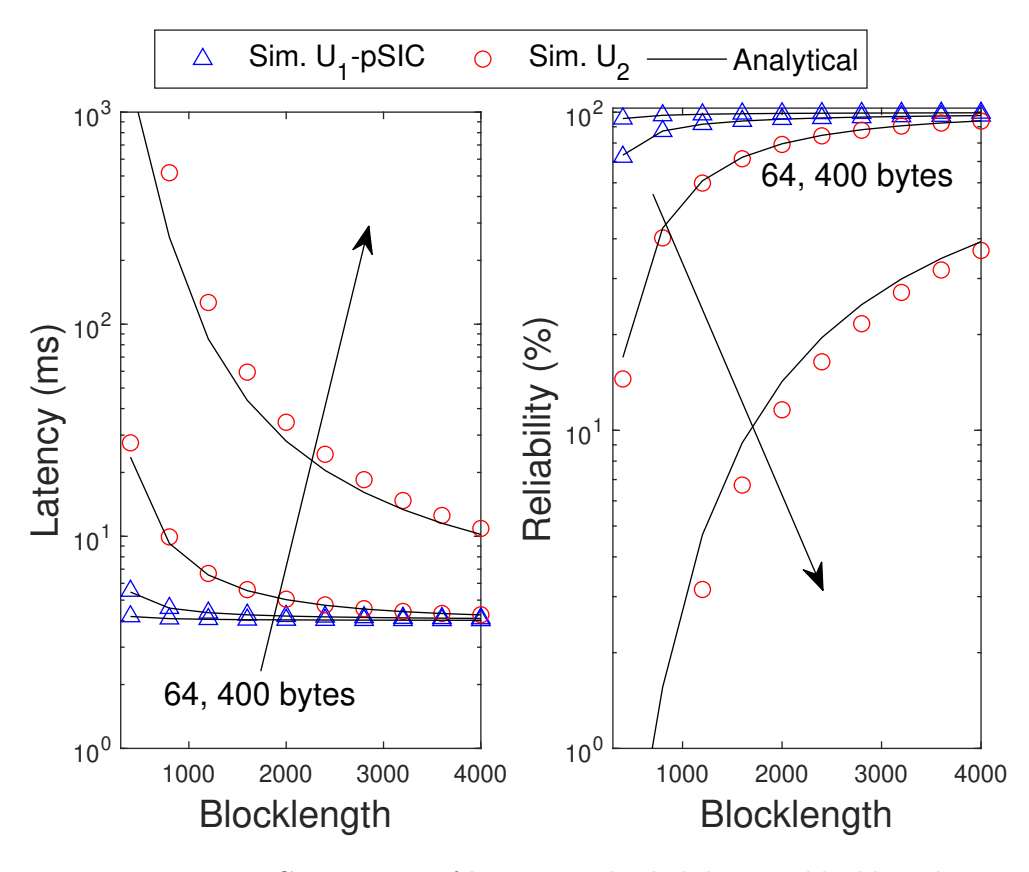


Figure 4.15: Comparison of latency and reliability vs. blocklength.

reliability is also compared with the URLLC requirement of latency (<1ms) and reliability (>99.99%). It can be observed from the figure that the proposed system meets the stringent requirement of 6G's URLLC use case. Figure 4.15 shows the impact of block length and the number of information bits on the latency and reliability of the proposed system for $P_B = 30$ dBm and $I_{th} = 10$ dB. It can be observed from (4.35) that latency and reliability are the function of blocklength and packet size. It can be observed from the figure that as the packet size increases from 64 to 400 bytes, the latency increases and reliability decreases. A tradeoff exists between packet size (information bits) and block length. As blocklength increases, the ABLER decreases, which results in lower latency and higher reliability, but as the packet size increases, the latency increases and reliability decreases. Therefore, as can be observed from the figure, when the packet size is 64 bytes, the system nearly achieves latency of 5 ms and reliability of 80% with blocklength of 2000. However, in the case of a longer packet size of 400 bytes, the latency and reliability change drastically with block length more than 4000.

4.6 Summary

This chapter presents a wireless-powered RIS-assisted CR-NOMA IoT system in which the secondary source harvests RF energy from a multiantenna power beacon and transmits information with the help of NOMA principle to two SUs: a near user, U_1 , through direct link and the far user, U_2 , with the help of RIS, under the multiantenna PU constraint with practical imperfection like HI and ipSIC. The performance of the considered system is analyzed using IBL and FBL transmission. For the IBL, the system performance is analyzed by deriving the analytical expression of OP and system throughput. For the FBL, the system performance is analyzed by deriving the analytical expression for the ABLER, goodput, latency, and reliability. Asymptotic analysis is also done at a higher transmit regime for both IBL and FBL with two different power settings scenarios: 1) when the transmit SNR of the secondary source leads the maximum interference constraint SNR $(\rho > \rho_{th})$, and 2) when the maximum interference constraint SNR leads the transmit SNR of the secondary source ($\rho < \rho_{th}$). Finally, Monte Carlo simulations are done to verify the analytical results. Numerical results show that: 1) analytical results corroborate with the simulation results; 2) the wireless-powered RIS-assisted CR-NOMA system outperforms its OMA counterpart in IBL and FBL analysis; 3) practical imperfections like HIs and ipSIC degrade the system performance; 4) when the transmit power of the secondary source is less than the maximum interference constraint, the OP and ABLER performance decreases

61

with increase in transmit power, but when maximum interference constraint is more than the transmit power of the secondary source, the OP and ABLER performance saturates to the error floor. Finally, the impact of other system parameters, such as the number of antennas at the B, the number of antennas at PU, the number of RIS elements, and the TS factor on the system performance is also examined.

Chapter 5

Finite Blocklength Analysis of ARIS-FDTW Communication with Hardware Impairments

The existing literature on RIS-FDTW communication [53, 68, 69, 72] considered the Rayleigh fading for the analysis and LI as Gaussian noise, except [70, 73], that focused on Nakagami-m fading and [71] where Weibull fading was used. Additionally, previous studies considered PRIS, that suffers from multiplicative fading attenuation. Therefore, analyzing the performance with ARIS [33] is worth investigating. Furthermore, to the best of our knowledge, none of the previous studies investigated the performance of the ARIS-FDTW system under the FBL regime, which is required for URLLC communication [119, 46] scenarios, where Shannon capacity theorem no longer holds.

This chapter investigates the performance of ARIS-FDTW communication in the presence of hardware impairments over cascaded Rician fading channels under the FBL regime. We derived novel analytical and asymptotic expressions for ABLER, ergodic capacity, system throughput, goodput, and latency. Monte Carlo simulations are performed to verify the analytical results. Numerical results revealed the superior performance of the ARIS-FDTW system compared to its passive counterpart and conventional FDTW-AF and FDTW-DF relay systems.

5.1 System Model

We consider an ARIS-assisted FDTW network composed of an ARIS (R) having N elements and two FD-IoT¹users, (U_1) and (U_2) , who want to exchange their information (SPs) with the assistance of ARIS (see Figure 5.1). Each user has two antennas (one each

¹Considered system model can be applied to multiple critical IoT scenarios, such as factory automation, autonomous vehicle, telesurgery, etc., where a small amount of information to be exchanged among nodes.

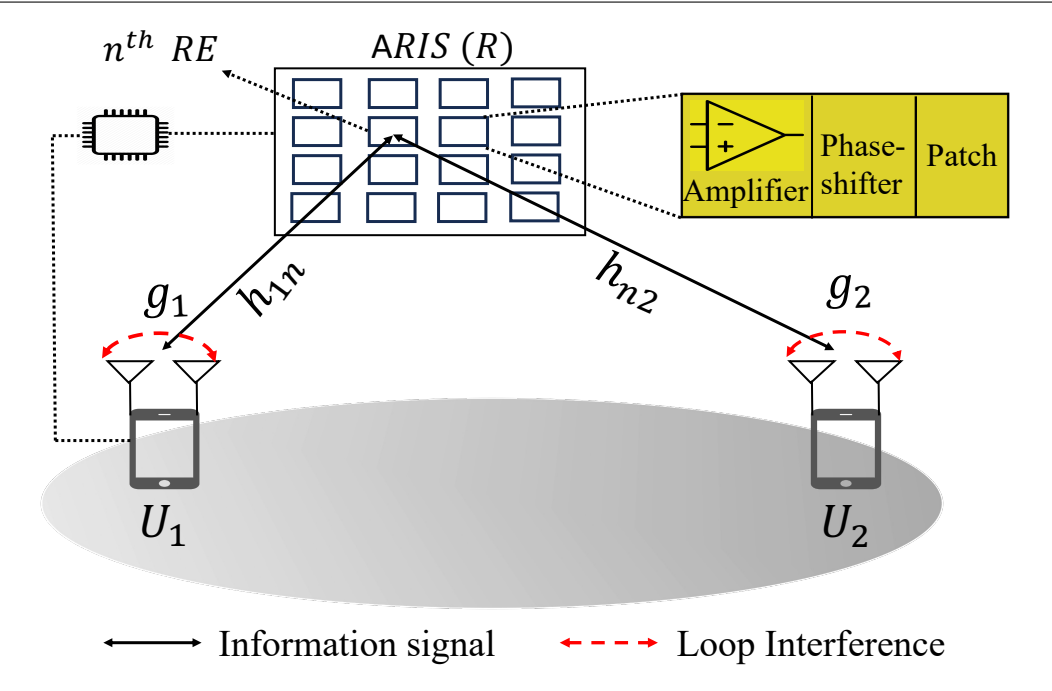


Figure 5.1: ARIS-assisted FDTW network.

for transmission and reception) to enable FD mode. Therefore, U_1 and U_2 can transmit and receive simultaneously. We also assume that the direct link between two users is blocked due to deep shadowing. Due to the FD mode, U_1 and U_2 experience signal interference from their output to input. Specifically, current ARIS systems share phase shift circuitry with PRIS and use power amplifiers to boost the radiated signal. Incident signals at ARIS are amplified and reflected to the target user [33]. The reflection amplification matrix at the ARIS is defined as $\Theta = \sqrt{\beta} diag(e^{j\theta_1}, e^{j\theta_2}, \dots, e^{j\theta_N}) \in \mathbb{C}^{N \times N}$, where $\theta_n \in [0, 2\pi)$ indicates the n^{th} RIS element phase shift, while β indicates the amplification coefficient. In PRIS, β is typically set to 1; however, ARIS may increase β by using a tunneling reflection amplifier for each RIS element. We assume the channels to be reciprocal. The wireless channel fading coefficient vector from U_1 to R is $\boldsymbol{h}_{1r} = [h_{11}, h_{12} \cdots h_{1N}]^H \in \mathbb{C}^{N \times 1}$ and from R to U_2 is $h_{r2} = [h_{12}, h_{22} \cdots h_{N2}]^H \in \mathbb{C}^{N \times 1}$. The channel fading coefficients undergo Rician fading, with $h_{XY} = \sqrt{\eta_{XY}} \left(\sqrt{\kappa/(\kappa+1)} + \sqrt{1/(\kappa+1)} \tilde{h}_{XY} \right)$, where, $X = \{1, n\}$, $Y=\{n,2\}, \ \kappa \ \text{is the Rician factor}, \ \tilde{h}_{XY} \sim \mathcal{CN}(0,1), \ \text{and} \ \eta_{XY}=\varrho d_{XY}^{-\alpha}, \ \text{with} \ d_{XY}$ being the distance between nodes X and Y and α , ϱ are the path loss exponent and frequency-dependent coefficient, respectively.

5.1.1 Signal Model

Without the loss of generality, we consider the case when U_1 sends the information to U_2 with the assistance of R. In addition, we assume HIs in the hardware of U_1 and U_2

as specified in [82]. Based on the above assumption, the received signal at U_2 can be expressed as

$$y_{2} = \underbrace{\sqrt{P_{1}\beta}\boldsymbol{h}_{r2}^{H}\boldsymbol{\Phi}\boldsymbol{h}_{1r}(x_{1} + \varepsilon_{12})}_{\text{Desired signal at }U_{2}} + \underbrace{\sqrt{P_{2}}g_{2}(x_{2} + \varepsilon_{22})}_{\text{Loop interference (LI)}} + \underbrace{\sqrt{P_{2}\beta}\boldsymbol{h}_{2r}^{H}\boldsymbol{\Phi}\boldsymbol{h}_{r2}(x_{2} + \varepsilon_{22})}_{\text{Self interference at }U_{2}} + \underbrace{\sqrt{\beta}(\boldsymbol{h}_{r2}^{H}\boldsymbol{\Phi}\boldsymbol{w}_{r})}_{\text{CM}} + w_{2},$$

$$\underbrace{\sqrt{\beta}(\boldsymbol{h}_{r2}^{H}\boldsymbol{\Phi}\boldsymbol{w}_{r})}_{\text{Thermal noise at ARIS (R)}} + w_{2},$$

$$(5.1)$$

where, $\mathbf{\Phi} = diag(e^{j\theta_1}, e^{j\theta_2}, \dots, e^{j\theta_N}); P_1, P_2$ are the transmitted power of U_1 and U_2 , respectively; x_1 and x_2 are the transmitted signals of U_1 and U_2 with unity power, respectively; $w_2 \sim \mathcal{CN}(0, \sigma_2^2)$ is the AWGN at U_2 . Furthermore, $\varepsilon_{12} \sim \mathcal{CN}(0, P_1\beta |\mathbf{h}_{r2}^H\mathbf{\Phi}\mathbf{h}_{1r}|^2k_{12}^2)$ denotes the distortion due to HI from the transmitter of U_1 and receiver of U_2 and $\varepsilon_{22} \sim \mathcal{CN}(0, P_2|g_2|^2k_{22}^2)$ denote the distortion due to HI from the transmitter and receiver of U_2 . Furthermore, $k_{12}^2 = k_{1t}^2 + k_{2r}^2$ denotes the degree of HI including k_{1t} at the transmitter of U_1 and U_2 and U_3 at the receiver of U_3 . Similarly, U_3 and U_4 are the receiver of U_4 and U_4 and U_4 are the receiver of U_4 and U_4 and U_4 are the receiver of U_4 . Next, U_4 and U_4 are the receiver of U_4 and applying analog and digital suppression techniques [62], U_4 can remove self-interference from its received signal [53, 68, 69, 70, 72]. Therefore, the SIDNR at U_4 can be written as

$$\Upsilon_{2} = \frac{\beta P_{1} |\boldsymbol{h}_{r2}^{H} \boldsymbol{\Phi} \boldsymbol{h}_{1r}|^{2}}{\beta P_{1} |\boldsymbol{h}_{r2}^{H} \boldsymbol{\Phi} \boldsymbol{h}_{1r}|^{2} k_{12}^{2} + P_{2} |g_{2}|^{2} \chi_{g} + \beta |\boldsymbol{h}_{r2}^{H} \boldsymbol{\Phi} \omega_{r}|^{2} + \sigma_{2}^{2}}.$$
(5.2)

where, $\chi_g = (1 + k_{22}^2)$ and $g_2 \sim \mathcal{CN}(0, \Omega_{LI})$ is the LI channel between the transmit and receive antennas of U_2 . The term $|\boldsymbol{h}_{r2}^H \boldsymbol{\Phi} \omega_r|^2$ can be approximated² as $\eta_{n2} \sigma_r^2 \zeta$, where, $\zeta = N\left(\frac{N\kappa+1}{\kappa+1}\right)$.

5.1.2 Channel Statistics

Let $\mathcal{X} = \left|\sum_{n=1}^{N} h_{1n} e^{j\theta_n} h_{n2}\right|^2$ for notational simplicity. By using coherent phase shift design as previously proposed in [53, 68, 70, 72] to facilitate constructive reception at U_2 , the phase shift of the n^{th} elements of R is set as $\theta_n = -arg(h_{1n}) - arg(h_{n2})$; therefore, $\mathcal{X} = \left(\sum_{n=1}^{N} \left|h_{1n}h_{n2}\right|\right)^2$. Let us assume that $X_n = \left|h_{1n}h_{n2}\right|$, so the mean and variance of

 $^{^2\}Phi$ is aligned with $|\boldsymbol{h}_{r2}^H\Phi\boldsymbol{h}_{1r}|$ therefore, the term $|\boldsymbol{h}_{r2}^H\Phi\omega_r|$ is randomly distributed and thus can be characterized with its mean power [123].

 X_n can be written as

$$\mu_n = \mathbb{E}[X_n] = \frac{\pi \sqrt{\eta_{1n} \eta_{n2}}}{4(\kappa + 1)} \left[L_{\frac{1}{2}}(-\kappa) \right]^2, \tag{5.3}$$

$$\Omega_n = Var(X_n) = \eta_{1n}\eta_{n2} \left[1 - \frac{\pi^2}{16(1+\kappa)^2} \left[L_{\frac{1}{2}}(-\kappa) \right]^4 \right].$$
 (5.4)

where, $L_{\frac{1}{2}}(\kappa) = e^{\frac{1}{2}} \left[(1-\kappa)I_0(-\frac{\kappa}{2}) - \kappa I_1(-\frac{\kappa}{2}) \right]$ is the Laguerre polynomial. Using Laguerre series approximation [118, Eq. (2.76)], we can obtain the approximate PDF and CDF of \mathcal{X} as

$$f_{\mathcal{X}}(x) = \frac{x^{\varphi_n} e^{-\frac{x}{\phi_n}}}{\phi_n^{\varphi_n + 1} \Gamma(\varphi_n + 1)}, \quad \mathcal{F}_{\mathcal{X}}(x) = \frac{\gamma\left(\varphi_n + 1, \frac{\sqrt{x}}{\phi_n}\right)}{\Gamma(\varphi_n + 1)}.$$
 (5.5)

where, $\varphi_n = \frac{N\mu_n^2 - \Omega_n}{\Omega_n}$ and $\phi_n = \frac{\Omega_n}{\mu_n}$.

5.2 Performance Analysis

5.2.1 Calculation of ABLER at U_2

It is assumed that communication occurs in a time-slotted fashion, and each time slot has a blocklength of $\mathbb{L} = \ell_d + \ell_t$, where ℓ_d and ℓ_t are the blocklength for data and training, respectively. Let Ξ_2 be the BLER, K_2 be the number of information bits, and ℓ_d be the blocklength for U_2 . Accordingly, the maximum achievable rate at U_2 is expressed as $r_2 = \frac{K_2}{\ell_d}$. Therefore, ABLER can be obtained by averaging Ξ_2 over SIDNR Υ_2 , as mentioned in section 4.4.1.

By using the steps mentioned in Appendix A.5, the ABLER of the ARIS-FDTW system with HIs can be expressed as

$$\overline{\Xi}_{2}^{ARIS} \approx \vartheta_{2} \left(\frac{\mu_{2} - \nu_{2}}{2} \right) \sum_{m=1}^{M} \frac{\pi}{M} \sqrt{1 - x_{m}^{2}} \left[\sum_{u=1}^{U} H_{u} \frac{1}{\Gamma(\varphi_{n} + 1)} \times \left(\frac{\sqrt{\Lambda(b_{n}x_{u} + c_{n})}}{\sqrt{\beta}\phi_{n}} \right) \right],$$
(5.6)

where, $x_m = cos\left(\frac{2m-1}{2M}\pi\right)$, $\Lambda = \frac{z_m}{P_1(1-z_mk_{12}^2)}$, $z_m = \left(\frac{\mu_2-\nu_2}{2}\right)x_m + \left(\frac{\mu_2+\nu_2}{2}\right)$, $b_n = P_2\chi_g\Omega_{LI}$, $c_n = \left(\beta\eta_{n2}\sigma_r^2\zeta + \sigma_2^2\right)$ and M is the complexity trade-off factor. x_u is the u-th zero point (abscissa) of Laguerre polynomial, $L_U(x) = \frac{e^x}{U!}\frac{d}{dx^U}\left(x^Ue^{-x}\right)$, u-th weight can be expressed as $H_U = \frac{\left(U!\right)^2x_u}{\left[L_{U+1}(x_u)\right]^2}$, and U is the Laguerre tradeoff factor. The ABLER can be obtained for PRIS by putting $\beta = 1$ and $\sigma_r^2 = 0$ in (5.6).

5.2.2 Asymptotic ABLER at U_2

The asymptotic ABLER can be obtained by setting $P_1, P_2 \to \infty$ in (5.6); therefore, the asymptotic ABLER at U_2 can be expressed as

$$\Xi_{2}^{ARIS,\infty} \approx \vartheta_{2} \left(\frac{\mu_{2} - \nu_{2}}{2}\right) \sum_{m=1}^{M} \frac{\pi}{M} \sqrt{1 - x_{m}^{2}} \left[\sum_{u=1}^{U} H_{u} \frac{1}{\Gamma(\varphi_{n} + 1)} \times \left(\varphi_{n} + 1, \frac{\sqrt{z_{m} \Omega_{LI} \chi_{g} x_{u}}}{\sqrt{\beta(1 - z_{m} k_{12}^{2})} \phi_{n}}\right)\right].$$
(5.7)

Remark 5.1 At higher transmit power, ABLER converges to an error floor. Thus, the diversity order of U_2 is equivalent to zero because of the residual LI power. We also found that the diversity order is independent of the thermal noise of the ARIS.

5.2.3 Calculation of EC at U_2

The EC in FBL transmission at U_2 can be obtained as

$$\overline{R}_{2} = \mathbb{E} \left[\log_{2}(1 + \Upsilon_{2}) - \sqrt{V(\Upsilon_{2})} \left[\sqrt{\ell_{d}} \ln 2Q(\Xi_{2}) \right]^{-1} \right],$$

$$= \overline{C}(\Upsilon_{2}) - \overline{V}(\Upsilon_{2}) \left[\sqrt{\ell_{d}} \ln 2Q(\Xi_{2}) \right]^{-1},$$
(5.8)

where, $\overline{C}(\Upsilon_2) = \mathbb{E}\{\log_2(1+\Upsilon_2)\}$ and $\overline{V}(\Upsilon_2) = \mathbb{E}\{\sqrt{V(\Upsilon_2)}\}$. $\sqrt{V(\Upsilon_2)} = \sqrt{1-(1+\Upsilon_2)^{-2}} \approx 1-\frac{1}{2}(1+\Upsilon_2)^{-2}$. Therefore, $\overline{C}(\Upsilon_2)$ and $\overline{V}(\Upsilon_2)$ can be written as

$$\overline{C}(\Upsilon_2) = \int_0^\infty \frac{1 - \mathcal{F}_{\Upsilon_2}(x)}{\ln 2(1+x)} dx, \ \overline{V}(\Upsilon_2) \approx 1 + \int_0^\infty \frac{1 - \mathcal{F}_{\Upsilon_2}(x)}{\left(1+x\right)^3} dx. \tag{5.9}$$

Applying the GCQ [120] method and expression for $\mathcal{F}_{\Upsilon_2}(x)$ as specified in Appendix A.5, the closed-form expression of $\overline{C}(\Upsilon_2)$ and $\overline{V}(\Upsilon_2)$ in (5.9) can be written as

$$\overline{C}(\Upsilon_2) \approx \frac{\pi}{2Mk_{12}^2 \ln 2} \sum_{m=1}^{M} \frac{2k_{12}^2 \sqrt{1 - x_m^2}}{2k_{12}^2 + (x_m + 1)} \left[1 - \sum_{u=1}^{U} H_u \frac{1}{\Gamma(\varphi_n + 1)} \times \right]
\gamma \left(\varphi_n + 1, \frac{\sqrt{(x_m + 1)(b_n x_u + c_n)}}{\varphi_n \sqrt{k_{12}^2 \beta P_1 (1 - x_m)}} \right),$$
(5.10)

$$\overline{V}(\Upsilon_{2}) \approx \frac{\pi}{2Mk_{12}^{2} \ln 2} \sum_{m=1}^{M} \frac{8k_{12}^{6} \sqrt{1 - x_{m}^{2}}}{8k_{12}^{6} + (x_{m} + 1)^{3}} \left[1 - \sum_{u=1}^{U} H_{u} \frac{1}{\Gamma(\varphi_{n} + 1)} \times \left(\varphi_{n} + 1, \frac{\sqrt{(x_{m} + 1)(b_{n}x_{u} + c_{n})}}{\varphi_{n} \sqrt{k_{12}^{2} \beta P_{1}(1 - x_{m})}} \right) \right].$$
(5.11)

(5.8) shows that EC in FBL is a function of Υ_2 , ℓ_d and Ξ_2 . In FBL, EC also depends on the values of $\overline{C}(\Upsilon_2)$ and $\overline{V}(\Upsilon_2)$, which makes the computation complex. However, $\overline{C}(\Upsilon_2)$ acts as an upper bound for the EC in the FBL regime. The EC can be obtained for PRIS by using (5.8) and putting $\beta = 1$ and $\sigma_r^2 = 0$ in (5.10) and (5.11).

5.2.4 Aysmptotic EC at U_2

The asymptotic EC can be obtained by setting $P_1, P_2 \to \infty$ in (5.10) and (5.11); therefore, the asymptotic EC at U_2 can be expressed as $\overline{R}_2^{\infty} \approx [\overline{C}^{\infty}(\Upsilon_2) - \overline{V}^{\infty}(\Upsilon_2)(\sqrt{\ell_d}\ln 2Q(\Xi_2))^{-1}]$, where $\overline{C}^{\infty}(\Upsilon_2)$ and $\overline{V}^{\infty}(\Upsilon_2)$ represented as

$$\overline{C}^{\infty}(\Upsilon_{2}) \approx \frac{\pi}{2Mk_{12}^{2} \ln 2} \sum_{m=1}^{M} \frac{2k_{12}^{2} \sqrt{1 - x_{m}^{2}}}{2k_{12}^{2} + (x_{m} + 1)} \left[1 - \sum_{u=1}^{U} H_{u} \frac{1}{\Gamma(\varphi_{n} + 1)} \times \right]
\gamma \left(\varphi_{n} + 1, \frac{\sqrt{(x_{m} + 1)(\chi_{g}\Omega_{LI}x_{u})}}{\varphi_{n}\sqrt{k_{12}^{2}\beta(1 - x_{m})}} \right),$$
(5.12)

$$\overline{V}^{\infty}(\Upsilon_{2}) \approx \frac{\pi}{2Mk_{12}^{2} \ln 2} \sum_{m=1}^{M} \frac{8k_{12}^{6} \sqrt{1 - x_{m}^{2}}}{8k_{12}^{6} + (x_{m} + 1)^{3}} \left[1 - \sum_{u=1}^{U} H_{u} \frac{1}{\Gamma(\varphi_{n} + 1)} \right] \times \gamma \left(\varphi_{n} + 1, \frac{\sqrt{(x_{m} + 1)(\chi_{g}\Omega_{LI}x_{u})}}{\varphi_{n}\sqrt{k_{12}^{2}\beta(1 - x_{m})}} \right).$$
(5.13)

Remark 5.2 The evaluation metric utilized to capture the diversity of EC using transmit power is the multiplexing gains at higher transmit power. Based on (5.12) and (5.13), we can observe that the EC of U_2 reaches the throughput ceiling, yielding zero multiplexing gain as the transmit power reaches infinity.

5.2.5 Throughput, Goodput and Latency analysis

Throughput is a performance parameter used to evaluate communication system efficacy at a constant channel coding rate, whereas goodput is defined as the the number of information bits reliably delivered in a specific time. Latency in the physical layer refers to the time that the radio interface takes to send and decode a packet. Mathematically, throughput (\mathcal{T}_2) and goodput (\mathcal{G}_2) (in bits/s/Hz) and latency (\mathcal{L}_2) (in ms) for U_2 can be defined as

$$\mathcal{T}_2 = r_2 \left(1 - \overline{\Xi}_2 \right), \ \mathcal{G}_2 = \left(1 - \frac{\ell_t}{\mathbb{L}} \right) \mathcal{T}_2, \ \mathcal{L}_2 = \frac{\ell_d T}{\left(1 - \overline{\Xi}_2 \right)}.$$
 (5.14)

Table 5.1: Simulation Parameters for ARIS-FDTW system.

Parameter	Values
Distance between U_1 and R (d_{1r})	15m
Distance between R and U_2 (d_{r2})	20m
Thermal noise power at ARIS (σ_r^2)	-30 dBm
Number of ARIS elements (N)	15
Amplitude of ARIS reflection coefficient (β)	4
Bandwidth (BW)	10 MHz
Noise figure (NF)	10
Number of information bits at U_2 (K_2)	150
Blocklength for data (ℓ_d) and training (ℓ_t)	300 and 100
Coherence time (T)	$0.003~\mathrm{ms}$
Complexity accuracy trade-off factor (M) and (U)	50 and 300
Pathloss exponent (α)	2.2
Rician factor (κ)	-5 dB
Frequency-dependent coefficient (ϱ)	1

5.3 Simulation Results and Discussion

This section presents the results of the Monte-Carlo simulation (Sim.) to validate the analytical results. All simulation parameters are set following [70, 68, 82]. The noise power is set as $\sigma_2^2 = -174 + 10 \log_{10}(BW) + NF$. Unless otherwise stated, all parameters are set accordingly to Table 5.1. Furthermore, we consider that $P_1 = P_2 = P$.

In Figure 5.2, we represent the ABLER for ARIS-FDTW and PRIS-FDTW scenarios to compare with that of FDTW-AF and FDTW-DF relay systems. As shown in Figure 5.2, ARIS-FDTW systems perform better than the PRIS-FDTW and conventional FDTW-AF and FDTW-DF relay systems. In Figure 5.3, ABLER is plotted against the P for different values of k_{12} and k_{22} . The results reveal that our analytical results match the simulated ones, and the ARIS-FDTW system outperforms the PRIS-FDTW system. With an increase in the degree of HI, i.e., $k_{12} = k_{22} = 0.01, 0.3, 0.6$, the gap between ABLER curves increases at higher P, while the performance degrades. At higher P, the curves converge to an error floor because of the LI according to Remark 5.1. Furthermore, the slopes of the curves remain unchanged regardless of the degree of HIs. Figure 5.4 compares the EC for the ARIS-FDTW system with the PRIS-FDTW system under varying HIs when $\Xi_2 = 0.01$. As shown in Fig. 5.4, our analytical results corroborate with the simulation. The ARIS outperforms PRIS because of the amplification factor β . The EC starts degrading with an increase in the level of HI, i.e., $k_{12} = k_{22} = 0.1, 0.15, 0.3$. At higher P, EC converges to a throughput ceiling. This is so because of the LI power, which also increases with the increase in transmit power, P.

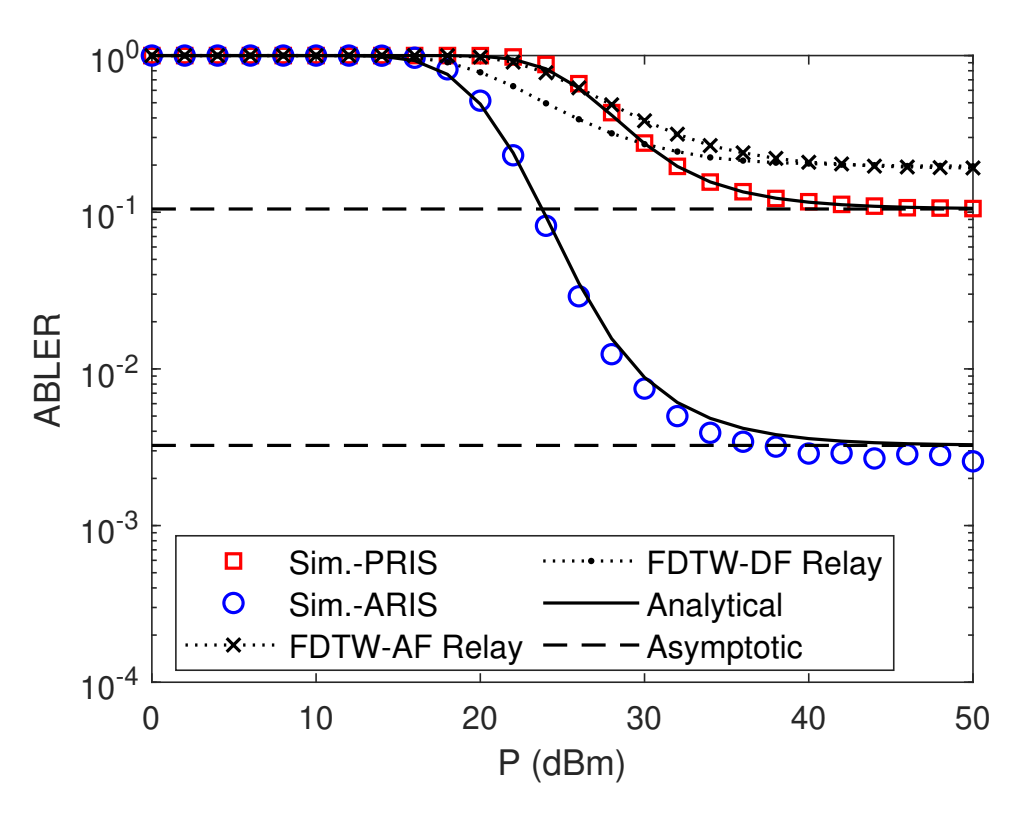


Figure 5.2: Comparison of ABLER vs. transmit power with conventional FDTW-AF and FDTW-DF relay systems.

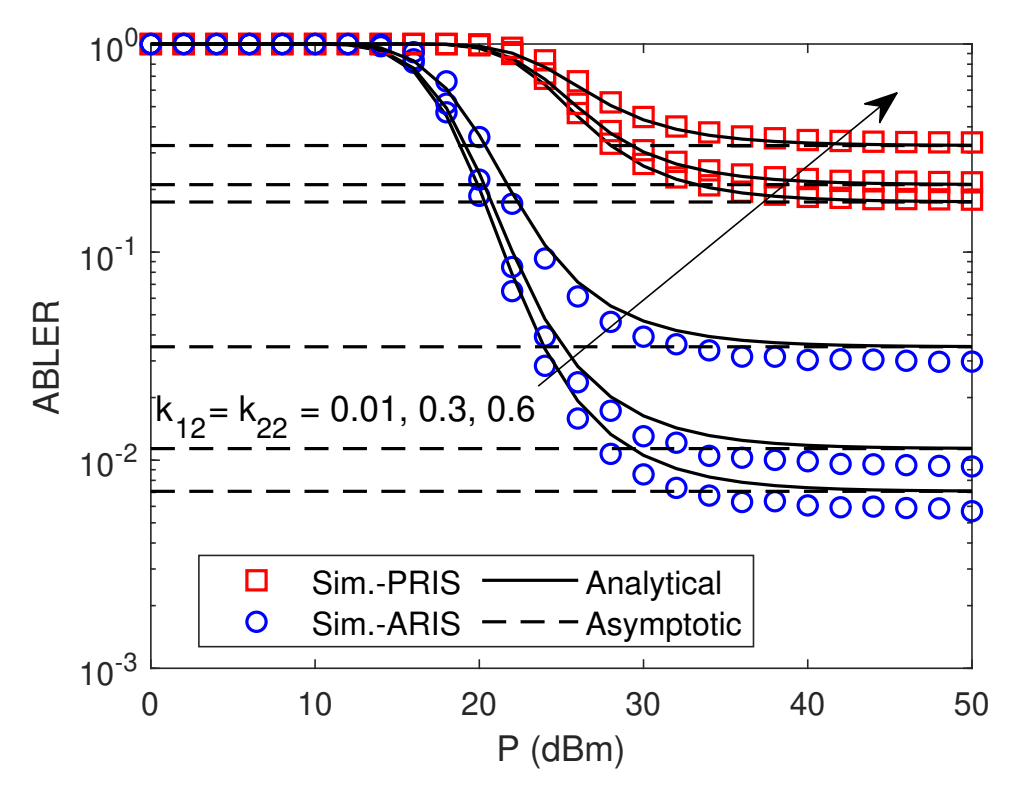


Figure 5.3: Comparison of ABLER vs. transmit power with varying HI parameters.

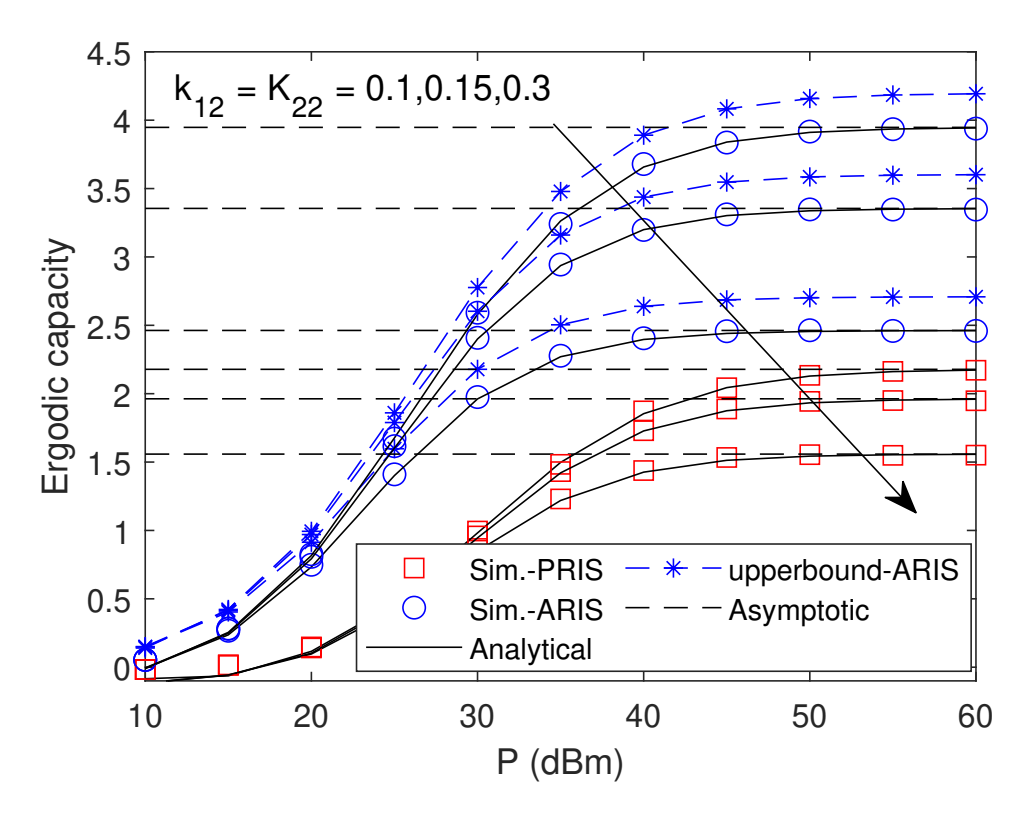


Figure 5.4: Comparison of EC vs. transmit power with varying HI parameters.

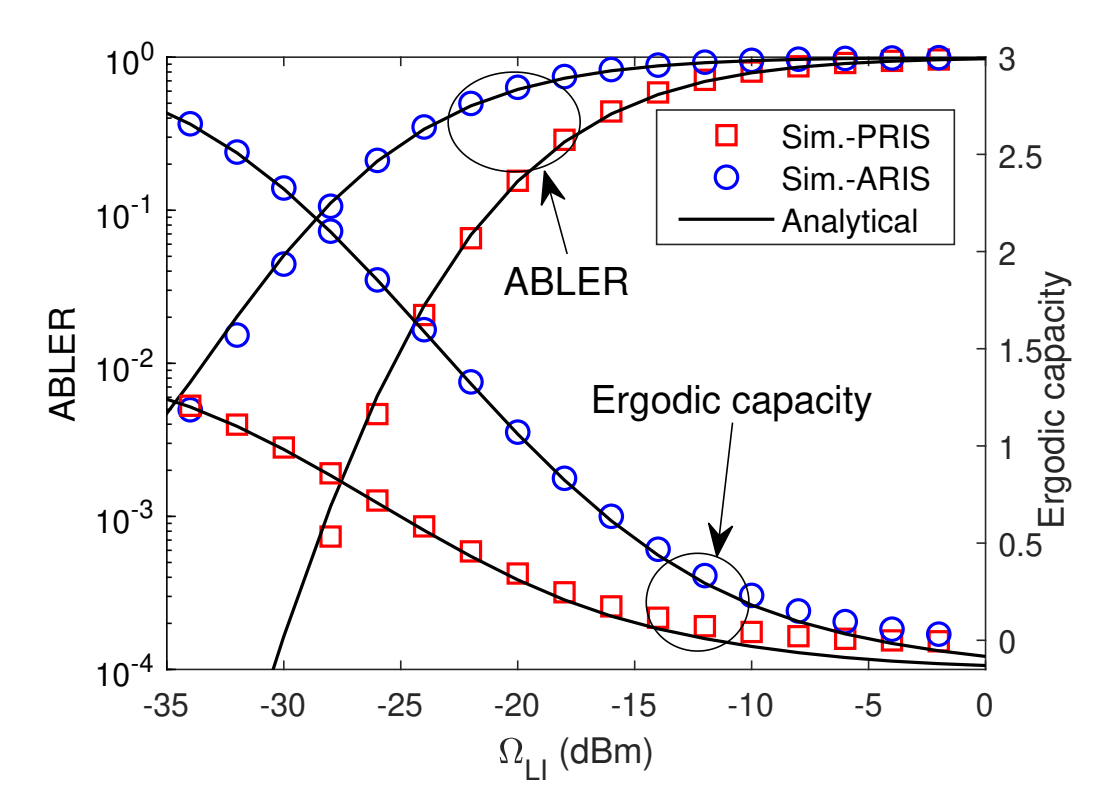


Figure 5.5: Comparison of ABLER and EC vs. LI power.

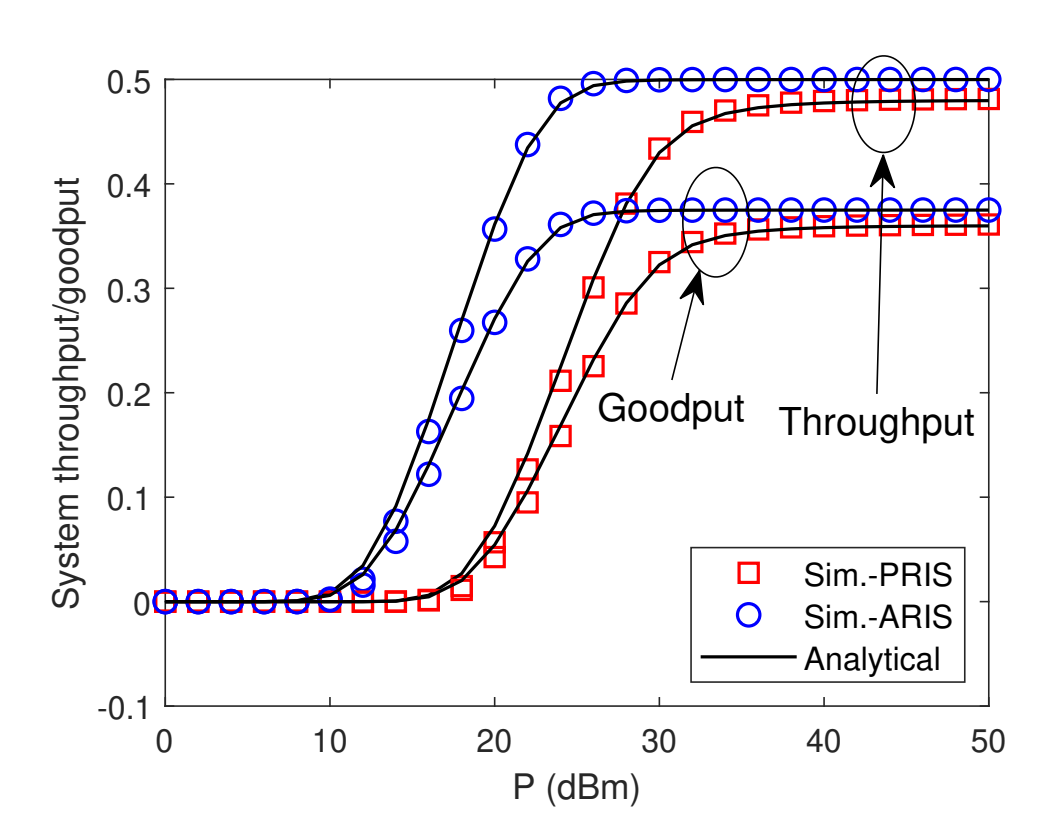


Figure 5.6: Comparison of system throughput/goodput vs. transmit power.

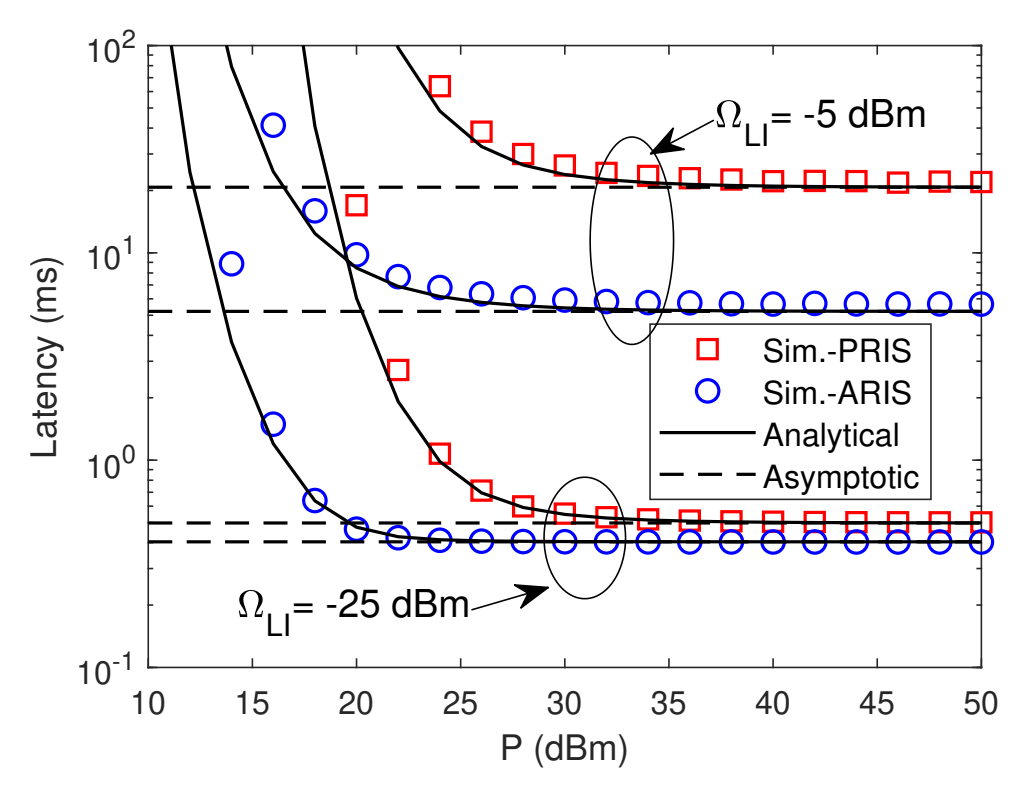


Figure 5.7: Comparison of latency vs. transmit power.

Figure 5.5 simultaneously depicts the comparison of ABLER and EC versus the LI power (Ω_{LI}) at U_2 for a fixed value of P=25 dBm and $k_{12}=k_{22}=0.1$. As seen from Figure 5.5, with an increase of LI, the ABLER increases and converges to unity. Similarly, the EC also starts to decrease as LI increases. This is why ABLER and EC converge to error floor and throughput ceiling at higher P, implying zero slopes for diversity order and multiplexing gains. Furthermore, Figure 5.6 depicts the throughput and goodput curves for U_2 versus P with $k_{12}=k_{22}=0.3$. The analytical results are plotted using (5.14) and are observed to match the simulation results closely. Goodput is usually lower than throughput because it examines the successfully transferred and received information bits, whereas throughput considers the entire bits, including the training bits. Finally, Figure 5.7 plots the latency versus P for ARIS-FDTW and PRIS-FDTW system for $\Omega_{LI}=-5$ and -25 dBm. As shown in Figure 5.7, LI severely impacts system performance under URLLC conditions. Furthermore, for $\Omega_{LI}=-25$ dBm, the ARIS-FDTW and PRIS-FDTW systems meet the criterion of latency (<1ms); however, as the LI increases, i.e., for $\Omega_{LI}=-5$ dBm, the latency of the system increases and the system does not comply with URLLC requirements.

5.4 Summary

This chapter investigated the performance of ARIS-FDTW communication in the face of HIs over cascaded Rician fading channels. System performance was analyzed under FBL regimes. Under the FBL regime, the new analytical expressions for ABLER, EC, system throughput, goodput, and latency were derived for ARIS-FDTW systems under the influence of LI and HIs. We also studied the diversity order and multiplexing gains in the higher transmit power conditions to provide more useful insights. Numerical results revealed the following: 1) our theoretical results corroborate with the simulation ones; 2) LI leads to performance floor at higher P; 3) the performance of ARIS-FDTW system is superior as compared to that of PRIS-FDTW system and conventional FDTW-AF and FDTW-DF relay scenarios under FBL regime; 4) increasing the degree of HI degrades the performance of ARIS-FDTW system.

Chapter 6

Performance of STAR-RIS-assisted Short Packet NOMA Network under Imperfect SIC and CSI

The analysis reported in the literature for STAR-RIS-SP-NOMA is analyzed in terms of ABLER [105, 106, 107], sum-rate maximization [109] with pCSI only. Recently, [108] investigated the SE maximization of STAR-RIS-SP-NOMA with ipCSI. Therefore, it can be observed that most previous works have considered the assumption of pCSI, which is not feasible to acquire in real-world scenarios. Thus, the investigation of performance analysis of STAR-RIS-SP-NOMA with ipCSI is worth investigating. Additionally, the crucial parameters required for analyzing the 6G URLLC use cases, like latency and reliability, are not yet discussed in the existing literature on STAR-RIS-SP-NOMA.

In this chapter, we propose an analytical framework to model the downlink STAR-RIS-SP-NOMA network under ipSIC and ipCSI conditions over the cascaded Nakagami-m fading environment. We have derived the statistical distribution of cascaded Nakagami-m channels by using the Laguerre polynomial series approximation. We derive the closed-form expressions for the ABLER for both users under ipSIC and ipCSI scenarios. The asymptotic analysis of ABLER was also evaluated at a high SNR to gain useful insights. With the help of ABLER, we formulate the overall system throughput and goodput performance under the delay-limited transmission regime. Further, to meet the rigorous requirement of the 6G's IoT network, i.e., ultra-reliability (99.99%) and low latency ($\leq 1ms$), we also formulate the closed-form expression for the latency and reliability in terms of ABLER, which shows the effectiveness of our considered system subjected to ipSIC and ipCSI. Finally, the validity of the closed-form expressions is validated by employing Monte Carlo simulations. Numerical results reveal the superior performance of STAR-RIS-SP-NOMA as compared to STAR-RIS-SP-OMA

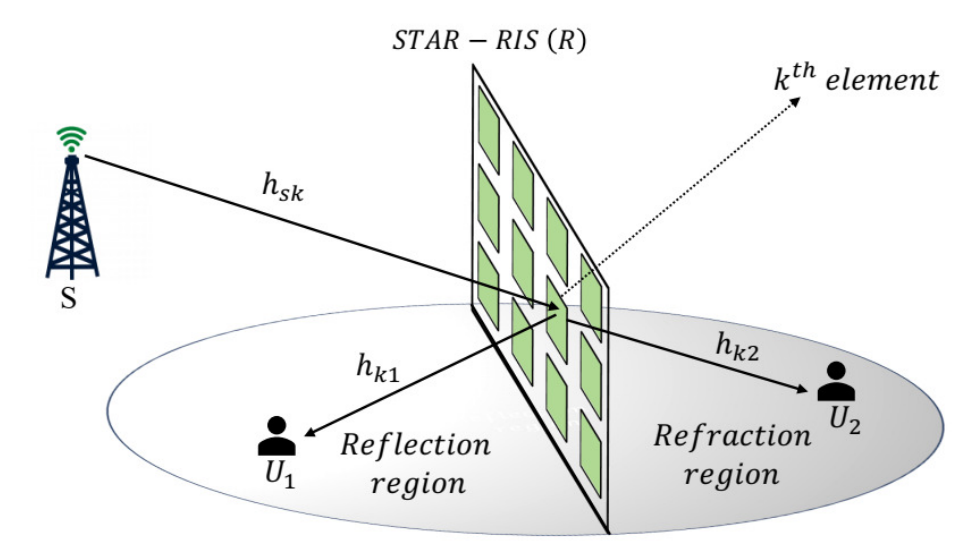


Figure 6.1: STAR-RIS assisted downlink SP-NOMA system.

and the conventional cooperative communication scenarios, such as DF-HD-SP-OMA and fixed-gain AF-HD-SP-OMA schemes. The performance of the STAR-RIS-SP-NOMA is also compared with all three operating protocols of STAR-RIS, and the numerical results reveal that the TS protocol can perform better than the MS and ES protocols. Parameters such as the ipCSI correlation factor, the ipSIC factor, blocklength, and STAR-RIS elements are also examined for their effects on system performance.

System Model 6.1

In the downlink STAR-RIS-SP-NOMA system, as shown in Figure 6.1, a source (S) sends SPs to two paired NOMA users, U_1 (near user) and U_2 (far user) through a microcontroller-enabled STAR-RIS (R) with K passive elements $(k = 1, 2, \dots, K)$ operating in ES mode. We have assumed that the distance between any two elements in STAR-RIS is set to half wavelength to avoid the concept of spatial correlation. In the ES mode, every STAR-RIS element can send some of the incident signals in the desired direction through reflection and some through refraction (transmit), with respective coefficients of η_k^r and η_k^t , with $\eta_k^r + \eta_k^t = 1$, assuming no loss in the STAR-RIS elements. For simplicity, we consider the amplitude, i.e., $\{\eta_k^t\}_{k=1}^K = \eta^t$ and $\{\eta_k^r\}_{k=1}^K = \eta^r$, same value for all the elements. The reflection and refraction coefficient matrices for R are given by $\Phi_r = diag\{\sqrt{\eta^r}e^{-j\theta_1^r}, \sqrt{\eta^r}e^{-j\theta_2^r}, \dots, \sqrt{\eta^r}e^{-j\theta_K^r}\} \in \mathbb{C}^{K \times K}$ and $\Phi_t = diag\{\sqrt{\eta^t}e^{-j\theta_1^t}, \sqrt{\eta^t}e^{-j\theta_2^t}, \dots, \sqrt{\eta^t}e^{-j\theta_K^t}\} \in \mathbb{C}^{K \times K}$. Assuming all devices operate in half-duplex mode, with a single antenna on each node. Furthermore, we assume the direct link between S to U_1 and S to U_2 is blocked.

6.1.1 Channel Model

We denote h_{XY} to be the channel coefficient of the link from the transmitter X to the receiver Y. h_{XY} is complex-valued and is represented in polar form as

$$h_{XY} = d_{XY}^{-\tau/2} |h_{XY}| e^{j \angle h_{XY}}, \tag{6.1}$$

where d_{XY} represents the distance¹ between the node X and Y, τ is the path loss exponent and $|h_{XY}|$ and $\angle h_{XY}$ are the magnitude and phase of h_{XY} . We assume the channel links undergo independent and identically distributed Nakagami-m small-scale fading.

Therefore, the channel between S-R, $R-U_1$ and $R-U_2$ can be expressed as $|h_{sk}| \sim$ Nakagami $(m_{sk}, 1)$, $|h_{k1}| \sim$ Nakagami $(m_{k1}, 1)$ and $|h_{k2}| \sim$ Nakagami $(m_{k2}, 1)$, respectively. Although we consider the ipCSI to be the overall effect of imperfect estimation of the cascaded channel, similar to the assumption made in [57], we proceed under the assumption that the location of S and R is stationary, one can estimate the relative accurate CSI of S-R link by calculating arrival and departure angles. Thus, CSI errors result from errors in channel estimation and limited feedback for the coefficients of the links $R-U_1$ and $R-U_2$. By taking into account the CSI imperfections as discussed in [57, 122, 124], the estimated channel can be written as

$$\widehat{h}_{ki} = \zeta h_{ki} + \sqrt{1 - \zeta^2} \widetilde{h}_{ki}, \tag{6.2}$$

where, \hat{h}_{ki} is the ideal channel, h_{ki} is the estimated channel, \tilde{h}_{ki} is the erroneously estimated channel, having same variance as h_{ki} . $\zeta \in (0,1]$ is the correlation factor used to measure the quality of the channel estimator, $\zeta = 1$ for the best channel estimator, that is, pCSI and $0 < \zeta < 1$ for ipCSI.

6.1.1.1 ES Protocol

Each STAR-RIS element can simultaneously reflect and refract signals for the ES protocol, dividing the total energy into two streams. The value of the reflection and refraction coefficient for the ES protocol lies between $0 \le \eta^t, \eta^r \le 1$.

According to the NOMA strategy, S sends a superimposed signal, $x = \sum_{i=1}^{2} \sqrt{\alpha_i P_s} x_i$, where x_i is the message intended for U_i , complying with $E\{|x_i|^2\} = 1$. Here, P_s represents the transmitted power of the source and α_i is the PA coefficient of U_i , with $i \in \{1, 2\}$ that

¹According to [96], we consider STAR-RIS to be operated in the far field regime; therefore, $d_{sk} = \{d_{sk}\}_{k=1}^{K}$ and $d_{ki} = \{d_{ki}\}_{k=1}^{K}$, e., all the elements of STAR-RIS are considered to be at the same distance from S.

satisfies $\alpha_2 > \alpha_1$ and $\alpha_1 + \alpha_2 = 1$. Therefore, the received signal at U_1 and U_2 can be represented as

$$y_{1} = \underbrace{\sqrt{P_{s}} \left(\zeta \sum_{k=1}^{K} h_{sk} \sqrt{\eta^{r}} e^{-j\theta_{k}^{r}} h_{k1} \right) x}_{\text{desired signal with estimated channel}} + \underbrace{\sqrt{P_{s}(1-\zeta^{2})} \left(\sum_{k=1}^{K} h_{sk} \sqrt{\eta^{r}} e^{-j\theta_{k}^{r}} \tilde{h}_{k1} \right) x}_{\text{signal with erroneous channel}} + n_{1}, \quad (6.3)$$

and

$$y_{2} = \sqrt{P_{s}} \left(\zeta \sum_{k=1}^{K} h_{sk} \sqrt{\eta^{t}} e^{-j\theta_{k}^{t}} h_{k2} \right) x + \sqrt{P_{s}(1-\zeta^{2})} \left(\sum_{k=1}^{K} h_{sk} \sqrt{\eta^{t}} e^{-j\theta_{k}^{t}} \tilde{h}_{k2} \right) x + n_{2},$$
desired signal with estimated channel signal with erroneous channel (6.4)

where the first term is the desired signal, the second term is the error signal due to the ipCSI, and n_1 , n_2 are the AWGN terms with zero mean and variance N_0 .

To maximize the received signal at U_1 and U_2 , we use a coherent combination and the optimal phase shift for the STAR-RIS² is set as $\angle \theta_k^r = -\angle h_{sk} - \angle h_{k1}$ and $\angle \theta_k^t = -\angle h_{sk} - \angle h_{k2}$, [102, 106, 122]. At U_2 , u_2 is decoded directly by considering u_1 as noise. Thus, the received SINR for decoding u_2 at u_2 is given as

$$\Upsilon_2 = \frac{\rho \zeta^2 \eta^t \alpha_2 X_2^2}{\rho \zeta^2 \eta^t \alpha_1 X_2^2 + \rho (1 - \zeta^2) \eta^t Y_t^2 + 1},\tag{6.5}$$

where $\rho = P_s/N_0$, is the transmit SNR, and $X_2 = (d_{sk}d_{k2})^{-\tau/2}(\sum_{k=1}^K |h_{sk}h_{k2}|)$ and $Y_t = (d_{k2})^{-\tau/2}(\sum_{k=1}^K |h_{sk}e^{j\theta_k^t}|)$. Conversely, by using SIC, U_1 decodes its own signal, x_1 by first decoding x_2 and treating x_1 as interference. Therefore, the instantaneous SINR of decoding x_2 at U_1 can be written as

$$\Upsilon_{1\to 2} = \frac{\rho \zeta^2 \eta^r \alpha_2 X_1^2}{\rho \zeta^2 \eta^r \alpha_1 X_1^2 + \rho (1 - \zeta^2) \eta^r Y_2^2 + 1}.$$
(6.6)

Practically, SIC implementation may lead to decoding errors, also known as ipSIC. Therefore, if x_2 is successfully decoded and removed, then the instantaneous SINR for decoding x_1 at U_1 is

$$\Upsilon_1 = \frac{\rho \zeta^2 \eta^r \alpha_1 X_1^2}{\rho \zeta^2 \eta^r \alpha_2 \psi X_1^2 + \rho (1 - \zeta^2) \eta^r Y_r^2 + 1},\tag{6.7}$$

²We apply an independent phase-shift model for reflection and transmission coefficients to establish the maximum performance enhancement of the STAR-RIS. In passive STAR-RIS, linked phase-shift coefficients may reduce performance.

where $X_1 = (d_{sk}d_{k1})^{-\tau/2} \sum_{k=1}^{K} |h_{sk}h_{k1}|$, $Y_r = (d_{k1})^{-\tau/2} (\sum_{k=1}^{K} |h_{sk}e^{j\theta_k^r}|)$. and ψ is the ipSIC factor, $\psi = 0$ is the case of pSIC and $0 < \psi < 1$ refers to ipSIC.

6.1.1.2 MS and TS Protocol

In the case of the MS protocol, the STAR-RIS elements are divided into two groups: one group utilizes the STAR-RIS elements as perfect reflectors, while the other group uses them to transmit the signals entirely. Therefore, we assume that K_t elements are used for the transmitting (refracting) links and K_r elements are used for the reflecting links, i.e., $K_t + K_r = K$. Therefore, for the MS protocol $\eta^r = 1$ and $\eta^t = 0$ for the reflective link and $\eta^r = 0$ and $\eta^t = 1$ for the transmitting link.

In the TS protocol, STAR-RIS functions in distinct coherence times in full reflection and full refraction mode during the T and R periods. During the T period, all STAR-RIS elements only refract signals ($\eta^t = 1$ and $\eta^r = 0$), whereas, during the R period, all STAR-RIS elements operate as the full reflection mode ($\eta^r = 1$ and $\eta^t = 0$).

6.1.2 STAR-RIS assisted SP-OMA

We compare STAR-RIS-SP-NOMA to STAR-RIS-SP-OMA to illustrate the performance benefits of STAR-RIS-SP-NOMA. We consider the FDMA scheme to transmit signals of U_1 and U_2 in two separate bandwidth resources. According to the preceding subsection, SINR at $U_i, i \in \{1, 2\}$ is provided by

$$\Upsilon_i^{OMA} = \frac{\rho \zeta^2 \eta^j X_i^2}{d_{ki}^{-\tau} \rho (1 - \zeta^2) \eta^j Y_i^2 + 1},\tag{6.8}$$

Note that, for i = 1, j = r and for i = 2, j = t.

6.1.3 Statistical Distribution

Computation of CDF and PDF of $X_i = (\sum_{k=1}^K |h_{sk}h_{ki}|), i \in \{1, 2\}$ is not straightforward. Let $\mathcal{X}_i = |h_{sk}h_{ki}|$, therefore the mean and variance of \mathcal{X}_i can be expressed as

$$\mu_{\mathcal{X}_i} = \mathbb{E}\{\mathcal{X}_i\} = \frac{\Gamma(m_{sk} + \frac{1}{2})\Gamma(m_{ki} + \frac{1}{2})}{\Gamma(m_{sk})\Gamma(m_{ki})\sqrt{m_{sk}m_{ki}}},\tag{6.9}$$

and

$$\Omega_{\mathcal{X}_i} = Var(\mathcal{X}_i) = 1 - \frac{1}{m_{sk}m_{ki}} \left[\frac{\Gamma(m_{sk} + \frac{1}{2})\Gamma(m_{ki} + \frac{1}{2})}{\Gamma(m_{sk})\Gamma(m_{ki})} \right]^2, \tag{6.10}$$

By using Laguerre polynomial series [118, Eq. (2.76)], we can get the PDF and CDF of

 X_i as

$$f_{X_i}(x) = \frac{x^{\varphi_i} e^{-\frac{x}{\varphi_i}}}{\phi_i^{\varphi_i + 1} \Gamma(\varphi_i + 1)},\tag{6.11}$$

and

$$\mathcal{F}_{X_i}(x) = \frac{\Upsilon\left(\varphi_i + 1, \frac{x}{\phi_i}\right)}{\Gamma(\varphi_i + 1)},\tag{6.12}$$

where, $\varphi_i = \frac{K\mu_{\mathcal{X}_i}^2 - \Omega_{\mathcal{X}_i}}{\Omega_{\mathcal{X}_i}}$ and $\phi_i = \frac{\Omega_{\mathcal{X}_i}}{\mu_{\mathcal{X}_i}}$. The PDF and CDF of $Y_j = (\sum_{k=1}^K |h_{sk}e^{j\theta_k^j}|), j \in \{r, t\}$ can be approximated with the help of causal CLT as $Y_j \sim \mathcal{C}(0, \Omega_j)$, where $\Omega_j = Kd_{sk}^{-\tau}$ [76, 77]. Therefore, the PDF and CDF of Y_j^2 can be expressed as

$$f_{Y_j^2}(y) = \frac{1}{\Omega_j} \exp\left(-\frac{y}{\Omega_j}\right), \quad \mathcal{F}_{Y_j^2}(y) = 1 - \exp\left(-\frac{y}{\Omega_j}\right).$$
 (6.13)

6.2 Performance Evaluation

This section discusses the initial stages of calculating the ABLER. We then determine the ABLER expressions for U_1 and U_2 . Asymptotic expressions of ABLER are obtained to acquire further insights. Then, based on the ABLER expression, we deduce the expressions for the system's throughput, goodput, latency, and reliability.

6.2.1 ABLER Preliminaries

Shannon's theorem, built on the assumption of IBL, is no longer valid in FBL analysis [46]. In FBL transmission, ABLER is computed to analyze the system performance [102, 106, 103, 104]. Let $\mathbb{L} = \ell_d + \ell_t$, where \mathbb{L} , ℓ_d and ℓ_t are the total blocklength, blocklength for data and blocklength for training, respectively. Here, we define the N_i and ℓ_d as the number of information bits and blocklength for U_i , respectively, $i \in \{1, 2\}$. Therefore, the maximum achievable rate at U_i can be written as $r_i = \frac{N_i}{\ell_d}$. Therefore, the ABLER can be obtained by averaging Ξ_i over SINR, as mentioned in section 4.4.1.

$$\overline{\Xi}_i \approx \vartheta_i \int_{\nu_i}^{\mu_i} \mathcal{F}_{\Upsilon_i}(x) dx.$$
(6.14)

where, $\mathcal{F}_{\Upsilon_i}(x)$ is the CDF of Υ_i , $\vartheta_i = [2\pi(2^{2r_i} - 1)/\ell_d]^{-1/2}$, $o_i = 2^{r_i} - 1$, $\nu_i = o_i - 1/(2\vartheta_i)$ and $\mu_i = o_i + 1/(2\vartheta_i)$.

6.2.2 Calculation of ABLER at U_1

By using the similar steps mentioned in Appendix A.5, the ABLER at U_1 for the STAR-RIS-SP-NOMA network with ipCSI and ipSIC can be expressed as

$$\overline{\Xi}_1^{ipCSI} = \overline{\Xi}_{1\to 2} + (1 - \overline{\Xi}_{1\to 2})\overline{\Xi}_1 \tag{6.15}$$

where, $\overline{\Xi}_{1\to 2}$ and $\overline{\Xi}_1$ are the ABLER for decoding x_2 and x_1 at U_1 respectively and can be written as

$$\overline{\Xi}_{1} \approx \vartheta_{1} \left(\frac{\mu_{1} - \nu_{1}}{2} \right) \sum_{m=1}^{M} \frac{\pi}{M} \sqrt{1 - x_{m}^{2}} \left[\sum_{u=1}^{U} H_{u} \frac{1}{\Gamma(\varphi_{1} + 1)} \Upsilon\left(\varphi_{1} + 1, \frac{\sqrt{\Lambda_{1}(b_{r}x_{u} + 1)}}{\varphi_{1}}\right) \right], \tag{6.16}$$

$$\overline{\Xi}_{1 \to 2} \approx \vartheta_{1} \left(\frac{\mu_{1} - \nu_{1}}{2} \right) \sum_{m=1}^{M} \frac{\pi}{M} \sqrt{1 - x_{m}^{2}} \left[\sum_{u=1}^{U} H_{u} \frac{1}{\Gamma(\varphi_{1} + 1)} \times \right]$$

$$\Upsilon\left(\varphi_{1} + 1, \frac{\sqrt{\Lambda_{1 \to 2}(b_{r}x_{u} + 1)}}{\varphi_{1}} \right) ,\tag{6.17}$$

where, $x_m = cos\left(\frac{2m-1}{2M}\pi\right)$, $\Lambda_1 = \frac{(d_{sk}d_{k1})^{\tau}z_1}{\rho\zeta^2\eta^r(\alpha_1-\psi z_1\alpha_2)}$, $\Lambda_{1\to 2} = \frac{(d_{sk}d_{k1})^{\tau}z_1}{\rho\zeta^2\eta^r(\alpha_2-z_1\alpha_1)}$, $z_1 = \left(\frac{\mu_1-\nu_1}{2}\right)x_m + \left(\frac{\mu_1+\nu_1}{2}\right)$, $b_r = \rho d_{k1}^{-\tau}(1-\zeta^2)\eta^r\Omega_r$ and M is the complexity trade-off factor. x_u is the u-th zero point (abscissa) of Laguerre polynomial, $L_U(x) = \frac{e^x}{U!}\frac{d}{dx^u}\left(x^Ue^{-x}\right)$, u-th weight can be expressed as $H_U = \frac{\left(U!\right)^2x_u}{\left[L_{U+1}(x_u)\right]^2}$ and U is the Laguerre tradeoff factor. Note that the (6.16) is valid only when $\alpha_1 - \psi z_m \alpha_2 > 0$, otherwise $\overline{\Xi}_1 = 1$ and (6.17) is valid for $\alpha_2 - \psi z_m \alpha_1 > 0$, otherwise $\overline{\Xi}_{1\to 2} = 1$. The value of the $\overline{\Xi}_1^{ipCSI}$ for different ipSIC can be obtained by varying $0 < \psi < 1$ in (6.16). The value of $\overline{\Xi}_1^{ipCSI}$ with pSIC can be obtained by putting $\psi = 0$ in (6.16).

The ABLER for the case of pCSI and ipSIC can be obtained by putting $\zeta=1$ in the (6.6) and (6.7). Therefore the overall ABLER for STAR-RIS-SP-NOMA with pCSI can be expressed as $\overline{\Xi}_1^{pCSI}=\overline{\Xi}_{1\to 2}'+(1-\overline{\Xi}_{1\to 2}')\overline{\Xi}_1'$. By using (6.12) and applying the GCQ method, $\overline{\Xi}_1'$ can be written as

$$\overline{\Xi}_{1}' \approx \vartheta_{1} \left(\frac{\mu_{1} - \nu_{1}}{2} \right) \sum_{m=1}^{M} \frac{\pi}{M} \sqrt{1 - x_{m}^{2}} \left[\frac{1}{\Gamma(\varphi_{1} + 1)} \Upsilon\left(\varphi_{1} + 1, \frac{\sqrt{\Lambda_{1}}}{\phi_{1}}\right) \right], \tag{6.18}$$

Similarly to (6.18), the expression for $\overline{\Xi}'_{1\to 2}$ can be obtained by changing Λ_1 to $\Lambda_{1\to 2}$ in (6.18).

6.2.3 Calculation of ABLER at U_2

The ABLER at U_2 for the STAR-RIS-SP-NOMA with ipCSI can be approximated as

$$\overline{\Xi}_{2}^{ipCSI} \approx \vartheta_{2} \left(\frac{\mu_{2} - \nu_{2}}{2} \right) \sum_{m=1}^{M} \frac{\pi}{M} \sqrt{1 - x_{m}^{2}} \left[\sum_{u=1}^{U} H_{u} \frac{1}{\Gamma(\varphi_{2} + 1)} \Upsilon\left(\varphi_{2} + 1, \frac{\sqrt{\Lambda_{2}(b_{t}x_{u} + 1)}}{\phi_{2}}\right) \right], \tag{6.19}$$

where, $\Lambda_2 = \frac{(d_{sk}d_{k2})^{\tau}z_2}{\rho\zeta^2\eta^t(\alpha_2-z_2\alpha_1)}$, $z_2 = \left(\frac{\mu_2-\nu_2}{2}\right)x_m + \left(\frac{\mu_2+\nu_2}{2}\right)$ and $b_t = \rho d_{k2}^{-\tau}(1-\zeta^2)\eta^t\Omega_t$. Note that the above expression of ABLER is valid only when $\alpha_2 - z_2\alpha_1 > 0$, otherwise $\overline{\Xi}_2^{ipCSI} = 1$. The ABLER for the case of pCSI can be obtained by putting $\zeta = 1$ in the (6.5). Therefore, the ABLER for the case of STAR-RIS-SP-NOMA with pCSI can be expressed as

$$\overline{\Xi}_{2}^{pCSI} \approx \vartheta_{2} \left(\frac{\mu_{2} - \nu_{2}}{2} \right) \sum_{m=1}^{M} \frac{\pi}{M} \sqrt{1 - x_{m}^{2}} \left[\frac{1}{\Gamma(\varphi_{2} + 1)} \Upsilon\left(\varphi_{2} + 1, \frac{\sqrt{\Lambda_{2}}}{\phi_{2}}\right) \right], \tag{6.20}$$

6.2.4 Asymptotic ABLER Analysis

This section presents the asymptotic ABLER analysis for U_1 and U_2 , which provides further insights for the STAR-RIS-SP-NOMA with ipCSI and ipSIC at a high transmit SNR regime.

6.2.4.1 Asymptotic ABLER at U_1

Assuming $\rho \to \infty$, the asymptotic ABLER of U_1 with ipCSI and ipSIC can be approximated as $\overline{\Xi}_1^{ipCSI,\infty} = \overline{\Xi}_{1\to 2}^{\infty} + (1-\overline{\Xi}_{1\to 2})\overline{\Xi}_1^{\infty}$, where $\overline{\Xi}_1^{\infty}$ can be written as

$$\overline{\Xi}_{1}^{\infty} \approx \vartheta_{1} \left(\frac{\mu_{1} - \nu_{1}}{2} \right) \sum_{m=1}^{M} \frac{\pi}{M} \sqrt{1 - x_{m}^{2}} \left[\sum_{u=1}^{U} H_{u} \frac{1}{\Gamma(\varphi_{1} + 1)} \times \left(\varphi_{1} + 1, \frac{\sqrt{\Lambda_{1}(1 - \zeta^{2})\eta^{r}\Omega_{r}x_{u}}}{\sqrt{d_{k_{1}}^{\tau}\zeta^{2}\eta^{r}}\phi_{1}} \right) \right],$$
(6.21)

Similar to (6.21), the expression for $\overline{\Xi}_{1\to 2}^{\infty}$ can be obtained by changing Λ_1 to $\Lambda_{1\to 2}$ in (6.21). Furthermore, the asymptotic ABLER at U_1 with pCSI can be obtained as $\overline{\Xi}_1^{pCSI,\infty} = \overline{\Xi}_{1\to 2}^{'\infty} + (1 - \overline{\Xi}_{1\to 2}^{'\infty})\overline{\Xi}_1^{'\infty}$. By using [117, Eq. (8.354.1)] the expression for $\overline{\Xi}_1^{'\infty}$ can be approximated as

$$\overline{\Xi}_{1}^{'\infty} \approx \vartheta_{1} \left(\frac{\mu_{1} - \nu_{1}}{2} \right) \sum_{m=1}^{M} \frac{\pi}{M} \sqrt{1 - x_{m}^{2}} \left[\frac{1}{(\varphi_{1} + 1)\Gamma(\varphi_{1} + 1)} \left(\frac{\Lambda_{1}}{\phi_{1}^{2}} \right)^{\frac{\varphi_{1} + 1}{2}} \right], \tag{6.22}$$

Similar to (6.22), the expression of $\overline{\Xi}_{1\to 2}^{'\infty}$ can obtained by changing Λ_1 to $\Lambda_{1\to 2}$ in (6.22).

6.2.4.2 Asymptotic ABLER at U_2

Assuming $\rho \to \infty$, the asymptotic ABLER of U_2 with ipCSI can be approximated as

$$\overline{\Xi}_{2}^{ipCSI,\infty} \approx \vartheta_{2} \left(\frac{\mu_{2} - \nu_{2}}{2}\right) \sum_{m=1}^{M} \frac{\pi}{M} \sqrt{1 - x_{m}^{2}} \left[\sum_{u=1}^{U} H_{u} \frac{1}{\Gamma(\varphi_{2} + 1)} \times \left(6.23\right)\right]$$

$$\Upsilon\left(\varphi_{2} + 1, \frac{\sqrt{(d_{sk}d_{k2})^{\tau}(1 - \zeta^{2})\eta^{t}\Omega_{t}z_{2}x_{u}}}{\sqrt{d_{k2}^{\tau}\zeta^{2}\eta^{t}(\alpha_{2} - z_{2}\alpha_{1})}\phi_{2}}\right).$$

Similarly to (6.22), the asymptotic ABLER of U_2 with pCSI can be expressed a

$$\overline{\Xi}_{2}^{pCSI,\infty} \approx \vartheta_2 \left(\frac{\mu_2 - \nu_2}{2}\right) \sum_{m=1}^{M} \frac{\pi}{M} \sqrt{1 - x_m^2} \left[\frac{1}{(\varphi_2 + 1)\Gamma(\varphi_2 + 1)} \left(\frac{\Lambda_2}{\phi_2^2}\right)^{\frac{\varphi_2 + 1}{2}} \right]. \tag{6.24}$$

Remark 6.1 We can observe that the asymptotic ABLER of U_1 and U_2 with ipCSI converges to an error floor. Thus, the diversity order of U_1 and U_2 with ipCSI is equivalent to zero because of the residual error that arises from ipCSI. The diversity order for the ABLER of U_1 and U_2 with pCSI is proportional to $(1/\rho)^{(\varphi_1+1)/2}$ and $(1/\rho)^{(\varphi_2+1)/2}$ respectively.

6.2.5 System Throughput and Goodput

Throughput is a performance parameter used to evaluate communication system efficacy at a constant channel coding rate, whereas goodput is defined as the the number of information bits reliably delivered in a specific time. Therefore, the total system throughput and goodput (in bits/s/Hz) can be expressed similarly to section 4.4.5 as

$$\mathcal{T}^{[pCSI,ipCSI]} = \sum_{i=1}^{2} \left(1 - \overline{\Xi}_{i}^{[pCSI,ipCSI]} \right) r_{i}, \quad \mathcal{G}^{[pCSI,ipCSI]} = \left(1 - \frac{\ell_{t}}{\mathcal{L}} \right) \mathcal{T}^{[pCSI,ipCSI]}. \tag{6.25}$$

6.2.6 Latency and Reliability

Latency in the physical layer is measured as the typical time for a packet to be sent and decoded by the radio interface. Meanwhile, reliability is the likelihood of successfully transmitting N_i bits of information across a certain channel quality in the allotted time on the user plane. We assume the fixed coherence time block, T (in ms), for each channel use. Therefore, mathematically the latency, \mathcal{L} (in ms) and the reliability, \mathcal{R} (in%) for

 $U_i, i \in \{1, 2\}$ can be evaluated similar to section 4.4.6, respectively as

$$\mathbb{L}_{i}^{[pCSI,ipCSI]} = \frac{\ell_{d}T}{\left(1 - \overline{\Xi}_{i}^{[pCSI,ipCSI]}\right)}, \quad \mathbb{R}_{i}^{[pCSI,ipCSI]} = \left(1 - \overline{\Xi}_{i}^{[pCSI,ipCSI]}\right) \times 100. \quad (6.26)$$

Table 6.1: Simulation Parameters for STAR-RIS-SP-NOMA.

Parameters	Values
STAR-RIS elements, (K)	15
Bandwidth, (BW)	10 MHz
Number of information bits for U_2 , (N_2)	150
Number of information bits for U_1 , (N_1)	200
Distance from S to R, (d_{sk}) , (in meters)	15
Distance from R to U_1 , (d_{k1}) (in meters)	10
Distance from R to U_2 , (d_{k2}) (in meters)	20
Blocklength for data, (ℓ_d)	500
Blocklength for training, (ℓ_t)	100
Coherence time for each channel use, (T) (in ms)	0.001
Pathloss exponent, (τ)	2.5
Iterations	10^{6}
Power allocation coefficient, (α_1) and (α_2)	0.3 and 0.7
Reflection (η^r) and Refraction (η^t) coefficient	0.7 and 0.3
Complexity trade-off factor, (M) and (U)	50 and 300

6.3 Simulation Results and Discussion

This section presents and validates the findings of theoretical analyses and Monte Carlo simulations (Sim.) that assess the STAR-RIS-SP-NOMA communication system's performance in terms of ABLER, system throughput, goodput, latency, and reliability. Additionally, the asymptotic ABLER and the impact of critical factors on the system performance are examined to offer useful design insights. The noise power (in dBm) is set as $\sigma^2 = -174 + 10 \log_{10}(BW) + NF$, where, BW is 10 MHz and NF is 10 dB. The values of η^r and η^t are taken according to [90]. The value of the path-loss exponent, τ , and the range of distances, d_{sk} , d_{k1} and d_{k2} are taken in accordance to [91, 105, 106]. We have assumed the Nakagami-m fading parameter, $m_{sk} = m_{k1} = m_{k2} = m$. Unless otherwise stated, all the parameters are set accordingly to Table 6.1. In Figure 6.2, the comparison of ABLER for STAR-RIS-SP-NOMA with STAR-RIS-SP-OMA system is plotted for $\zeta = 1$, $\psi = 0.2$ and m = 0.8. As can be observed, the STAR-RIS-SP-NOMA system performs better than the STAR-RIS-SP-OMA, DF-HD-SP-OMA, and AF-HD-SP-OMA scenarios. The analytical results match the simulated ones.

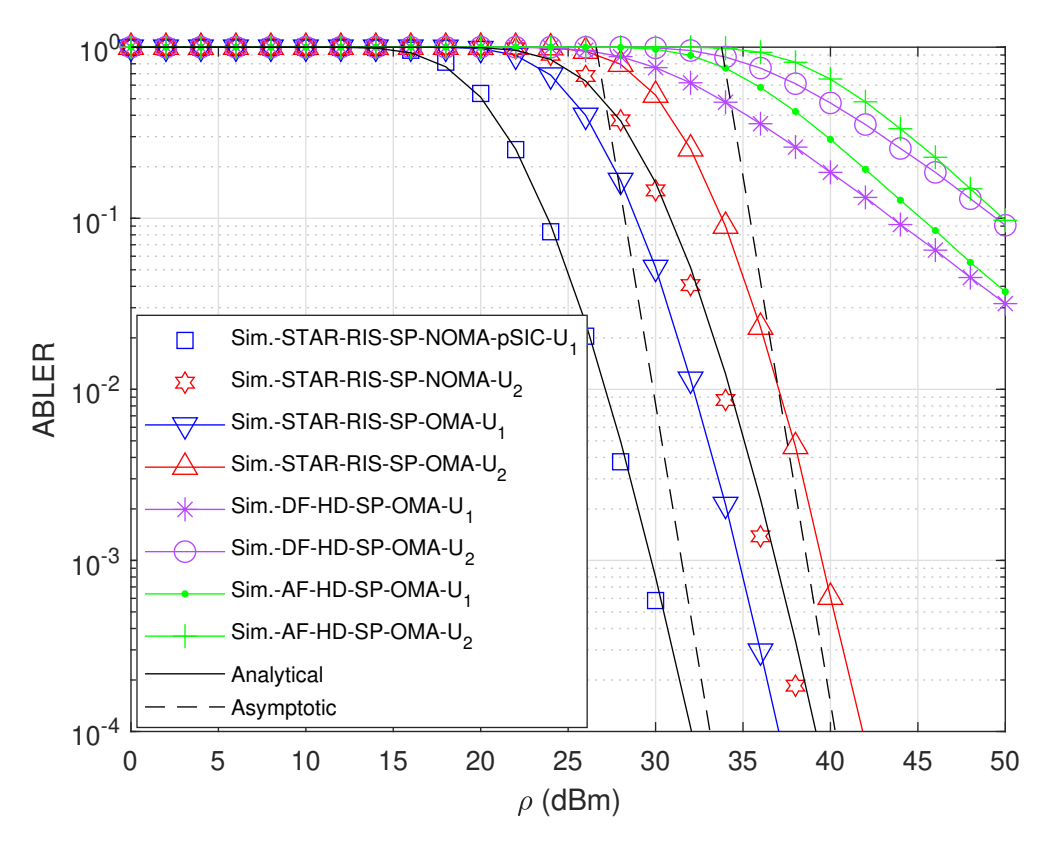


Figure 6.2: ABLER vs. transmit SNR.

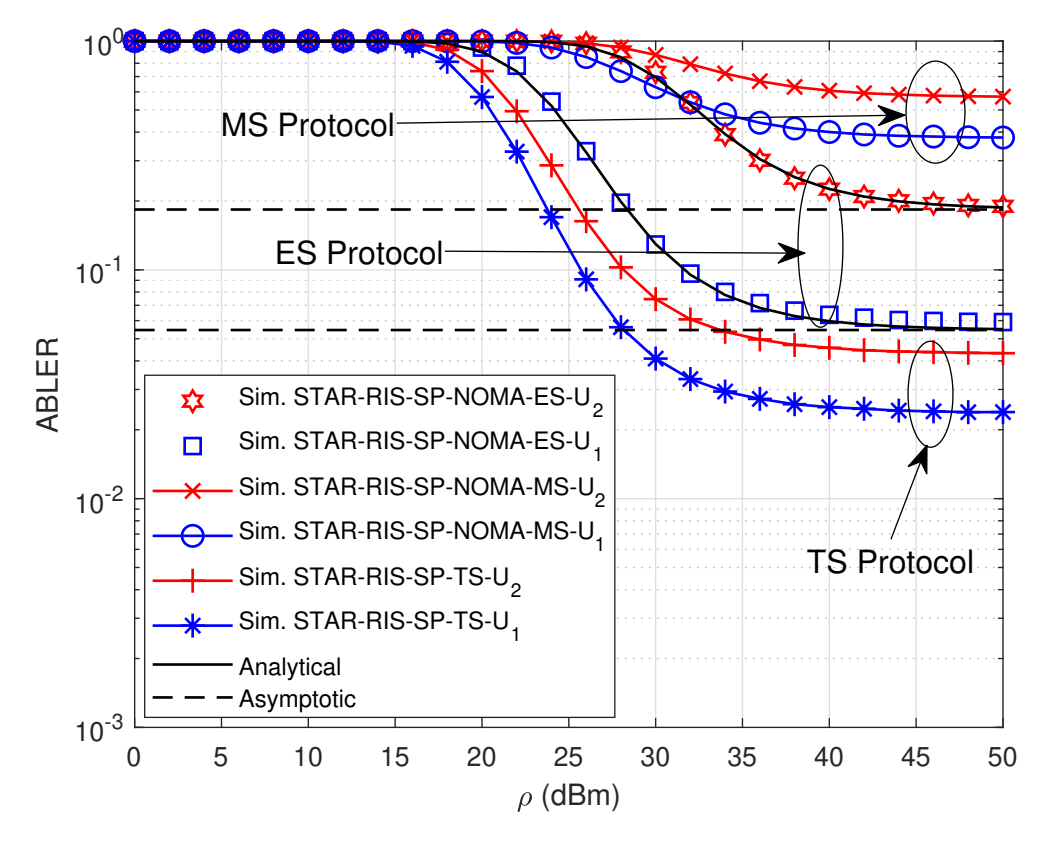


Figure 6.3: Comparison of ABLER vs. transmit SNR for all STAR-RIS protocols.

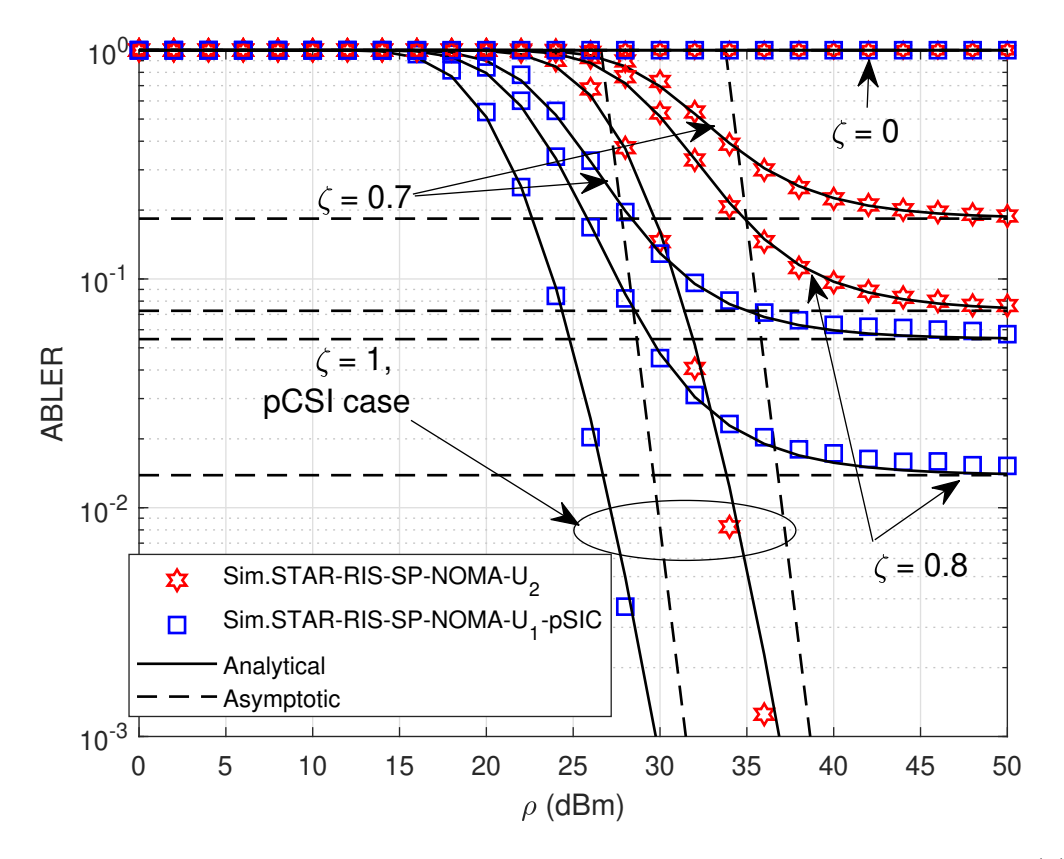


Figure 6.4: Comparison of ABLER vs. transmit SNR for varying ipCSI factor (ζ).

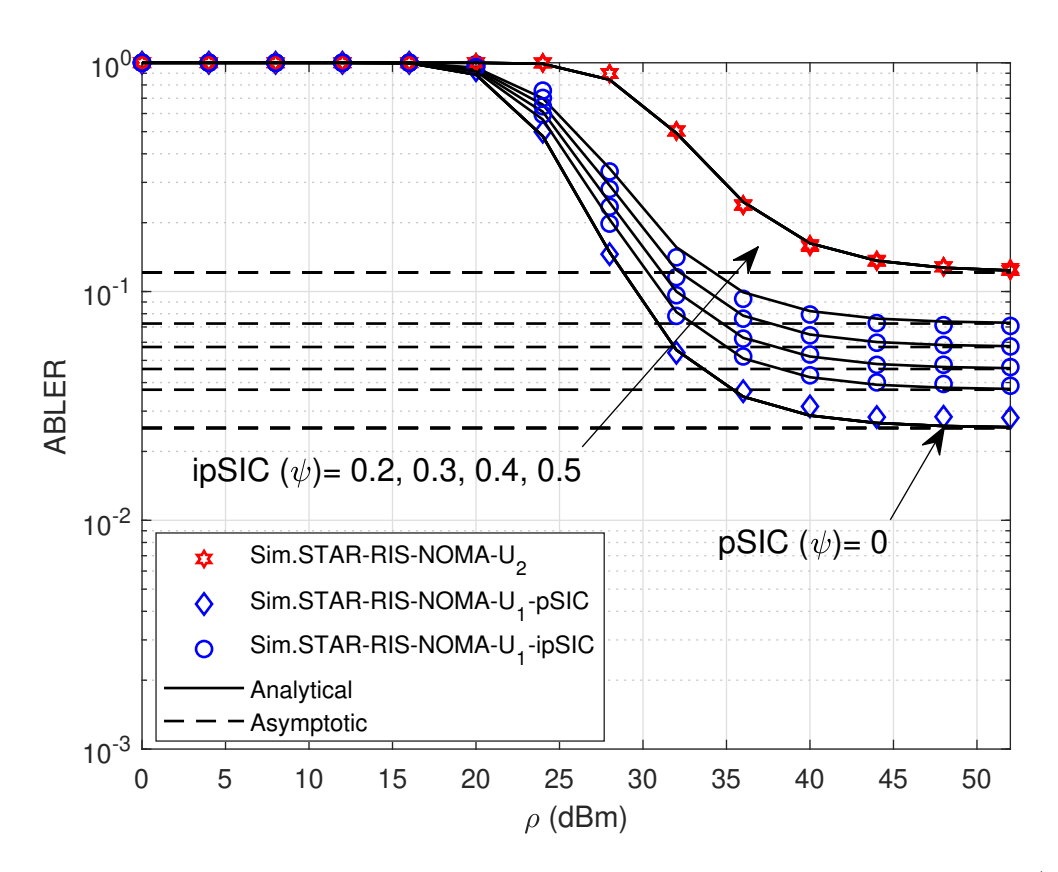


Figure 6.5: Comparison of ABLER vs. transmit SNR for varying ipSIC factor (ψ) .

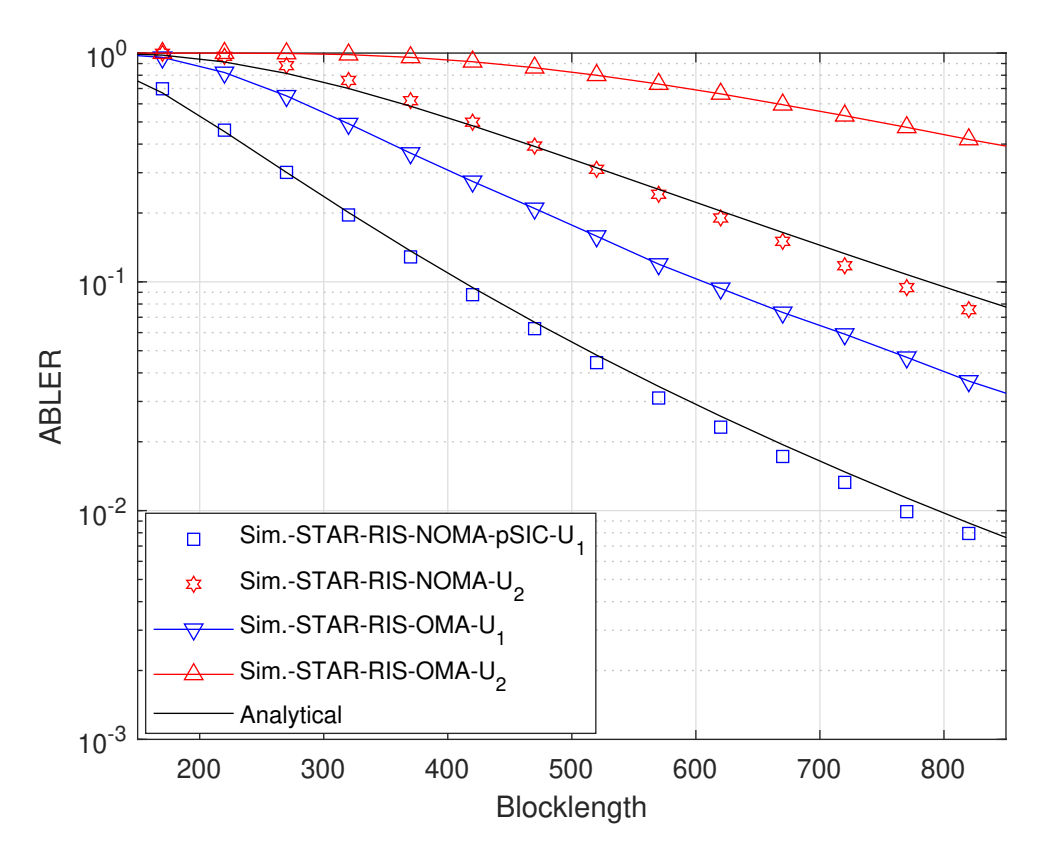


Figure 6.6: ABLER vs. blocklength.

In Figure 6.3, the ABLER versus transmit SNR is plotted for the MS, ES, and TS protocols with $\zeta = 0.7$, $\psi = 0.2$, and m = 0.8. It can be observed that the TS protocol performs better than the MS and ES protocols. This is because, in the TS protocol, all STAR-RIS elements transmit or reflect fully in the T or R- period. The ES protocol performs better than the MS protocol because, while serving two users in the same resource block, the ES protocol utilizes all the STAR-RIS elements to serve both users. In Figure 6.4, to show the effect of ipCSI, the value of the CSI correlation factor is varied as $\zeta = 0, 0.7.0.8, 1$ with a constant ipSIC factor of $\psi = 0.1$. For $\zeta = 0$, the channel is totally erroneous. So, the system exhibits a maximum ABLER of 1, i.e., no packet is recovered successfully at the receiver. For $0 < \zeta < 1$, the ABLER starts to decrease, and for $\zeta = 1$ (the case of pCSI), the system achieves the best ABLER performance. The analytical results corroborate with the simulations. Additionally, at high SNR, the asymptotic results for ipCSI approach the error floor, consistent with Remark 6.1. In Figure 6.5, the effect of ipSIC is shown on the STAR-RIS-SP-NOMA system with $\zeta = 0.8, \psi = 0, 0.2, 0.3, 0.4, 0.5$ and m = 0.8. One can observe from the figure that, increasing the ipSIC factor from $\psi = 0, 0.2, 0.3, 0.4, 0.5,$ the ABLER starts increasing, and performance degrades. For $\psi = 0$, (pSIC case), the ABLER of U_1 is lowest, and with the increasing ψ , the value of ABLER starts increasing.

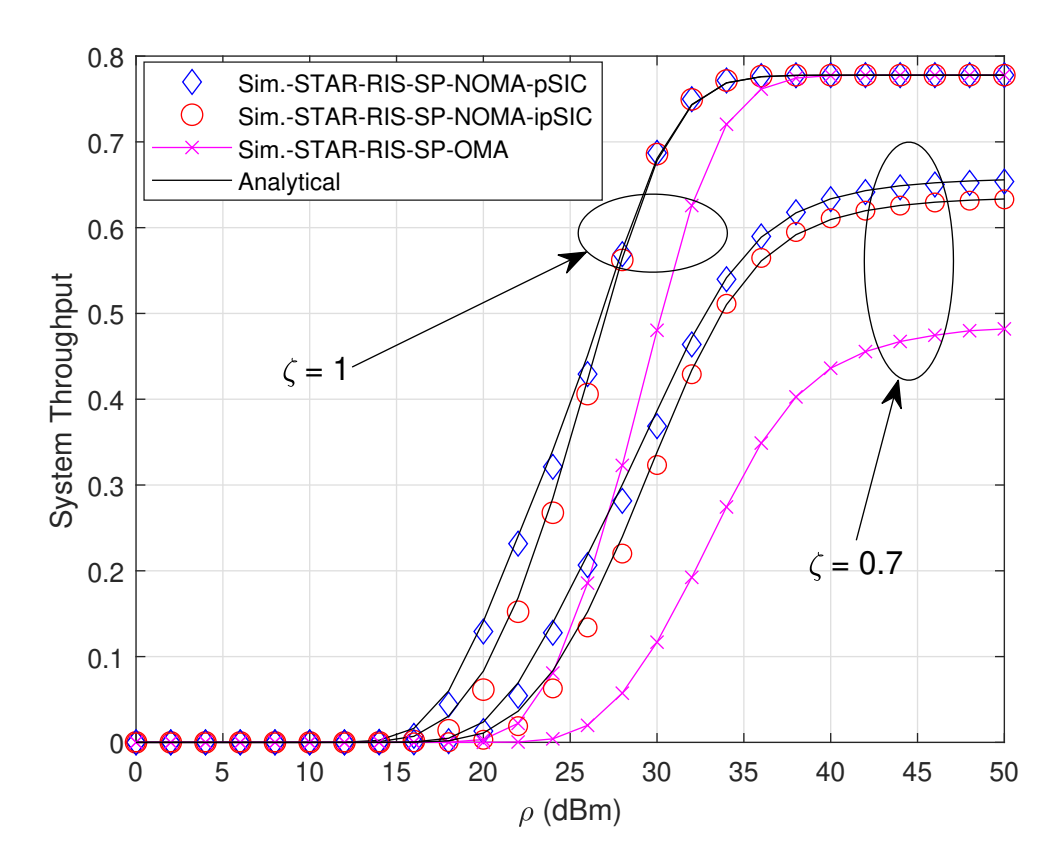


Figure 6.7: System throughput vs. transmit SNR.

At high transmit SNR, the ABLER curves reach an error floor, verified by asymptotic results. The analytical curves match the simulation, which reveals the tightness of the analytical results.

In Figure 6.6, the ABLER is plotted against blocklength, ℓ_d , for the STAR-RIS-SP-NOMA and STAR-RIS-SP-OMA for $\rho=20{\rm dBm}$, $\zeta=0.8$, and $\psi=0$. It can be observed that the STAR-RIS-SP-NOMA system provides better reliability than the STAR-RIS-SP-OMA. From the figure, it can be observed that the reliability can be increased by increasing the blocklength. Conversely, when the amount of information bits are fixed, the transmission rate will decrease due to an increase in block length. In Figure 6.7, system throughput is plotted versus transmit SNR for $\zeta=0.7,1, \psi=0.3$ and m=0.8. The system throughput is plotted using (6.25). As can be observed, the STAR-RIS-SP-NOMA system with pCSI and ipSIC reaches a higher throughput ceiling than the STAR-RIS-SP-NOMA with ipCSI and ipSIC. The reason for the lower throughput ceiling of the STAR-RIS-SP-NOMA with ipCSI is due to the residual error that arises because of the ipCSI. Additionally, the STAR-RIS-SP-NOMA outperforms STAR-RIS-SP-OMA with ipCSI and ipSIC. In Figure 6.8, the system goodput is plotted against the transmit SNR for $\zeta=0.7,1, \psi=0.3$ and m=0.8. The system's goodput is plotted using (6.25). Analytical results match

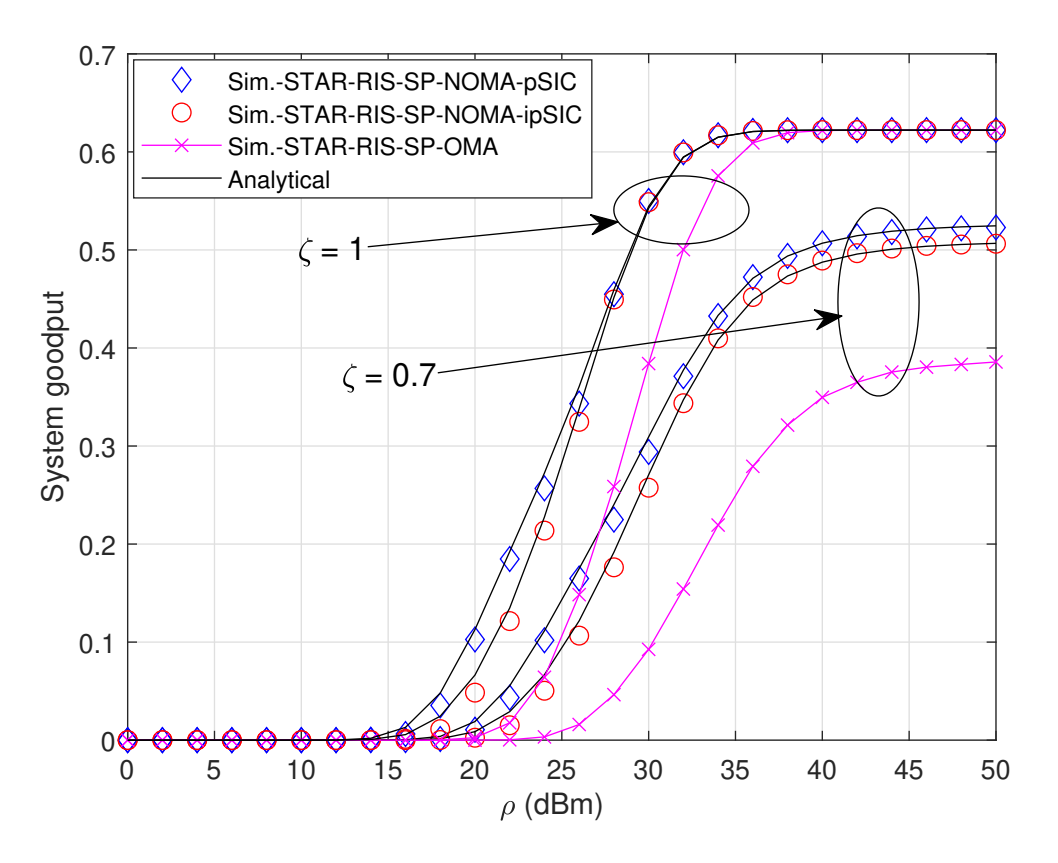


Figure 6.8: System goodput vs. transmit SNR.

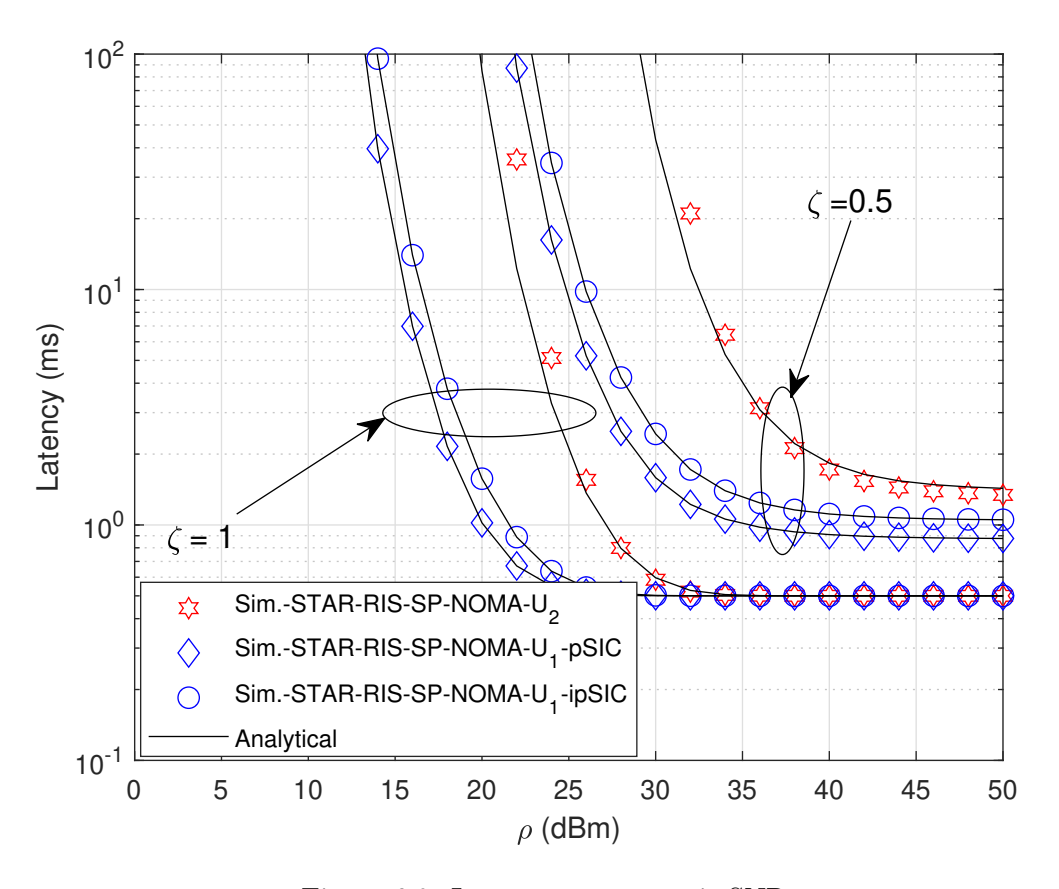


Figure 6.9: Latency vs. transmit SNR.

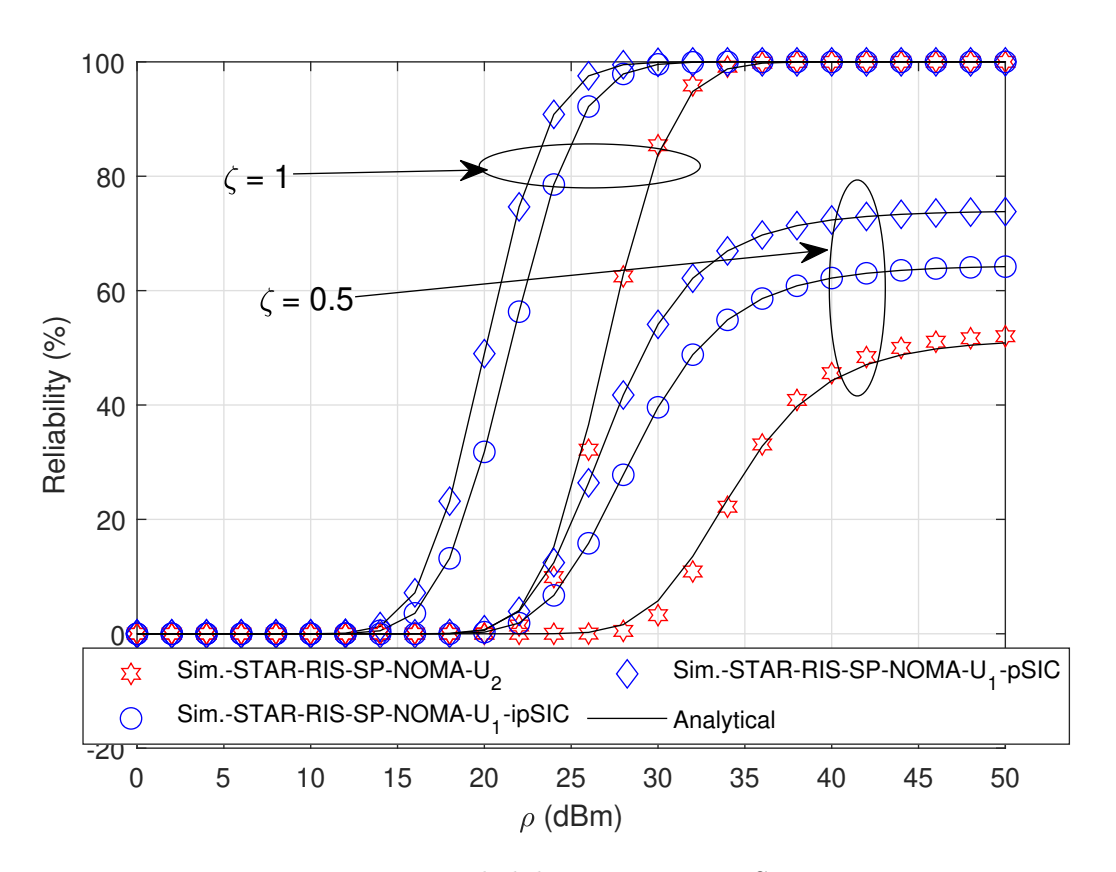


Figure 6.10: Reliability vs. transmit SNR.

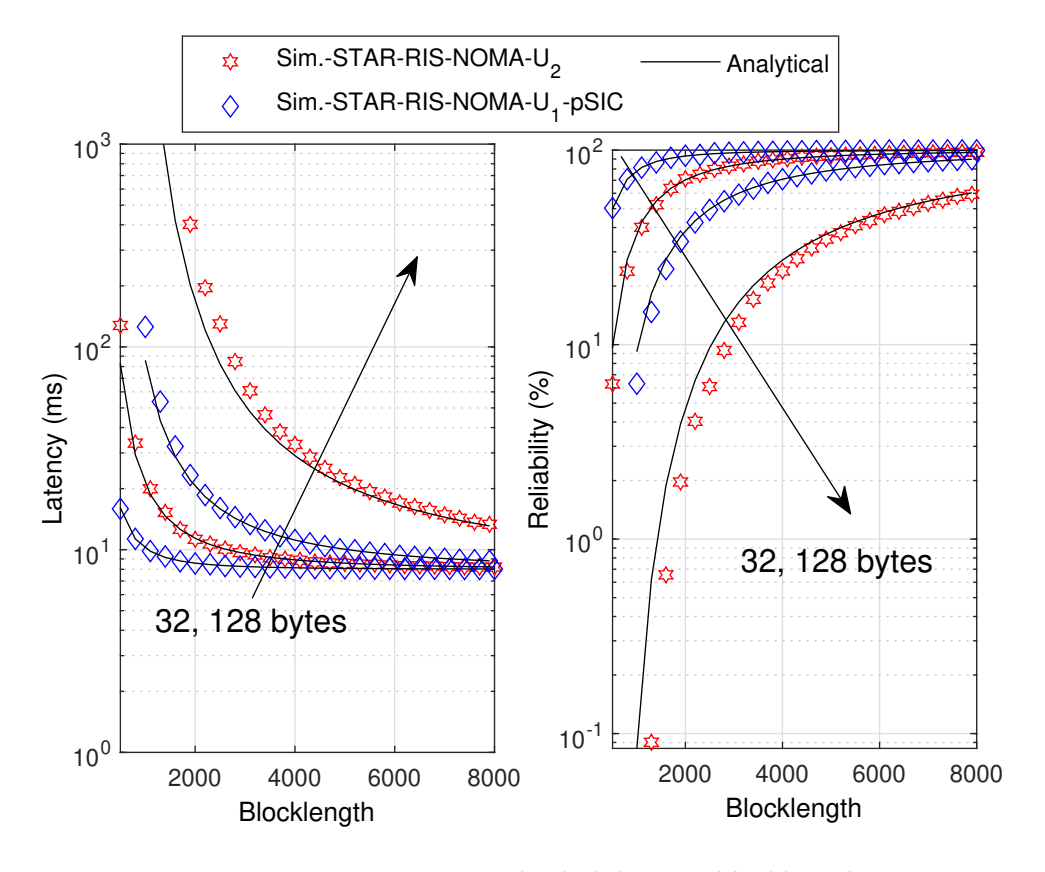


Figure 6.11: Latency and reliability vs. blocklength.

well with the simulated ones. As can be observed, the STAR-RIS-SP-NOMA system with pCSI and ipSIC can reach a higher goodput ceiling than the STAR-RIS-SP-NOMA with ipCSI and ipSIC. Also, the STAR-RIS-SP-NOMA outperforms STAR-RIS-SP-OMA with ipCSI and ipSIC. It should be noted that goodput is usually lower than throughput because it simply examines information bits successfully transferred and received, whereas throughput considers all the bits, including the training bits.

In Figure 6.9, we show the latency versus transmit SNR for $\zeta = 0.7, 1, \psi = 0.3$ and m = 0.8 is plotted according to (6.26) for U_1 and U_2 . The analytical results match well with the simulated ones. As observed in Figure 6.9, the latency of U_1 and U_2 decreases with increased transmit SNR for pCSI, ipCSI, and ipSIC. This is because of reduced re-transmissions and a reduction in the ABLER at higher transmit SNR. Furthermore, increasing transmit SNR leads to the saturation of latency for U_1 and U_2 because of the low value of ABLER, after which a condition of almost no re-transmission is reached. For instance, latency for both the users, U_1 and U_2 , approaches less than 1 ms, around 20 dBm and 27 dBm of transmit SNR for the case of pCSI ($\zeta = 1$), while for the case of ipCSI ($\zeta = 0.5$), it attains the same value at higher transmit SNR as ζ decreases. This demonstrates that our suggested system can fulfill the demanding requirements of URLLC applications. Conversely, Figure 6.10 shows the variation of reliability against transmit SNR for $\zeta = 0.7, 1, \ \psi = 0.3$ and m = 0.8. The analytical results are plotted using (6.26) and match well with the simulated ones. As in the case of latency, a significant improvement in reliability is observed for both the cases of pCSI and ipCSI with an increase in transmit SNR. To attain reliability of 99.99% in pCSI, U_1 and U_2 necessitate transmit SNR levels of about 27 dBm and 33 dBm, respectively. It can be observed that in the case of ipCSI $\zeta = 0.5$, the STAR-RIS-SP-NOMA system is not able to meet the URLLC reliability requirement of 99.99%. In Fig. 6.11, the impact of blocklength and the number of information bits on the latency and reliability of the proposed system for $\rho = 30$ dBm and $\zeta = 0.8$ is analyzed. It can be observed from (6.26) that the latency and reliability are functions of blocklength and packet size (information bits contained in N_1 and N_2). It can be observed from the figure that as the packet size increases from 32 to 128 bytes, the latency increases and reliability decreases. There is a trade-off between packet size and blocklength. As blocklength increases, the ABLER decreases, which results in lower latency and higher reliability, but as the packet size increases, the latency increases and reliability decreases. Therefore, as can be observed from the figure, when the packet size is 32 bytes, the system nearly achieves a latency of 8 ms and a reliability of 90% with a

blocklength of 2000. However, in the case of a longer packet size of 128 bytes, the latency and reliability change drastically with blocklength more than 4000.

6.4 Summary

In this chapter, we investigated the performance of the downlink STAR-RIS-SP-NOMA network under the effect of ipSIC and ipCSI. To analyze the system's performance, firstly, we derive the statistical characterization of the cascaded Nakagami-m channels through the Laguerre polynomial series approximation. Secondly, the approximate closed-form expressions for ABLER, system throughput, goodput, latency, and reliability are derived with pCSI, ipCSI, pSIC, and ipSIC. We have also derived asymptotic ABLER expression at high transmit SNR regimes for pCSI, ipCSI, pSIC, and ipSIC Finally, through the numerical results, it is shown that: to gain useful insights. 1) the analytical results corroborate with the simulation results; 2) the superior performance of STAR-RIS-SP-NOMA over STAR-RIS-SP-OMA, DF-HD-SP-OMA, and AF-HD-SP-OMA scenarios; 3) the TS protocol could achieve the best performance, and the MS protocol has the worst performance; 4) a degradation in the performance is observed with increasing ipCSI and ipSIC as compared to the case with pCSI and pSIC; 5) ipCSI causes error floor for ABLER at high transmit SNR regimes; 6) ABLER reduces with increase in the number of STAR-RIS elements; 7) increase in blocklength leads to decrease in ABLER, which results in lower latency and increased reliability, but as the packet size increases, the latency increases and reliability decreases.

Chapter 7

Conclusion and Future Work

In this thesis, we presented our work on the performance analysis of RIS-assisted communication with spectrally efficient signaling techniques like NOMA, CR, and FDTW using IBL and FBL codes. In this chapter, we conclude the thesis by summarizing its key points and proposing future research directions that can be built upon the work presented.

7.1 Conclusion

The brief summary of the conclusions of this thesis is presented below.

- 1. Performance analysis and a novel phase shift matrix design for RIS-assisted NOMA.
 - (a) A new design of the RIS-NOMA system is proposed to provide a coherent phase shift to both users in the NOMA pair by utilizing all the elements of an RIS simultaneously. The performance of the same design on RIS-assisted NOMA network is investigated.
 - (b) The closed-form expression of OP and system throughput is derived.
 - (c) The Monte-Carlo simulations are also presented to verify the closed-form expressions. Numerical results confirm the superiority of the proposed design of the RIS-NOMA system over other existing scenarios of RIS-NOMA systems.
- 2. Performance analysis of wireless-powered RIS-assisted CR-NOMA networks with HIs using IBL and FBL codes.
 - (a) The performance of the considered system is analyzed using IBL and FBL transmission. For the IBL, the system performance is analyzed by deriving the analytical expression of OP and system throughput. For the FBL, the system performance is analyzed by deriving the analytical expression for the ABLER, goodput, latency, and reliability.
 - (b) Asymptotic analysis is also done at a higher transmit regime for both IBL and FBL regimes.

- (c) The wireless-powered RIS-assisted CR-NOMA system outperforms its OMA counterpart in IBL and FBL analysis. Practical imperfections like HIs and ipSIC degrade the system's performance.
- (d) Finally, the impact of other system parameters, such as the number of antennas at the B, the number of antennas at PU, the number of RIS elements, and the TS factor on the system performance, is also examined.
- 3. Performance analysis of ARIS-assisted FDTW communication with HIs under FBL regime.
 - (a) Under the FBL regime, the novel analytical expressions for ABLER, EC, system throughput, goodput, and latency are derived for ARIS-FDTW systems under the influence of LI and HIs.
 - (b) Diversity order and multiplexing gains have been examined based on the asymptotic analysis in the higher transmit power conditions to provide useful insights.
 - (c) The ARIS-FDTW system's performance is observed to be superior than that of the PRIS-FDTW system and conventional FDTW-AF and FDTW-DF relay scenarios under the FBL regime.
- 4. Performance analysis of STAR-RIS assisted short packet NOMA system under ipSIC and ipCSI.
 - (a) The novel analytical expressions of ABLER, system throughput, goodput, latency, and reliability are derived with pCSI, ipCSI, pSIC, and ipSIC. Asymptotic ABLER expressions at high transmit SNR regimes for pCSI, ipCSI, pSIC, and ipSIC are also derived to gain useful insights.
 - (b) The superior performance of STAR-RIS-SP-NOMA is observed over STAR-RIS-SP-OMA, DF-HD-SP-OMA, and AF-HD-SP-OMA scenarios.
 - (c) A degradation is observed in the performance with increasing ipCSI and ipSIC compared to the case with pCSI and pSIC. ipCSI causes an error floor for ABLER at high transmit SNR regimes.
 - (d) Increase in blocklength leads to a decrease in ABLER, which results in lower latency and increased reliability, but as the packet size increases, the latency increases, and reliability decreases.

7.2 Future Work

Some of the possible directions that can be taken up as extensions of this work are suggested as:

- Designing a phase shift matrix for ARIS-NOMA that provides coherent phase shifts to multiple users by using all RIS elements simultaneously.
- Implementing RIS-NOMA network with non-terrestrial networks like integrated satellite-terrestrial networks and high-altitude platform systems.
- Performance analysis of wireless-powered RIS-assisted CR-MIMO NOMA in IBL and FBL regimes. Optimizing PA and TS factors to minimize OP and maximize system throughput for the same system model.
- Performance analysis of wireless-powered RIS-assisted CR-MIMO NOMA in IBL and FBL regimes with non-linear energy harvesting model.
- Implementing ARIS-FDTW system by considering discrete phase shifts of ARIS, multiuser scenario, and ipCSI.
- Investigating the performance of STAR-RIS assisted short packet NOMA under ipCSI by considering a multiantenna at the source and multiple antennas at the user side.

Chapter A

Appendix

A.1 Derivation of (3.9) and (3.10)

Since, $|\Psi_{2,2}| = c_2 A_2 \sum_{k=1}^K |h_{SR_k}| |h_{R_k U_2}|$, and $|h_{XY}|$ follows a Rayleigh distribution with mean $\frac{1}{2} \sqrt{\pi/A \left(d_{XY}\right)}$ and variance $(4-\pi)/4A \left(d_{XY}\right)$. We have considered the channels to be independent. Thus, the mean and variance of $|\Psi_{2,2}|$ can be computed as

$$\mathbb{E}[|\Psi_{2,2}|] = K\pi c_2 A_2 / 4,\tag{A.1}$$

$$Var[|\Psi_{2,2}|] = K\left(1 - \frac{\pi^2}{16}\right) (c_2 A_2)^2,$$
 (A.2)

where, $A_2 = 1/\sqrt{A(d_{SR}) A(d_{RU_2})}$. Using (A.1) and (A.2), the shape and scale parameter of the Gamma distribution denoted by $\Lambda_{|\Psi_{2,2}|}$ and $\lambda_{|\Psi_{2,2}|}$, respectively, can be obtained by using moment-matching method [77] as:

$$\Lambda_{|\Psi_{2,2}|} = \frac{(\mathbb{E}[|\Psi_{2,2}|])^2}{Var[|\Psi_{2,2}|]} = \frac{K\pi^2}{16 - \pi^2},\tag{A.3}$$

$$\lambda_{|\Psi_{2,2}|} = \frac{Var[|\Psi_{2,2}|]}{(\mathbb{E}[|\Psi_{2,2}|])} = \left(\frac{4}{\pi} - \frac{\pi}{4}\right)c_2A_2,\tag{A.4}$$

Furthermore, let $Z = |\Psi_{2,2}|^2$, then the CDF of Z can be deduced from $|\Psi_{2,2}|$ as $\mathcal{F}_Z(x) = P(0 \le |\Psi_{2,2}| \le \sqrt{x}) = \mathcal{F}_{|\Psi_{2,2}|^2}(\sqrt{x})$ by transformation of random variables. Therefore, the CDF of $|\Psi_{2,2}|^2$ can be expressed as in (3.9). The PDF can be obtained in (3.10) by differentiating (3.9).

A.2 Derivation of (3.11) and (3.12)

To determine the PDF of $|\Psi_{1,2}|^2$, firstly we start with $|\Psi_{1,2}| = A_2|\sum_{k=1}^K h_{R_k U_2} c_1 e^{-j\phi_{U_1}^k} h_{SR_k}|$. We can write $\Psi_{1,2} = \Re(\Psi_{1,2}) + j\Im(\Psi_{1,2})$, where, $\Re(.)$ and $\Im(.)$ denote the real and imaginary parts of a complex number respectively. Since h_{SR_k} and $h_{R_k U_2}$ are independent with $\phi_{U_1}^k \in (-\pi, \pi)$. Therefore, $\mathbb{E}[\Re(\Psi_{1,2})] = \mathbb{E}[\Im(\Psi_{1,2})] = 0$

and $Var[\mathfrak{R}(\Psi_{1,2})] = Var[\mathfrak{I}(\Psi_{1,2})] = K(c_1A_2)^2/2$. Thus $\mathfrak{R}(\Psi_{1,2}) \sim \mathcal{N}(0, Var[\mathfrak{R}(\Psi_{1,2})])$ and $\mathfrak{I}(\Psi_{1,2}) \sim \mathcal{N}(0, Var[\mathfrak{I}(\Psi_{1,2})])$. We obtained the results in (3.11) and (3.12) by fitting them with the Gamma distribution.

A.3 Derivation of (4.19)

By using (4.8) and (4.9) in (4.16) and applying a similar analysis as in [125], we can write (4.17) as

$$P_{1}^{out} = \underbrace{\Pr\left(|h_{s1}|^{2} < \frac{\delta_{1}}{\Delta_{s}\rho|h_{bs}^{\sum}|^{2}}, \rho \leq \frac{\rho_{th}}{|h_{sd}^{\sum}|^{2}}\right)}_{I_{1}} + \underbrace{\Pr\left(|h_{s1}|^{2} < \frac{\delta_{1}|h_{sd}^{\sum}|^{2}}{\rho_{th}}, \rho > \frac{\rho_{th}}{|h_{sd}^{\sum}|^{2}}\right)}_{I_{2}}$$
(A.5)

Thus, I_1 and I_2 can be written as

$$I_1 = \mathcal{F}_{|h_{sd}^{\sum}|^2} \left(\frac{\rho_{th}}{\rho}\right) \int_0^\infty \mathcal{F}_{|h_{s1}|^2} \left(\frac{\delta_1}{\Delta_s \rho y}\right) \frac{y^{N-1}}{\Omega_{bs}^N \Gamma(N)} e^{-\frac{y}{\Omega_{bs}}} dy, \tag{A.6}$$

$$I_2 = \int_{\frac{\rho_{th}}{\rho}}^{\infty} f_{|h_{sd}^{\Sigma}|^2}(x) \mathcal{F}_{|h_{s1}|^2} \left(\frac{\delta_1 x}{\rho_{th}}\right) dx, \tag{A.7}$$

Further, by using the GLQ [120] in (A.6) and (A.7), we can obtain the results as in (4.19).

A.4 Derivation of (4.20)

On applying coherent phase shifts, $\mathcal{X} = \sum_{k=1}^{K} (|h_{sk}h_{k2}|)^2$, and by using (4.10), we can write (4.18) as

$$P_2^{out} = \underbrace{\Pr\left(\mathcal{X} < \frac{\delta_2}{\Delta_s \rho \left|h_{bs}^{\Sigma}\right|^2}, \rho \leq \frac{\rho_{th}}{|h_{sd}^{\Sigma}|^2}\right)}_{I_2} + \underbrace{\Pr\left(\mathcal{X} < \frac{\delta |h_{sd}^{\Sigma}|^2}{\rho_{th}}, \rho > \frac{\rho_{th}}{|h_{sd}^{\Sigma}|^2}\right)}_{I_2}$$
(A.8)

Furthermore, I_3 and I_4 can be simplified as

$$I_3 = \mathcal{F}_{|h_{sd}^{\sum}|^2} \left(\frac{\rho_{th}}{\rho}\right) \int_0^\infty \mathcal{F}_{\mathcal{X}} \left(\frac{\delta_2}{\Delta_s \rho y}\right) \frac{y^{N-1}}{\Omega_{bs}^N \Gamma(N)} e^{-\frac{y}{\Omega_{bs}}} dy, \tag{A.9}$$

$$I_4 = \int_{\frac{\rho_{th}}{\rho}}^{\infty} f_{|h_{sd}^{\sum}|^2}(x) \mathcal{F}_{\mathcal{X}}\left(\frac{\delta_2 x}{\rho_{th}}\right) dx, \tag{A.10}$$

The integrals in (A.9) and (A.10) are evaluated using the GLQ [120] and the results are obtained as in (4.20).

A.5 Derivation of (5.6)

The CDF of $\mathcal{F}_{\gamma_2}(x)$ can be written as shown

$$\mathcal{F}_{\gamma_2}(x) = Pr\left(\left|\sum_{n=1}^{N} h_{1n} h_{n2}\right|^2 < \frac{\Psi}{\beta} \left(P_2 \chi_g |g_2|^2 + c_n\right)\right), \tag{A.11}$$

where, $\Psi = \frac{x}{P_1(1-xk_{12}^2)}$ and the CDF of \mathcal{X} is given in (5.5), $Y = |g_2|^2$ and the PDF of Y is an exponential random variable represented as $f_Y(y) = \frac{1}{\Omega_{LI}}e^{\frac{-y}{\Omega_{LI}}}$. Therefore, (A.11) can be written as shown in (A.12).

$$\mathcal{F}_{\gamma_{2}}(x) = \int_{0}^{\infty} \mathcal{F}_{\mathcal{X}} \left[\Psi \beta^{-1} \left(y P_{2} \chi_{g} + c_{n} \right) \right] f_{Y}(y) dy
= \frac{1}{\Gamma(\varphi_{n} + 1)} \int_{0}^{\infty} \Upsilon \left(\varphi_{n} + 1, \frac{\sqrt{\Psi(y \chi_{g} P_{2} + c_{n})}}{\sqrt{\beta} \phi_{n}} \right) \frac{1}{\Omega_{LI}} e^{\frac{-y}{\Omega_{LI}}} dy.$$
(A.12)

By applying the GLQ [120] in (A.12), we obtain the CDF, $\mathcal{F}_{\gamma_2}(x)$ as shown in (A.13).

$$\mathcal{F}_{\gamma_2}(x) \approx \sum_{u=1}^{U} H_u \frac{1}{\Gamma(\varphi_n + 1)} \Upsilon\left(\varphi_n + 1, \frac{\sqrt{\Psi(b_n x_u + c_n)}}{\sqrt{\beta} \phi_n}\right). \tag{A.13}$$

Further, by applying the GCQ [120] method in (A.13), we obtain the result as in (5.6).

- G. Marconi, "Wireless telegraphic communication," Nobel Lecture, vol. 11, pp. 198–222, 1909.
- [2] R. Simons, "Guglielmo marconi and early systems of wireless communication," *Gec Review*, vol. 11, no. 1, pp. 37–55, 1996.
- [3] T. M. Cover, Elements of information theory. John Wiley & Sons, 1999.
- [4] C. E. Shannon, "A mathematical theory of communication," *The Bell system technical journal*, vol. 27, no. 3, pp. 379–423, 1948.
- [5] P. Nicopolitidis, A. Pomportsis, G. I. Papadimitriou, and M. S. Obaidat, Wireless networks. John Wiley & Sons, Inc., 2003.
- [6] M. Zeng, A. Annamalai, and V. K. Bhargava, "Recent advances in cellular wireless communications," *IEEE Communications magazine*, vol. 37, no. 9, pp. 128–138, 1999.
- [7] W. Stallings, Wireless communications & networks. Pearson Education India, 2009.
- [8] U. Varshney and R. Jain, "Issues in emerging 4g wireless networks," *Computer*, vol. 34, no. 6, pp. 94–96, 2001.
- [9] M. Shafi, A. F. Molisch, P. J. Smith, T. Haustein, P. Zhu, P. De Silva, F. Tufvesson, A. Benjebbour, and G. Wunder, "5G: A tutorial overview of standards, trials, challenges, deployment, and practice," *IEEE Journal on Selected Areas in Communications*, vol. 35, no. 6, pp. 1201–1221, 2017.
- [10] F. Tariq, M. R. A. Khandaker, K.-K. Wong, M. A. Imran, M. Bennis, and M. Debbah, "A speculative study on 6G," *IEEE Wireless Communications*, vol. 27, no. 4, pp. 118–125, 2020.
- [11] L. E. M. Matheus, A. B. Vieira, L. F. M. Vieira, M. A. M. Vieira, and O. Gnawali, "Visible light communication: Concepts, applications and challenges," *IEEE Communications Surveys & Tutorials*, vol. 21, no. 4, pp. 3204–3237, 2019.

[12] F. Liu, Y. Cui, C. Masouros, J. Xu, T. X. Han, Y. C. Eldar, and S. Buzzi, "Integrated sensing and communications: Toward dual-functional wireless networks for 6G and beyond," *IEEE Journal on Selected Areas in Communications*, vol. 40, no. 6, pp. 1728–1767, 2022.

- [13] Q. Wu and R. Zhang, "Towards smart and reconfigurable environment: Intelligent reflecting surface aided wireless network," *IEEE Communications Magazine*, vol. 58, no. 1, pp. 106–112, 2019.
- [14] Y. Liu, W. Yi, Z. Ding, X. Liu, O. A. Dobre, and N. Al-Dhahir, "Developing NOMA to next generation multiple access: Future vision and research opportunities," *IEEE Wireless Communications*, vol. 29, no. 6, pp. 120–127, 2022.
- [15] G. Araniti, A. Iera, S. Pizzi, and F. Rinaldi, "Toward 6G non-terrestrial networks," IEEE Network, vol. 36, no. 1, pp. 113–120, 2022.
- [16] C. Liaskos, S. Nie, A. Tsioliaridou, A. Pitsillides, S. Ioannidis, and I. Akyildiz, "A new wireless communication paradigm through software-controlled metasurfaces," IEEE Communications Magazine, vol. 56, no. 9, pp. 162–169, 2018.
- [17] Q. Wu and R. Zhang, "Intelligent reflecting surface enhanced wireless network via joint active and passive beamforming," *IEEE Transactions on Wireless Communications*, vol. 18, no. 11, pp. 5394–5409, 2019.
- [18] C. Pan, H. Ren, K. Wang, J. F. Kolb, M. Elkashlan, M. Chen, M. Di Renzo, Y. Hao, J. Wang, A. L. Swindlehurst, et al., "Reconfigurable intelligent surfaces for 6g systems: Principles, applications, and research directions," IEEE Communications Magazine, vol. 59, no. 6, pp. 14–20, 2021.
- [19] E. Basar, M. Di Renzo, J. De Rosny, M. Debbah, M.-S. Alouini, and R. Zhang, "Wireless communications through reconfigurable intelligent surfaces," *IEEE Access*, vol. 7, pp. 116753–116773, 2019.
- [20] M. Di Renzo, A. Zappone, M. Debbah, M.-S. Alouini, C. Yuen, J. de Rosny, and S. Tretyakov, "Smart radio environments empowered by reconfigurable intelligent surfaces: How it works, state of research, and the road ahead," *IEEE Journal on Selected Areas in Communications*, vol. 38, no. 11, pp. 2450–2525, 2020.
- [21] Y. Liu, X. Mu, J. Xu, R. Schober, Y. Hao, H. V. Poor, and L. Hanzo, "STAR:

Simultaneous transmission and reflection for 360° coverage by intelligent surfaces," *IEEE Wireless Communications*, vol. 28, no. 6, pp. 102–109, 2021.

- [22] U. Cisco, "Cisco annual internet report (2018–2023) white paper," Cisco: San Jose, CA, USA, vol. 10, no. 1, pp. 1–35, 2020.
- [23] Z. Zhang, Y. Xiao, Z. Ma, M. Xiao, Z. Ding, X. Lei, G. K. Karagiannidis, and P. Fan, "6G wireless networks: Vision, requirements, architecture, and key technologies," IEEE Vehicular Technology Magazine, vol. 14, no. 3, pp. 28–41, 2019.
- [24] C. Han, Y. Wu, Z. Chen, and X. Wang, "Terahertz communications (teracom): Challenges and impact on 6G wireless systems. arxiv 2019," arXiv preprint arXiv:1912.06040, 1912.
- [25] Y. Liu, S. Zhang, X. Mu, Z. Ding, R. Schober, N. Al-Dhahir, E. Hossain, and X. Shen, "Evolution of noma toward next generation multiple access (NGMA) for 6G," *IEEE Journal on Selected Areas in Communications*, vol. 40, no. 4, pp. 1037–1071, 2022.
- [26] Z. Ding, Y. Liu, J. Choi, Q. Sun, M. Elkashlan, I. Chih-Lin, and H. V. Poor, "Application of non-orthogonal multiple access in LTE and 5G networks," *IEEE Communications Magazine*, vol. 55, no. 2, pp. 185–191, 2017.
- [27] Z. Ding, X. Lei, G. K. Karagiannidis, R. Schober, J. Yuan, and V. K. Bhargava, "A survey on non-orthogonal multiple access for 5G networks: Research challenges and future trends," *IEEE Journal on Selected Areas in Communications*, vol. 35, no. 10, pp. 2181–2195, 2017.
- [28] Z. Liu and L.-L. Yang, "Sparse or dense: A comparative study of code-domain NOMA systems," *IEEE Transactions on Wireless Communications*, vol. 20, no. 8, pp. 4768–4780, 2021.
- [29] W. Tang, M. Z. Chen, X. Chen, J. Y. Dai, Y. Han, M. Di Renzo, Y. Zeng, S. Jin, Q. Cheng, and T. J. Cui, "Wireless communications with reconfigurable intelligent surface: Path loss modeling and experimental measurement," *IEEE Transactions on Wireless Communications*, vol. 20, no. 1, pp. 421–439, 2021.
- [30] H. Zhang, S. Zeng, B. Di, Y. Tan, M. Di Renzo, M. Debbah, Z. Han, H. V. Poor, and L. Song, "Intelligent omni-surfaces for full-dimensional wireless communications:

Principles, technology, and implementation," *IEEE Communications Magazine*, vol. 60, no. 2, pp. 39–45, 2022.

- [31] N. Docomo, "Docomo conducts world's first successful trial of transparent dynamic metasurface," Online. www. nttdocomo.co. jp/english/info/mediacenter/pr/2020/0117 00. html, 2020.
- [32] Q. Wu, S. Zhang, B. Zheng, C. You, and R. Zhang, "Intelligent reflecting surface-aided wireless communications: A tutorial," *IEEE Transactions on Communications*, vol. 69, no. 5, pp. 3313–3351, 2021.
- [33] Z. Zhang, L. Dai, X. Chen, C. Liu, F. Yang, R. Schober, and H. V. Poor, "Active RIS vs. passive RIS: Which will prevail in 6G?," *IEEE Transactions on Communications*, vol. 71, no. 3, pp. 1707–1725, 2023.
- [34] C. You and R. Zhang, "Wireless communication aided by intelligent reflecting surface: Active or passive?," *IEEE Wireless Communications Letters*, vol. 10, no. 12, pp. 2659–2663, 2021.
- [35] K. K. Kishor and S. V. Hum, "An amplifying reconfigurable reflectarray antenna," *IEEE Transactions on Antennas and Propagation*, vol. 60, no. 1, pp. 197–205, 2012.
- [36] K. Liu, Z. Zhang, L. Dai, S. Xu, and F. Yang, "Active reconfigurable intelligent surface: Fully-connected or sub-connected?," *IEEE Communications Letters*, vol. 26, no. 1, pp. 167–171, 2022.
- [37] X. Mu, Y. Liu, L. Guo, J. Lin, and R. Schober, "Simultaneously transmitting and reflecting (STAR) RIS aided wireless communications," *IEEE Transactions on Wireless Communications*, vol. 21, no. 5, pp. 3083–3098, 2022.
- [38] F. Boccardi, R. W. Heath, A. Lozano, T. L. Marzetta, and P. Popovski, "Five disruptive technology directions for 5G," *IEEE Communications Magazine*, vol. 52, no. 2, pp. 74–80, 2014.
- [39] P. Popovski, "Ultra-reliable communication in 5g wireless systems," in 1st International Conference on 5G for Ubiquitous Connectivity, pp. 146–151, 2014.
- [40] Y. Li, X. Cheng, Y. Cao, D. Wang, and L. Yang, "Smart choice for the smart grid: Narrowband internet of things (nb-iot)," *IEEE Internet of Things Journal*, vol. 5, no. 3, pp. 1505–1515, 2018.

[41] H. Ren, C. Pan, Y. Deng, M. Elkashlan, and A. Nallanathan, "Resource allocation for secure URLLC in mission-critical IoT scenarios," *IEEE Transactions on Communications*, vol. 68, no. 9, pp. 5793–5807, 2020.

- [42] G. Durisi, T. Koch, and P. Popovski, "Toward massive, ultrareliable, and low-latency wireless communication with short packets," *Proceedings of the IEEE*, vol. 104, no. 9, pp. 1711–1726, 2016.
- [43] H. Ji, S. Park, J. Yeo, Y. Kim, J. Lee, and B. Shim, "Ultra-reliable and low-latency communications in 5G downlink: Physical layer aspects," *IEEE Wireless Communications*, vol. 25, no. 3, pp. 124–130, 2018.
- [44] G. Durisi, T. Koch, J. Östman, Y. Polyanskiy, and W. Yang, "Short-packet communications over multiple-antenna rayleigh-fading channels," *IEEE Transactions on Communications*, vol. 64, no. 2, pp. 618–629, 2016.
- [45] Y. Gu, H. Chen, Y. Li, L. Song, and B. Vucetic, "Short-packet two-way amplify-and-forward relaying," *IEEE Signal Processing Letters*, vol. 25, no. 2, pp. 263–267, 2018.
- [46] Y. Polyanskiy, H. V. Poor, and S. Verdu, "Channel coding rate in the finite blocklength regime," *IEEE Transactions on Information Theory*, vol. 56, no. 5, pp. 2307–2359, 2010.
- [47] C. Huang, A. Zappone, G. C. Alexandropoulos, M. Debbah, and C. Yuen, "Reconfigurable intelligent surfaces for energy efficiency in wireless communication," IEEE Transactions on Wireless Communications, vol. 18, no. 8, pp. 4157–4170, 2019.
- [48] E. Björnson, Ö. Özdogan, and E. G. Larsson, "Intelligent reflecting surface versus decode-and-forward: How large surfaces are needed to beat relaying?," *IEEE Wireless Communications Letters*, vol. 9, no. 2, pp. 244–248, 2019.
- [49] A.-A. A. Boulogeorgos and A. Alexiou, "Performance analysis of reconfigurable intelligent surface-assisted wireless systems and comparison with relaying," *IEEE Access*, vol. 8, pp. 94463–94483, 2020.
- [50] L. Yang, J. Yang, W. Xie, M. O. Hasna, T. Tsiftsis, and M. D. Renzo, "Secrecy performance analysis of RIS-aided wireless communication systems," *IEEE Transactions on Vehicular Technology*, vol. 69, no. 10, pp. 12296–12300, 2020.

[51] L. Yang, F. Meng, Q. Wu, D. B. da Costa, and M.-S. Alouini, "Accurate closed-form approximations to channel distributions of RIS-aided wireless systems," *IEEE Wireless Communications Letters*, vol. 9, no. 11, pp. 1985–1989, 2020.

- [52] L. Yang, F. Meng, J. Zhang, M. O. Hasna, and M. D. Renzo, "On the performance of ris-assisted dual-hop uav communication systems," *IEEE Transactions on Vehicular Technology*, vol. 69, no. 9, pp. 10385–10390, 2020.
- [53] S. Atapattu, R. Fan, P. Dharmawansa, G. Wang, J. Evans, and T. A. Tsiftsis, "Reconfigurable intelligent surface assisted two-way communications: Performance analysis and optimization," *IEEE Transactions on Communications*, vol. 68, no. 10, pp. 6552–6567, 2020.
- [54] A. Hemanth, K. Umamaheswari, A. C. Pogaku, D.-T. Do, and B. M. Lee, "Outage performance analysis of reconfigurable intelligent surfaces-aided noma under presence of hardware impairment," *IEEE Access*, vol. 8, pp. 212156–212165, 2020.
- [55] C. Guo, Y. Cui, F. Yang, and L. Ding, "Outage probability analysis and minimization in intelligent reflecting surface-assisted miso systems," *IEEE Communications Letters*, vol. 24, no. 7, pp. 1563–1567, 2020.
- [56] T. N. Do, G. Kaddoum, T. L. Nguyen, D. B. da Costa, and Z. J. Haas, "Multi-RIS-aided wireless systems: Statistical characterization and performance analysis," *IEEE Transactions on Communications*, vol. 69, no. 12, pp. 8641–8658, 2021.
- [57] P. Yang, L. Yang, and S. Wang, "Performance analysis for ris-aided wireless systems with imperfect CSI," *IEEE Wireless Communications Letters*, vol. 11, no. 3, pp. 588–592, 2022.
- [58] S. Hong, C. Pan, H. Ren, K. Wang, K. K. Chai, and A. Nallanathan, "Robust transmission design for intelligent reflecting surface-aided secure communication systems with imperfect cascaded csi," *IEEE Transactions on Wireless Communications*, vol. 20, no. 4, pp. 2487–2501, 2021.
- [59] K.-T. Nguyen, T.-H. Vu, H. Shin, and S. Kim, "Performance analysis of active RIS and passive RIS-aided MISO systems over nakagami-m fading channel with imperfect csi," *IEEE Transactions on Vehicular Technology*, pp. 1–15, 2024.

[60] A. U. Khan, G. Abbas, Z. H. Abbas, M. Bilal, S. C. Shah, and H. Song, "Reliability analysis of cognitive radio networks with reserved spectrum for 6G-IoT," *IEEE Transactions on Network and Service Management*, vol. 19, no. 3, pp. 2726–2737, 2022.

- [61] G. Pan, J. Ye, J. An, and M.-S. Alouini, "Full-duplex enabled intelligent reflecting surface systems: Opportunities and challenges," *IEEE Wireless Communications*, vol. 28, no. 3, pp. 122–129, 2021.
- [62] E. Ahmed and A. M. Eltawil, "All-digital self-interference cancellation technique for full-duplex systems," *IEEE Transactions on Wireless Communications*, vol. 14, no. 7, pp. 3519–3532, 2015.
- [63] D. Xu, X. Yu, Y. Sun, D. W. K. Ng, and R. Schober, "Resource allocation for IRS-assisted full-duplex cognitive radio systems," *IEEE Transactions on Communications*, vol. 68, no. 12, pp. 7376–7394, 2020.
- [64] L. Zhang, Y. Wang, W. Tao, Z. Jia, T. Song, and C. Pan, "Intelligent reflecting surface aided MIMO cognitive radio systems," *IEEE Transactions on Vehicular Technology*, vol. 69, no. 10, pp. 11445–11457, 2020.
- [65] J. Yuan, Y.-C. Liang, J. Joung, G. Feng, and E. G. Larsson, "Intelligent reflecting surface-assisted cognitive radio system," *IEEE Transactions on Communications*, vol. 69, no. 1, pp. 675–687, 2021.
- [66] W. Jiang, Y. Zhang, J. Zhao, Z. Xiong, and Z. Ding, "Joint transmit precoding and reflect beamforming design for IRS-assisted MIMO cognitive radio systems," *IEEE Transactions on Wireless Communications*, vol. 21, no. 6, pp. 3617–3631, 2022.
- [67] X. Wu, J. Ma, Z. Xing, C. Gu, X. Xue, and X. Zeng, "Secure and energy efficient transmission for IRS-assisted cognitive radio networks," *IEEE Transactions on Cognitive Communications and Networking*, vol. 8, no. 1, pp. 170–185, 2022.
- [68] B. C. Nguyen, T. M. Hoang, L. T. Dung, and T. Kim, "On performance of two-way full-duplex communication system with reconfigurable intelligent surface," *IEEE Access*, vol. 9, pp. 81274–81285, 2021.
- [69] B. Lu, R. Wang, and Y. Liu, "Outage probability of intelligent reflecting surface assisted full duplex two-way communications," *IEEE Communications Letters*, vol. 26, no. 2, pp. 286–290, 2022.

[70] P. K. Sharma and P. Garg, "Intelligent reflecting surfaces to achieve the full-duplex wireless communication," *IEEE Communications Letters*, vol. 25, no. 2, pp. 622–626, 2021.

- [71] A. M. Tota Khel and K. A. Hamdi, "Performance analysis of IRS-assisted full-duplex wireless communication systems with interference," *IEEE Communications Letters*, vol. 26, no. 9, pp. 2027–2031, 2022.
- [72] T.-H. Vu and S. Kim, "Performance analysis of full-duplex two-way RIS-based systems with imperfect CSI and discrete phase-shift design," *IEEE Communications* Letters, vol. 27, no. 2, pp. 512–516, 2023.
- [73] K. Singh, F. Karim, S. K. Singh, P. K. Sharma, S. Mumtaz, and M. F. Flanagan, "Performance analysis of RIS-assisted full-duplex communications with infinite and finite blocklength codes," *IEEE Transactions on Communications*, vol. 71, no. 7, pp. 4262–4282, 2023.
- [74] B. Zheng, Q. Wu, and R. Zhang, "Intelligent reflecting surface-assisted multiple access with user pairing: NOMA or OMA?," *IEEE Communications Letters*, vol. 24, no. 4, pp. 753–757, 2020.
- [75] Y. Cheng, K. H. Li, Y. Liu, K. C. Teh, and H. V. Poor, "Downlink and uplink intelligent reflecting surface aided networks: NOMA and OMA," *IEEE Transactions* on Wireless Communications, vol. 20, no. 6, pp. 3988–4000, 2021.
- [76] Z. Ding, R. Schober, and H. V. Poor, "On the impact of phase shifting designs on IRS-NOMA," *IEEE wireless communications letters*, vol. 9, no. 10, pp. 1596–1600, 2020.
- [77] B. Tahir, S. Schwarz, and M. Rupp, "Analysis of uplink IRS-assisted NOMA under Nakagami-m fading via moments matching," *IEEE Wireless Communications Letters*, vol. 10, no. 3, pp. 624–628, 2021.
- [78] X. Yue and Y. Liu, "Performance analysis of intelligent reflecting surface assisted NOMA networks," *IEEE Transactions on Wireless Communications*, vol. 21, no. 4, pp. 2623–2636, 2021.
- [79] Z. Ding and H. V. Poor, "A simple design of IRS-NOMA transmission," *IEEE Communications Letters*, vol. 24, no. 5, pp. 1119–1123, 2020.

[80] Y. Cheng, K. H. Li, Y. Liu, K. C. Teh, and G. K. Karagiannidis, "Non-orthogonal multiple access (NOMA) with multiple intelligent reflecting surfaces," *IEEE Transactions on Wireless Communications*, vol. 20, no. 11, pp. 7184–7195, 2021.

- [81] A. R. Pawar, S. Kashyap, and S. Chouhan, "Error probability analysis of intelligent reflecting surface-enabled non-orthogonal multiple access systems," *IEEE Transactions on Vehicular Technology*, vol. 72, no. 7, pp. 9237–9251, 2023.
- [82] X. Yue, M. Song, C. Ouyang, Y. Liu, T. Li, and T. Hou, "Exploiting active RIS in NOMA networks with hardware impairments," *IEEE Transactions on Vehicular Technology*, vol. 73, no. 6, pp. 8207–8221, 2024.
- [83] W. Liang, W. Luo, J. Zhang, and Z. Ding, "Active and passive beamforming design for reconfigurable intelligent surface assisted CR-NOMA networks," *IEEE Communications Letters*, vol. 26, no. 10, pp. 2409–2414, 2022.
- [84] T.-H. Vu, T.-V. Nguyen, D. B. d. Costa, and S. Kim, "Reconfigurable intelligent surface-aided cognitive NOMA networks: Performance analysis and deep learning evaluation," *IEEE Transactions on Wireless Communications*, vol. 21, no. 12, pp. 10662–10677, 2022.
- [85] K. Guo, R. Liu, X. Li, L. Yang, K. An, and Y. Huang, "Outage performance of RIS-assisted cognitive non-terrestrial network with NOMA," *IEEE Transactions on Vehicular Technology*, vol. 73, no. 4, pp. 5953–5958, 2024.
- [86] P. T. Tin, M.-S. V. Nguyen, D.-H. Tran, C. T. Nguyen, S. Chatzinotas, Z. Ding, and M. Voznak, "Performance analysis of user pairing for active RIS-enabled cooperative NOMA in 6G cognitive radio networks," *IEEE Internet of Things Journal*, pp. 1–1, 2024.
- [87] J. Li, L. Yang, Q. Wu, X. Lei, F. Zhou, F. Shu, X. Mu, Y. Liu, and P. Fan, "Active RIS-aided NOMA-enabled space-air-ground integrated networks with cognitive radio," *IEEE Journal on Selected Areas in Communications*, pp. 1–1, 2024.
- [88] Y. Liu, X. Mu, J. Xu, R. Schober, Y. Hao, H. V. Poor, and L. Hanzo, "STAR: Simultaneous transmission and reflection for 360° coverage by intelligent surfaces," IEEE Wireless Communications, vol. 28, no. 6, pp. 102–109, 2021.
- [89] J. Zuo, Y. Liu, Z. Ding, L. Song, and H. V. Poor, "Joint design for

simultaneously transmitting and reflecting (STAR) RIS assisted NOMA systems," *IEEE Transactions on Wireless Communications*, vol. 22, no. 1, pp. 611–626, 2023.

- [90] C. Zhang, W. Yi, Y. Liu, Z. Ding, and L. Song, "STAR-IOS aided NOMA networks: Channel model approximation and performance analysis," *IEEE Transactions on Wireless Communications*, vol. 21, no. 9, pp. 6861–6876, 2022.
- [91] X. Yue, J. Xie, Y. Liu, Z. Han, R. Liu, and Z. Ding, "Simultaneously transmitting and reflecting reconfigurable intelligent surface assisted NOMA networks," *IEEE Transactions on Wireless Communications*, vol. 22, no. 1, pp. 189–204, 2023.
- [92] B. Zhao, C. Zhang, W. Yi, and Y. Liu, "Ergodic rate analysis of STAR-RIS aided NOMA systems," *IEEE Communications Letters*, vol. 26, no. 10, pp. 2297–2301, 2022.
- [93] Z. Xie, W. Yi, X. Wu, Y. Liu, and A. Nallanathan, "STAR-RIS aided NOMA in multicell networks: A general analytical framework with gamma distributed channel modeling," *IEEE Transactions on Communications*, vol. 70, no. 8, pp. 5629–5644, 2022.
- [94] Q. Li, M. El-Hajjar, Y. Sun, I. Hemadeh, A. Shojaeifard, Y. Liu, and L. Hanzo, "Achievable rate analysis of the STAR-RIS-aided NOMA uplink in the face of imperfect CSI and hardware impairments," *IEEE Transactions on Communications*, vol. 71, no. 10, pp. 6100–6114, 2023.
- [95] R. Hashemi, S. Ali, N. H. Mahmood, and M. Latva-aho, "Average rate and error probability analysis in short packet communications over RIS-aided URLLC systems," *IEEE Transactions on Vehicular Technology*, vol. 70, no. 10, pp. 10320–10334, 2021.
- [96] H. Ren, K. Wang, and C. Pan, "Intelligent reflecting surface-aided URLLC in a factory automation scenario," *IEEE Transactions on Communications*, vol. 70, no. 1, pp. 707–723, 2022.
- [97] A. Ranjha and G. Kaddoum, "URLLC facilitated by mobile UAV relay and RIS: A joint design of passive beamforming, blocklength, and UAV positioning," IEEE Internet of Things Journal, vol. 8, no. 6, pp. 4618–4627, 2021.
- [98] S. Dhok, P. Raut, P. K. Sharma, K. Singh, and C.-P. Li, "Non-linear energy

harvesting in RIS-assisted URLLC networks for industry automation," *IEEE Transactions on Communications*, vol. 69, no. 11, pp. 7761–7774, 2021.

- [99] M. Soleymani, I. Santamaria, E. Jorswieck, R. Schober, and L. Hanzo, "Optimization of the downlink spectral- and energy-efficiency of RIS-aided multi-user URLLC MIMO systems," *IEEE Transactions on Communications*, pp. 1–1, 2024.
- [100] L. Wang, B. Ai, Y. Niu, Z. Zhong, Z. Han, and N. Wang, "Joint reliability optimization and beamforming design for STAR-RIS-aided multi-user MISO URLLC systems," *IEEE Transactions on Vehicular Technology*, vol. 73, no. 6, pp. 8041–8054, 2024.
- [101] Y. Eghbali, S. K. Taskou, M. R. Mili, M. Rasti, and E. Hossain, "Providing URLLC service in multi-STAR-RIS assisted and full-duplex cellular wireless systems: A meta-learning approach," *IEEE Communications Letters*, vol. 28, no. 3, pp. 513–517, 2024.
- [102] T.-H. Vu, T.-V. Nguyen, D. B. d. Costa, and S. Kim, "Intelligent reflecting surface-aided short-packet non-orthogonal multiple access systems," *IEEE Transactions on Vehicular Technology*, vol. 71, no. 4, pp. 4500–4505, 2022.
- [103] L. Yuan, Q. Du, N. Yang, F. Fang, and N. Yang, "Performance analysis of IRS-aided short-packet NOMA systems over nakagami-m fading channels," *IEEE Transactions* on Vehicular Technology, vol. 72, no. 6, pp. 8228–8233, 2023.
- [104] C. Xia, Z. Xiang, B. Su, H. Liu, J. Meng, and G. Pan, "RIS-NOMA-assisted short-packet communication with hardware impairments," *IEEE Internet of Things Journal*, vol. 11, no. 2, pp. 2990–3002, 2024.
- [105] F. Karim, S. K. Singh, K. Singh, S. Prakriya, and M. F. Flanagan, "On the performance of STAR-RIS-aided NOMA at finite blocklength," *IEEE Wireless Communications Letters*, vol. 12, no. 5, pp. 868–872, 2023.
- [106] T.-H. Vu, T.-V. Nguyen, Q.-V. Pham, D. Benevides da Costa, and S. Kim, "STAR-RIS-enabled short-packet NOMA systems," *IEEE Transactions on Vehicular Technology*, vol. 72, no. 10, pp. 13764–13769, 2023.
- [107] J. Xu, L. Yuan, N. Yang, N. Yang, and Y. Guo, "Performance analysis of STAR-IRS aided NOMA short-packet communications with statistical CSI," *IEEE Transactions on Vehicular Technology*, vol. 72, no. 9, pp. 12385–12390, 2023.

[108] M. V. Katwe, R. Deshpande, K. Singh, C. Pan, P. H. Ghare, and T. Q. Duong, "Spectrally-efficient beamforming design for STAR-RIS-aided URLLC NOMA systems," *IEEE Transactions on Communications*, vol. 72, no. 7, pp. 4414–4431, 2024.

- [109] S. Lv, X. Xu, S. Han, Y. Liu, P. Zhang, and A. Nallanathan, "STAR-RIS enhanced finite blocklength transmission for uplink NOMA networks," *IEEE Transactions on Communications*, vol. 72, no. 1, pp. 273–287, 2024.
- [110] B. Tahir, S. Schwarz, and M. Rupp, "Outage analysis of uplink IRS-assisted NOMA under elements splitting," in 2021 IEEE 93rd Vehicular Technology Conference (VTC2021-Spring), pp. 1–5, 2021.
- [111] S. Bi, Y. Zeng, and R. Zhang, "Wireless powered communication networks: an overview," *IEEE Wireless Communications*, vol. 23, no. 2, pp. 10–18, 2016.
- [112] Y. Liu, S. A. Mousavifar, Y. Deng, C. Leung, and M. Elkashlan, "Wireless energy harvesting in a cognitive relay network," *IEEE Transactions on Wireless Communications*, vol. 15, no. 4, pp. 2498–2508, 2016.
- [113] Y. Liu, Z. Ding, M. Elkashlan, and H. V. Poor, "Cooperative non-orthogonal multiple access with simultaneous wireless information and power transfer," *IEEE Journal on Selected Areas in Communications*, vol. 34, no. 4, pp. 938–953, 2016.
- [114] C. Pan, H. Ren, K. Wang, M. Elkashlan, A. Nallanathan, J. Wang, and L. Hanzo, "Intelligent reflecting surface aided MIMO broadcasting for simultaneous wireless information and power transfer," *IEEE Journal on Selected Areas in Communications*, vol. 38, no. 8, pp. 1719–1734, 2020.
- [115] K. W. Choi, S. I. Hwang, A. A. Aziz, H. H. Jang, J. S. Kim, D. S. Kang, and D. I. Kim, "Simultaneous wireless information and power transfer (SWIPT) for internet of things: Novel receiver design and experimental validation," *IEEE Internet of Things Journal*, vol. 7, no. 4, pp. 2996–3012, 2020.
- [116] M. K. Simon, Probability distributions involving Gaussian random variables: A handbook for engineers and scientists. Springer, 2006.
- [117] I. S. Gradshteyn and I. M. Ryzhik, *Table of integrals, series, and products*. Academic press, 2014.

[118] S. Primak, V. Kontorovich, and V. Lyandres, Stochastic methods and their applications to communications: stochastic differential equations approach. John Wiley & Sons, 2005.

- [119] T. A. Khan, R. W. Heath, and P. Popovski, "Wirelessly powered communication networks with short packets," *IEEE Transactions on Communications*, vol. 65, no. 12, pp. 5529–5543, 2017.
- [120] F. B. Hildebrand, Introduction to numerical analysis. Courier Corporation, 1987.
- [121] C. D. Ho, T.-V. Nguyen, T. Huynh-The, T.-T. Nguyen, D. B. da Costa, and B. An, "Short-packet communications in wireless-powered cognitive IoT networks: Performance analysis and deep learning evaluation," *IEEE Transactions on Vehicular Technology*, vol. 70, no. 3, pp. 2894–2899, 2021.
- [122] Y. Zhang, L. Yang, X. Li, K. Guo, H. Liu, and Y. Bian, "STARRIS-assisted IoV NOMA networks with hardware impairments and imperfect CSI," IEEE Transactions on Intelligent Transporation System, pp. 1–10, 2024.
- [123] X. Yue, J. Xie, C. Ouyang, Y. Liu, X. Shen, and Z. Ding, "Active simultaneously transmitting and reflecting surface assisted NOMA networks," *IEEE Transactions on Wireless Communications*, vol. 23, no. 8, pp. 9912–9926, 2024.
- [124] H. A. Suraweera, P. J. Smith, and M. Shafi, "Capacity limits and performance analysis of cognitive radio with imperfect channel knowledge," *IEEE Transactions* on Vehicular Technology, vol. 59, no. 4, pp. 1811–1822, 2010.
- [125] D. Li, "Performance analysis of MRC diversity for cognitive radio systems," *IEEE Transactions on Vehicular Technology*, vol. 61, no. 2, pp. 849–853, 2012.

List of Publications

Journal Publications

- S. Kumar, R. Singh, B. Kumbhani and S. Agarwal, "A New Paradigm for IRS-NOMA Transmission," *IEEE Transactions on Vehicular Technology*, vol. 73, no. 7, pp. 10835-10839, July 2024.
- S. Kumar and B. Kumbhani, "Wireless Powered Reconfigurable Intelligent Surface Aided Cognitive NOMA Network With Hardware Impairments: IBL and FBL Analysis," accepted for publication in *IEEE Internet of Things Journal*, doi: 10.1109/JIOT.2025.3538534.
- 3. S. Kumar, B. Kumbhani, and S. Darshi, "Performance Analysis of STAR-RIS aided Short-Packet NOMA Network under imperfect SIC and CSI," accepted for publication in *IEEE Systems Journal*, doi: 10.1109/JSYST.2025.3562732.
- S. Kumar and B. Kumbhani, "Performance analysis of active STAR-RIS-assisted NOMA with hardware impairments at finite blocklength," *Digital Signal Processing*, p. 105206, 2025.
- 5. **Shiv Kumar**, Brijesh Kumbhani, and Georges Kaddoum, "Finite Blocklength Analysis of Active RIS-assisted FDTW Communication with Hardware Impairments," in *IEEE Wireless Communications Letters*. (Under Revision)

Conference Proceeding

- S. Kumar and B. Kumbhani, "Performance Analysis of RIS-assisted Full-Duplex Two-Way NOMA using iFBL and FBL Codes," 2024 IEEE Middle East Conference on Communications and Networking (MECOM), Abu Dhabi, United Arab Emirates, 2024, pp. 458-463, doi: 10.1109/MECOM61498.2024.10881231.
- S. Kumar, R. Singh and B. Kumbhani, "Polarised-decoupling for STAR-RIS assisted Dual Serve," 2024 IEEE Middle East Conference on Communications and Networking (MECOM), Abu Dhabi, United Arab Emirates, 2024, pp. 470-475, doi: 10.1109/MECOM61498.2024.10881695.
- 3. S. Kumar and B. Kumbhani, "Performance Analysis of Active RIS-assisted Full-Duplex-Two-Way NOMA System under Finite Blocklength with Hardware

Impairments," 2024 IEEE International Conference on Advanced Networks and Telecommunications Systems (ANTS), Guwahati, India, 2024, pp. 1-6, doi: 10.1109/ANTS63515.2024.10898867.

4. S. K. Singh, N. Gupta, R. Singh, S. Kumar and B. Kumbhani, "Seamless V2I Connectivity: How THz Waves and Base Station Density Contribute," 2024 IEEE International Conference on Advanced Networks and Telecommunications Systems (ANTS), Guwahati, India, 2024, pp. 1-3, doi: 10.1109/ANTS63515.2024.10898386.